Title

Nanofibrous Materials for Improved Sorbent Performance in the Sorption-Enhanced Steam Methane Reforming System

Author

Minardi, Luke

Publication Date

2020

Peer reviewed|Thesis/dissertation

UNIVERSITY OF CALIFORNIA

Los Angeles

Nanofibrous Materials for Improved Sorbent Performance in the Sorption-Enhanced Steam Methane Reforming System

A dissertation submitted in partial satisfaction of the requirements for the degree

Doctor of Philosophy in Chemical Engineering

by

Luke Minardi

2020

ABSTRACT OF THE DISSERTATION

Nanofibrous Materials for Improved Sorbent Performance in the Sorption-Enhanced Steam Methane Reforming System

by

Luke Minardi
Doctor of Philosophy in Chemical Engineering
University of California, Los Angeles, 2020
Professor Dante Simonetti, Chair

This work focuses on improving material deficiencies in calcium oxide CO_2 sorbents for applications in sorption-enhanced steam methane reforming (SE-SMR). Challenges such as low sorption conversion and low stability of calcium oxide sorbents were addressed with studies on material synthesis and material chemistry. Calcium oxide decomposed from electrospun PVP-$Ca(NO_3)_2$ nanofibers lead to higher conversions and higher carbonation kinetics compared to calcium oxide from marble and synthesized via decomposition and hydrothermal treatment. Favorable material properties such as large macropores, high surface area and porosity, and small agglomerate size were enabled by electrospinning and led to the improved material performance. Electrospinning led to calcium oxide reaching stoichiometric capacity, 0.79 g_{CO2} g_{CaO}^{-1}, at 600 and 650°C in 100% CO_2.

In order to address the low stability of calcium oxide sorbents, metal additives were incorporated in the electrospinning solution so that upon nanofiber decomposition there was a mixture of additive metal oxide and calcium oxide. A systematic study was carried out on additive oxides using Al, Co, Cr, Er, Ga, In, La, Li, Mg, Nd, Y, and Zn additives to probe which properties impact the sorption capacity and stability of modified calcium oxide. Material

properties such as molecular weight of the additive oxide or the formation of a mixed oxide ($M_xCa_yO_z$) and the M:Ca ratio directly impact the sorption capacity of the modified sorbents due to the effect of dilution and consumption of CaO in the mixed oxide. The Tammann temperature of the additive oxide was found to have a strong effect on the conversion of the modified sorbent. If the Tammann temperature was higher than the maximum treatment temperature the sorbent approached 100% conversion, however if the Tammann temperature was lower than the maximum treatment, conversion decreased with decreasing Tammann temperature. Further, Tammann temperature was found to be the primary material property influencing the stability of the modified sorbent and the formation of mixed oxides did not impact material stability. The stability of the modified sorbents increased with increasing Tammann temperature of the additive oxide. By optimizing the metal loading the alumina modified CaO-nanofibers, 1Al-20Ca-O, reached 0.75 g_{CO2} g_{CaO}^{-1}, while being an order of magnitude more stable during carbonation-regeneration cycling compared to unmodified CaO-nanofibers.

Calcium oxide was also tested in a packed bed reactor in CO_2 breakthrough experiments and in bench-scale SE-SMR experiments. The CO_2 breakthrough experiments show that calcium oxide sorbents are even less stable when they carbonate in the presence of steam. SE-SMR experiments showed that the sorption capacity determined in the TGA related directly to the CO_2 breakthrough time during the reforming reaction, with CaO-nanofibers having the highest breakthrough time and CaO-marble having the lowest breakthrough time. Further, the modified 1Al-20Ca-O sorbent lost only 5% of its CO_2 breakthrough time over 10 cycles, indicating that modified sorbents retain their stability benefits under realistic SE-SMR operating conditions.

The dissertation of Luke Minardi is approved.

Louis Bouchard

Vasilios Manousiouthakis

Philippe Sautet

Dante Simonetti, Committee Chair

University of California, Los Angeles

2020

TABLE OF CONTENTS

LIST OF FIGURES

LIST OF TABLES

ACKNOWLEDGMENTS

This work would not have been possible to complete without help and support from many people. Unfortunately, I am unable to list every name that comes to mind in this section. For anyone who was unnamed, you have my thanks and apologies.

I would like to thank my mom and dad for their continual support and belief in me. Nothing I have accomplished thus far would have been possible without their love, hard work, and parenting. John, Jake, and Sarah made my time at home over the holidays a ton of fun and helped motivate me to work hard when I got back to lab. Thank you to my grandparents for their love and care while I was growing up. Special thanks to grandma Dot – our phone calls have been like miniature vacations. Last, I would like to thank my aunts, uncles, cousins, and friends for everything you've done for me and for making my visits home so much fun!

To my advisor Dante, you helped me with everything from raising the quality of my research, writing, and presentations to showing by example how to maintain a work-life balance. It is difficult to put in words how much I appreciate the time in your lab, so I will simply say thank you. Thank you to my committee members Professors Bouchard, Manousiouthakis, and Sautet. You all raised many constructive questions and had many good suggestions for my work.

Former Simonetti group members, good luck in present and future endeavors. To current group members, please keep the lab/office intellectually stimulating and a fun place to be! Derrick and Faisal - it was a great experience to work with both of you. Although we didn't work together as much in lab - Sara, Aziz, Eric, Anas, Steven, Byron, Julie, Christina, and JC made life in lab a lot of fun and were always there to help out. Lastly, I would like the many

undergraduates I have mentored or worked with in lab; in particular Jessii, Nico, Zubin, Richa, Brian, Jon, and Ksenia.

I would like to thank Professor Jane Chang. Being in your group for 2 years taught me many valuable lessons on how to properly conduct and present research. I appreciate everything you've done for me. I'd also like to thank former Chang lab group members Calvin, Colin, Cyrus, Diana, Ernest, Jack, Jea, Jeff, Kevin, Nick, and Ryan! You guys helped me learn so much in lab and were so much fun to be around!

To the basketball crew Vasili, Patty, Somi, Kevin, Kelly, and everyone else who joined in – our weekly games were a ton of fun and it was a good excuse to ditch lab a few hours.

Words cannot describe my thanks and appreciation for my many mentors throughout my academic career! First among them is Jack, dear leader of the etch crew. Thank you for showing me how to properly conduct research! Nick, you showed me how to do everything from the most mundane tasks to fixing broken equipment. Your training has been invaluable! Lucas Johnson and Rigved Epur my mentors from REUs at Colorado State University and University of Pittsburgh, respectively, showed me the basics of how to conduct research and had the trust in me to let me be highly independent in the lab. Lastly, I would like to thank Sebastian Marino for making chemistry, calculus, and learning fun! Prior to meeting you I won't have dreamed of a career path in engineering. I know many of your former students feel a similar appreciation for your positive influence on our lives.

VITA

2010 – 2014	B. S. Chemical Engineering Rowan University Glassboro, NJ
2014 – 2020	Graduate Student Researcher Department of Chemical Engineering University of California, Los Angeles
2017 – 2020	Teaching Assistant Department of Chemical Engineering University of California, Los Angeles

PUBLICATIONS

1. **Luke Minardi**[*], Faisal H. Alshafei[*], Zubin Mishra and Dante A. Simonetti, *Calcium Oxide-based Nanofibers as Stable Sorbents with Maximum Capacity for CO_2-free H_2 Production*, Submitted to Sustainable Energy & Fuels. [*]these authors contributed equally to this work
2. Faisal H. Alshafei[*], **Luke Minardi**[*], Derrick Rosales, Gen Chen and Dante A. Simonetti, *Improved Sorption-Enhanced Steam Methane Reforming via Calcium Oxide–Based Sorbents with Targeted Morphology*, Energy Technology, 2019, 7, 1800807. [*]these authors contributed equally to this work
3. Nicholas D. Altieri, Jack Kun-Chieh Chen, **Luke Minardi** and Jane P. Chang, *Review Article: Plasma–Surface Interactions at the Atomic Scale for Patterning Metals*, Journal of Vacuum Science and Technology A, 2017, 35, 05C203.
4. Rigved Epur, **Luke Minardi**, Moni K. Datta, Sung Jae Chung and Prashant N. Kumta, *A Simple Facile Approach to Large Scale Synthesis of High Specific Surface Area Silicon Nanoparticles*, Journal of Solid State Chemistry, 2013, 208, pp 93-98.

PRESENTATIONS

1. **Luke Minardi**, Faisal H. Alshafei, Zubin Mishra and Dante A. Simonetti, (2019, June), *Improved Sorption Enhanced Steam Methane Reforming Using Electrospun Calcium Based Sorbents*. Presented at NAM 26, Chicago, IL.
2. **Luke Minardi**, Faisal H. Alshafei, Zubin Mishra and Dante A. Simonetti, (2018, October), *The Effects of Metal Dopants on the Stability of Calcium Oxide Nanofibers for Use in Sorption Enhanced Steam Methane Reforming*. Presented at 2018 AIChE National Conference, Pittsburgh, PA.
3. **Luke Minardi**, Faisal H. Alshafei, Derrick Rosales and Dante A. Simonetti, (2017, October), *Utilization of Highly Reactive Calcium Oxide Nanofibers for CO_2 Sorption in Steam Methane Reforming*. Presented at 2017 AIChE National Conference, Minneapolis, MN.
4. **Luke Minardi**, Nicholas D. Altieri, Jack Kun-Chieh Chen, Ernest Chen and Jane P. Chang, (2016, April), *Thermodynamic Prediction and Experimental Verification of Etch Selectivity for EUV Mask Materials*. Presented at IMPACT+ Workshop, San Jose, CA.

5. **Luke Minardi**, Nicholas D. Altieri, Jack Kun-Chieh Chen, Ernest Chen and Jane P. Chang, (2016, April), *Thermodynamic Prediction and Experimental Verification of Etch Selectivity for EUV Mask Materials*. Presented at IMPACT+ Workshop, San Jose, CA. (Poster)
6. **Luke Minardi**, Jack Kun-Chieh Chen, Nicholas D. Altieri and Jane P. Chang, (2015, November), *Thermodynamic Prediction and Experimental Verification of Etching Selectivity for Tantalum-based Materials*. Presented at IMPACT+ Workshop, San Jose, CA. (Poster)

Chapter 1: Introduction and Background

1.1 – Motivation

Steam reforming of chemical feedstocks, e.g. natural gas, naphtha, coal, or biomass is a fundamental process for the chemical industry to produce syngas or high purity H_2. These reforming products are feedstocks for a variety of subsequent processes such as ammonia synthesis, methanol synthesis, Fisher-Tropes synthesis, or fuel cell power. Typically, steam reforming uses natural gas as a feed due to its low cost and ready availability. The U.S. Energy Information Administration has reported proven shale gas reserves of 308 trillion ft^3.[1] In remote fields, it is estimated that 30% of natural gas is flared.[2]

Annual production of hydrogen is approximately 500 Billion m^3 yr^{-1} and nearly half of the production is from steam methane reforming.[3] Over half of the world's hydrogen is consumed in the production of fertilizer (ammonia synthesis) and the majority of remaining hydrogen is consumed by chemical industries and refineries.[4] Production of hydrogen via hydrocarbons results in $C_{(s)}$, CO, and CO_2 byproducts and reaction conditions determine the spectrum and ratios of byproducts.[3]

Atmospheric carbon dioxide concentrations have increased significantly in the past 50-60 years.[5] This accumulation of carbon dioxide in the atmosphere occurs because the rate of anthropogenic emission is higher than the rate of natural sequestration,[6] and has led the national academy of engineers to list the development of carbon sequestration methods as 1 of 14 engineering grand challenges.[7] Amine scrubbing is currently a widely used process for carbon capture from coal fired power plants and post-combustion carbon capture.[8] Amine scrubbing is a chemically and economically effective method for capture, but it is limited to post-processing

use. Sequestration of carbon byproducts as they are produced by sorption-enhanced steam methane reforming offers thermodynamic and process benefits, in addition to reducing or potentially eliminating CO_2 emissions in hydrogen production.

Due to its industrial ubiquity, many fundamental methane reforming studies on the thermodynamics, kinetics, and catalysts of have been carried out.[5] Also, significant studies have been conducted on modifications to the reforming process to improve economics.

1.2 – Steam Methane Reforming Background

1.2.1 – Thermodynamics

Steam methane reforming (SMR) reactions, 1-3 in **Table 1**, are a highly endothermic system of reactions that produces hydrogen with carbon dioxide and carbon monoxide as byproducts. The equilibrium constant as a function of temperature may be seen in **Figure 1**. Industrially, SMR is typically operated around 800-1000˚C and 14-20 atm, the high operating temperature is necessary for the high conversion of methane and high concentration of hydrogen. The typical composition exiting the reformer is 76% H_2, 13% CH_4, 12% CO, 10% CO_2 on a dry basis.[9] The high operating temperatures of SMR results in a number of drawbacks like high capital cost, high operating cost, and catalyst deactivation via coking and sintering.

Inclusion of a CO_2 sorbent in the reforming system results in the generic CO_2 sorption reaction, reaction 4 in **Table 1**, a system that includes all 4 reactions in **Table 1** is referred to as sorption-enhanced steam methane reforming (SE-SMR). There have been many studied sorbents, discussed below, which enhance process conditions because CO_2 sorption is typically exothermic and it consumes CO_2, a reforming product. This enables lower processing temperatures and drives the reaction right following Le Chatelier's principle, which enables cost savings on

utilities and downstream separations. The addition of calcium oxide as a CO_2 sorbent enables favorable thermodynamics at temperatures as low as 400˚C, compared to the highly unfavorable thermodynamics for SMR at the same conditions, **Figure 1**. The thermodynamics of calcium oxide carbonation are extremely favorable, other sorbents with less favorable thermodynamics have equilibrium conversions between calcium oxide sorbent and no sorbent.

Table 1. The steam methane reforming reactions with their heat of reaction and Gibbs energy of reaction

RX No.	Reaction	ΔH°_{RXN} (kJ mol^{-1})	ΔG°_{RXN} (kJ mol^{-1})
1	$CH_4 + H_2O = CO + 3\ H_2$	205.8	141.9
2	$CH_4 + 2\ H_2O = CO_2 + 4\ H_2$	164.7	113.3
3	$CO + H_2O = CO_2 + H_2$	-41.1	-28.6
4	$MO_{(s)} + CO_{2\ (g)} = MCO_{3\ (s)}$	n/a	n/a

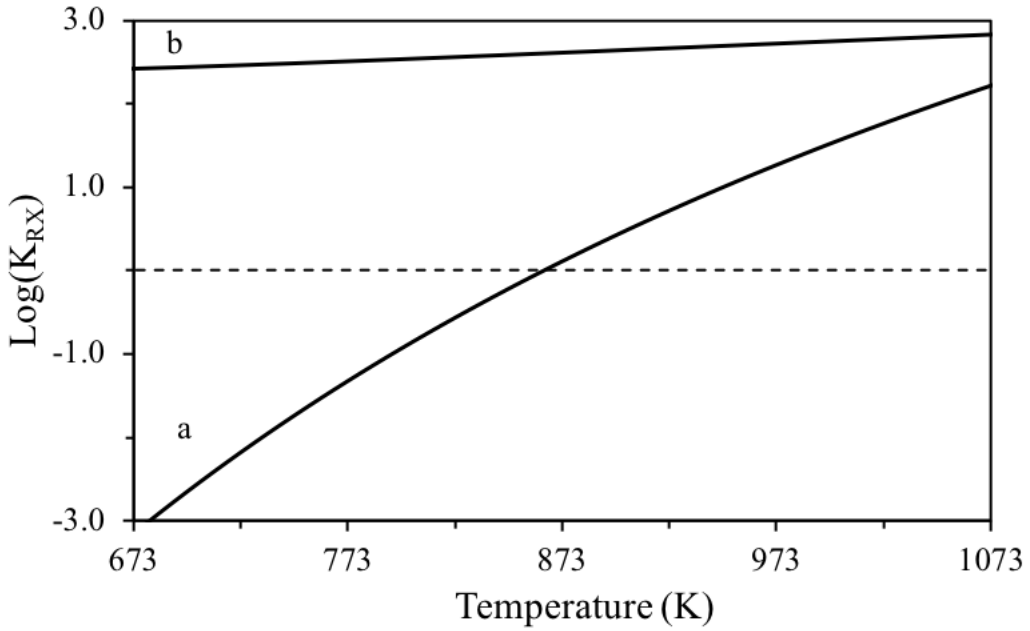

Figure 1. Equilibrium constant as a function of temperature (P = 1 atm) for (a) reaction 2, in **Table 1**, and (b) the sum of reactions 2 and 4 (where $MO_{(s)}$ is CaO), in **Table 1**. The dotted horizontal line is where $Log(K_{RX}) = 0$.

1.3 – Sorption Enhanced Steam Methane Reforming Background

Due to the drawbacks of high temperature methane reforming studies have investigated methods to improve the reformer's thermodynamics and, as a result, the economics. A review by Barelli et al. covers two methods of improving the thermodynamics of reforming.[9] The first method is using a membrane reactor to remove reaction products (H_2, CO_2) as they are created, which shifts the reaction right and creates a higher purity product stream. A number of membranes have been investigated including oxygen transport membranes, hydrogen transport membranes,[10] ion transport membranes,[11] and palladium membranes.[12] A more promising method of improving reforming thermodynamics is sorption-enhanced reforming. Sorption enhanced steam methane reforming (SE-SMR) uses a solid, which reacts with CO_2 to form a solid product, as seen with a generic metal oxide, MO, in reaction 4 (**Table 1**). The integration of catalyst and sorbent was proposed in 1933 in a U.S. Patent by Roger Williams.[13] This approach consumes CO_2 and shifts the reforming reactions right similar to membrane reactors. The exothermic carbonation reaction with CO_2 enables a reduction of the operating temperature of the reformer to 450-600°C. Due to the exothermicity of carbonation reactions, overall heat of reactions for the reforming and carbonation reactions are close to zero. The carbonation reaction produces a higher quality H_2 product stream by capturing its reforming co-product. The incorporation of absorbers in the reformer reduce the cost of H_2 production by eliminating the need for high temperature resistant alloys, reducing catalyst sintering and coking, reducing the required heat duty, and eliminating the need for downstream separation. Additionally, the carbonation reaction sequesters CO_2 for an environmentally benign process. In short, SE-SMR improves methane conversion, reduces operating temperature, and reduces the need for down-stream processing compared to SMR.

Sorbents typically are not utilized in industrial processes because they lack in one of the following areas: sorbent capacity, sorption kinetics, sorbent regeneration temperature, and sorbent stability upon cycling (cyclability). CO_2 absorbers must meet 3 requirements for the SE-SMR process: they must have a capacity of 0.3 $mmol_{CO2}$ $g_{sorbent}^{-1}$ (0.0132 g $_{CO2}$ $g_{sorbent}^{-1}$) at operating conditions (~10 atm and 350-450°C), high stability in hydrothermal conditions, and fast absorption kinetics.[9,14]

Table 2. Studied CO_2 sorbents stoichiometric capacity, calcination temperature, and stability[9]

	Sorbents	Stoichiometric Capacity (g_{CO2} $g_{sorbent}^{-1}$)	Regeneration Temp (°C)	Capacity after 45 Cycles (g_{CO2} $g_{sorbent}^{-1}$)
Natural Sorbents	CaO	0.79	900	0.316
	K_2O/hydrotalcite	0.029	400	Stable
Synthetic Sorbents	Li_4SiO_4	0.37	750	Stable to 100x
	Li_2ZrO_3	0.29	690	Stable to 100x
	Na_2ZrO_3	0.24	790	Stable to 100x

Various materials have been investigated for the purpose of CO_2 absorption seen in **Table 2**; studies have included both natural absorbers and synthetic absorbers. Calcium oxide has the highest CO_2 loading capacity, 18 $mmol_{CO2}$ g_{CaO}^{-1}or 0.79 g_{CO2} g_{CaO}^{-1}. $CaCO_3$ regeneration occurs at elevated temperatures ~900°C, which leads to particle sintering.[15] Absorber sintering leads to a decrease in capacity of about 60%, after only 45 cycles.[9] Natural forms of calcium oxide include dolomite and huntite, which are (1:1) and (1:3) mixtures of $CaCO_3$ and $MgCO_3$ respectively. Studies by Silaban et al. have found that $MgCO_3$ in dolomite and huntite does not undergo cyclic calcination and carbonation; rather it remains MgO after the first calcination.[16,17] Dolomite and huntite have absorption capacities proportional to their $CaCO_3$ content (10.7 $mmol_{CO2}$ g^{-1} and 5.7 $mmol_{CO2}$ g^{-1}) and stability after 45 cycles inversely proportional to $CaCO_3$

content (~20% and 40%).[9] A More detailed description of synthetic CaO sorbents will follow in the subsequent section. Potassium carbonate promoted hydrotalcites (K_2CO_3/HTC) is a promising alternative to $CaCO_3$ absorbers because they have high cycling stability due the relatively low calcination temperature of 400°C. K_2CO_3/HTC has a capacity of 0.3-0.45 $mmol_{CO2}$ g^{-1} over 6000 cycles.[18] The primary drawback is the relatively small sorption capacity versus calcium oxide and it is more relevant to sorption enhanced water gas shift because of the lower operating temperatures. Synthetic sorbents Li_4SiO_4,[18] Li_2ZrO_3,[18] and Na_2ZrO_3 have moderate stability (~100 cycles) and capacity (5-9 $mmol_{CO2}$ g^{-1}). The ideal sorbent for SE-SMR needs a balance between absorber loading capacity, absorption kinetics, regenerating temperature, and cycling capacity. The ideal absorber would have the capacity of calcium oxide with regeneration temperature and stability of K_2CO_3/HTC.

1.3.1 - CaO Sorbents

CaO-based materials are the predominant sorbents used in SE-SMR because of their high sorption capacity (0.79 g_{CO2} g_{CaO}^{-1}), adequate reversibility ($CaO + CO_2 \leftrightarrow CaCO_3$; K_{eq} = 87 at 923 K), fast carbonation–calcination kinetics ($E_{carbonation}$ = 20 kJ mol^{-1}; $E_{calcination}$ = 104 kJ mol^{-1}),[19] and low material cost.[20–22] Unfortunately, CaO sorbents (usually derived from natural CaO compounds such as limestone and dolomite) suffer from low conversions, as discussed above. This poor performance is due to the formation of $CaCO_3$ product layers that cover CaO surfaces and fill material pores, thereby inhibiting the diffusion of CO_2 to reaction interfaces.[23] A number of studies has investigated a variety of precursors, treatment steps,[24,25] and synthesis techniques (e.g., sol-gel,[26] flame spray pyrolysis,[27] hydrothermal core shell structures,[28] and templating[29,30]) to improve the capacity, kinetics, and/or stability of CaO. These synthesis techniques aim to

increase porosity and surface area and reduce the domain size of the sorbents in order to minimize diffusion limitations. Of these synthesis techniques flame spray pyrolysis and templating have had the most promising results. In addition, both natural and synthetic CaO sorbents have significant decrease in their sorption capacity over multiple carbonation-regeneration cycles (60% loss in initial capacity for limestone after 10 cycles).[31] Upon carbonation-regeneration cycling, issues such as, particle sintering and aggregation as well as the simultaneous loss in surface area and pore volume are responsible for the observed loss in activity for pure, unmodified CaO sorbents.[32–35] It is impossible to avoid sintering in such materials because the operating temperature for CaO sorbents is typically in the range of 873-973 K for carbonation and 1123-1223 K for regeneration, which is significantly above the Tammann temperature of $CaCO_3$ (~806 K).[36] Highly active, efficient, and inexpensive adsorbents are critical for the widespread implementation of SE-SMR technology.[37]

1.3.2 - Modified CaO

Metal additives have been shown to be an effective method to produce CaO-based sorbents that are highly stable upon cycling and have a reasonable CO_2 capacity. However, stability is often improved at the expense of CO_2 capacity because of dilution of the total amount of CaO in the sorbent. Aluminum-modified CaO sorbents have attracted the most attention in the literature. Li et al.,[38] synthesized a CaO/$Ca_{12}Al_{14}O_{33}$ sorbent (mass ratio of CaO to $Ca_{12}Al_{14}O_{33}$ was 3 to 1) that exhibited a CO_2 sorption capacity of 0.41-0.45 g_{CO2} $g_{sorbent}^{-1}$ and that was stable for up to 13 cycles (carbonation conditions: 963 K, 30 min, 14% CO_2, regeneration conditions: 1123 K, 10 min, 100% N_2). Zr-modified sorbents also show great promise in improving the mechanical durability of CaO by forming a stable mixed oxide ($CaZrO_3$) phase, which acts as an

effective spacer and barrier against sintering, thus, preventing growth in the CaO grains upon repeated cycling.[39–41] One study by Lu et al.[36] synthesized a sorbent with a Zr:Ca atomic ratio of 3:10 via flame spray pyrolysis with a capacity of 0.27 g_{CO2} $g_{sorbent}^{-1}$ (57% CaO conversion). The sorbent was stable up to 100 cycles (carbonation conditions: 973 K, 30 mins, 30% CO_2, regeneration conditions: 973 K, 30 mins, 100% He). The stability of the sample was attributed to the high Tammann temperature of ZrO_2 (1491 K). Similar to ZrO_2, MgO has been shown to improve stability, especially when the molar ratio of CaO to MgO was ca. 2 to 1.[42] Furthermore, sorbent formulations using MgO retain CO_2 capacity because, unlike Al_2O_3 and ZrO_2, CaO and MgO remain as separate oxide phases.[43]

Aside from the aforementioned metals, other additives or supports that have been reported to be effective at increasing the stability of CaO-based sorbents include CeO_2,[36,44] $TiO_2/CaTiO_3$,[36,45,46] Nd_2O_3,[41,47] Y_2O_3,[48–50] La_2O_3,[49,51–53] $CaMnO_4$,[51] SiO_2,[51,54–56] Yb_2O_3,[41] and Pr_6O_{11}.[41] Despite these numerous promising reports on modified CaO materials, the results are difficult to compare in a parallel manner, as only a few studies have comprehensively compared the effects of different additive metals on CO_2 sorption capacity and stability while also using the same synthesis method and testing conditions.[36,41,51] Furthermore, it is still unclear (i) which other metals could function as stabilizers or performance enhancers for CaO-based sorbents, and more significantly, (ii) which chemical and physical properties are responsible for stability improvements. The studies on additives reported in this work are all using the same electrospinning technique and regeneration at mild conditions to enable comparison with the bulk of modified CaO literature.

1.4 – Scope and Organization

This thesis focuses on studying calcium oxide because it has the highest stoichiometric capacity. The work of this thesis focuses on (i) maximizing the sorption capacity of CaO sorbents by tuning synthesis techniques, discussed in Chapter 3, (ii) maximizing the stability of the high capacity calcium oxide by introducing additive oxides, (iii) understanding the effect of this metal additives on sorbent capacity and stability, discussed in Chapter 5, and (iv) studying CaO-based sorbents with breakthrough curves with CO_2 feeds and in the SE-SMR reaction to verify and quantify the translation of the material performance to operating conditions, discussed in Chapter 5.

Chapter 2: Experimental Methods

2.1 – Sorbent Characterization

2.1.1 – Thermogravimetric Analyzer (TGA)

Thermogravimetric analysis was conducted in alumina crucibles in a Perkin Elmer TGA. For all experiments, the pressure was 1 bar and the gas flow rate was 200 standard ml min^{-1}. High gas flow rates were used minimize any transport effects in the thermogravimetric analyzer (TGA). Reactions were conducted in house air, with moisture and CO_2 removed, argon (UHP Argon 99.999% purity), or CO_2 (Wright Bros, Inc., 99.5%).

2.1.2 - Plug Flow Reactor

A home-built plug flow reactor was constructed for CO_2 breakthrough and Gibbs' reactor characterization of the sorbents. A schematic of the constructed PFR can be seen in **Figure 2**. Gasses are introduced through an MKS Mass Flow Controller and pass through ¼" 316 S.S. tubing wrapped in heating wire. Water is introduced through an in-line port, where it is vaporized by S.S. tubing heated above 120°C. The orientation of two-way valves V6 and V8 one globe valve V7 are used to send gasses to the bypass line or through the reactor – this is done to ensure that gas mixtures reach steady-state before introduction to the reactor. Pressure can be controlled by the pressure regulator upstream of the condenser. The condenser is used to condense steam in order to protect the gas chromatograph. If the process gas was dry, then then two-way valve V9 and globe valve V10 were changed to bypass the condenser. The outlet stream, post condenser, can be sent to the Fourier-transform infrared spectrometer (FTIR) (MKS Multigas) or gas chromatograph (GC) (Agilent 7890B GC system with a thermal conductivity detector) for data on CO_2 sorption or SMR and SE-SMR respectively. The FTIR is best to

determine CO_2 breakthrough time because it has a shorter sample time, whereas the GC is best used for conversion and selectivity because it can accurately determine the composition of all gas components.

The reactor itself can be either ¼" or ½" outer diameter reactor. The catalyst and/or sorbent particles are sorted to a uniform range of sizes (typically 180-250 μm particles), using meshes, these particles are packed between two plugs of quartz wool. The packed bed is then pre-treated in hydrogen (to reduce the catalyst) or helium. Typical pre-treatment conditions are the following, 50 sccm H_2 at 998 K (ramp rate of 2.3 K min^{-1}) held overnight. Post pre-treatment, reactors are purged with helium before going to the bypass to determine reactant concentrations (identities and flow ranges bay be seen in **Table 3**). Bubble flow meters were used to determine flow rate, so molar flowrates could be used to calculate reaction rates.

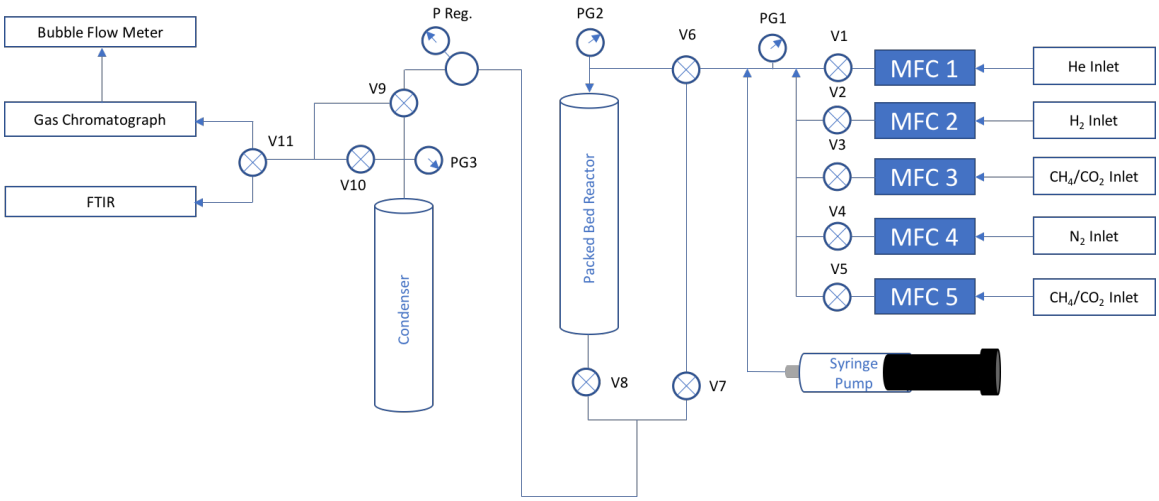

Figure 2. Process flow diagram of laboratory plug flow reactor for SMR and SE-SMR experiments

Table 3. Mass flow controller gasses and maximum flow rate

MFC	Gas	Max Flow Rate (ml min^{-1})
1	He	500
2	H_2	500
3	CH_4/CO_2	500
4	N_2	500
5	CH_4/CO_2	50

2.1.4 – Nitrogen Physisorption

A Micrometrics ASAP 2020 Plus was used to analyze the surface area, pore volume, and pore size. Samples were degassed at 423 K for 8 h at a rate of 10 K min^{-1} to remove any adsorbed gas and water on the sample surface. Nitrogen was then adsorbed and desorbed from the sample surface under cryogenic conditions. The adsorption and desorption isotherms were used to calculate the Brunauer-Emmet-Teller (BET) surface area, pore volume, and average pore diameter.

2.1.5 – X-Ray Diffraction (XRD)

JEOL JDX-3530 and Philips X-Pert X-ray diffractometers with Cu Kα radiation of 1.5410 Å were used to obtain X-ray diffraction (XRD) patterns. XRD data was used to identify the crystals present and the average crystallite size using the Scherrer formula.

2.1.6 – Scanning Electron Microscopy

NOVA 230 Nano Scanning Electron Microscope (SEM) was used to determine the morphology of the of the synthesized CO_2 sorbents, supports, and catalysts. Particles sizes were quantified from SEM micrographs using ImageJ software.

2.2 – Sorbent Synthesis and Preparation

The nomenclature for the sorbents in this thesis can be found in Appendix 1.

2.2.1 – Electrospinning Setup

A cartoon of the electrospinning set-up can be seen in **Figure 3**. A polymer solution was prepared by dissolving 1.3 g of PVP in 23 cm^3 of ethanol. The solution was then vortexed (Fisher Scientific Digital Vortex Mixer) at 2900 rpm for 1 h until the PVP was completely dissolved. The polymer solution was left to settle for 5 mins, transferred to a beaker, and stirred for 15 mins. The metal containing solution was prepared by dissolving 0.975 g of calcium nitrate in 10 cm^3 of DI water and stirring the solution for 0.5 h. The calcium-containing solution was then added dropwise to the polymer-containing solution. The solution was stirred for 0.25 h, and then vortexed for 0.5 h at 2900 rpm.

The electrospinning solution was placed in a 10 mL syringe (BD 10 mL syringe with Luer Lok™ tip) with a hypodermic needle (Monoject™ Standard 30G x ¾"). The distance between the tip of the needle and a stainless-steel collecting plate, which was covered with aluminum foil, was 16 inches. A Gamma High Voltage Research ES75 power supply was used to apply 30 kV on the polymer jet while the polymer solution was extruded through the needle at a rate controlled by a syringe pump (1.0 $cm^3\ h^{-1}$; Kent Scientific Genie Plus). Dry air was circulated inside a 3 m^3 chamber at 6 $cm^3\ min^{-1}$ to control the relative humidity at 19.5 ± 1%. All electrospinning was carried out at ambient conditions: temperature (294 ± 3 K) and pressure (101 kPa). The collected fibers were thermally treated in air at 923 K for 8 h at a ramping rate of 5 $K\ min^{-1}$ to remove the PVP chains and form calcium oxide.

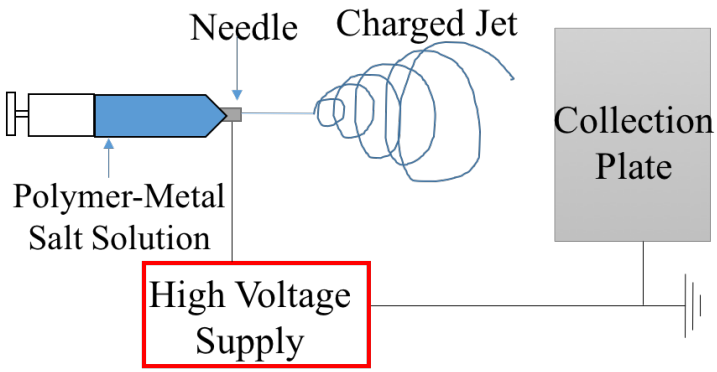

Figure 3. Cartoon of essential elements of electrospinning set-up

Electrospun nanofibers are similar to continuous, or infinite, nanorods. Their surface morphology and nanofiber diameter can be tuned by changing electrospinning conditions (i.e. viscosity, concentration, distance, extrusion rate, potential, humidity, air flow).[57] Electrospinning also enables fine tuning of material (catalyst or sorbent) composition by changing which metal salts are added to the fiber. Upon burning off the polymer and calcining the metals in the nanofiber, the morphology changes. For instance, $Mg(NO_3)_2$-PVP nanofibers pre-calcination are continuous and slightly crosslinked **Figure 4a**. When they are calcined the have the morphology of nanorods of relatively uniform length and diameter, seen in **Figure 4b**. The morphology of $Ca(NO_3)_2$-PVP nanofibers, discussed in Chapter 3, **Figure 7a and b**, are similar to their magnesium counterparts, however post calcination CaO-nanofibers, **Figure 7d**, have completely different morphology than MgO-nanofibers. This is behavior that is observed again in Chapter 4 with modified CaO sorbents.

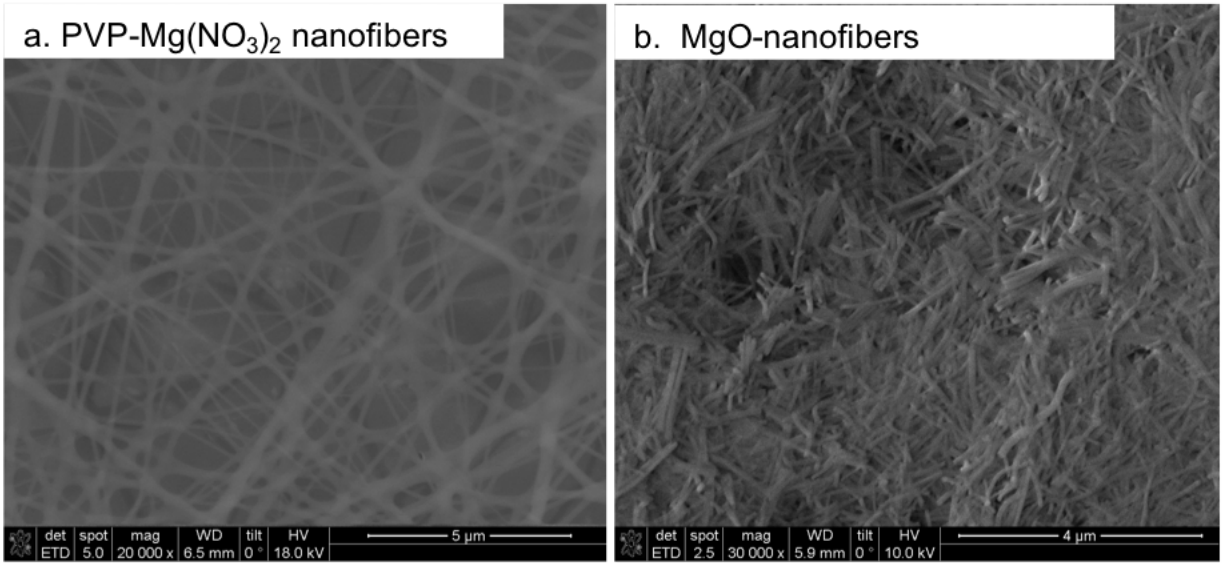

Figure 4. SEM images of (a) PVP-$Mg(NO_3)_2$ nanofibers pre-calcination (b) MgO-nanofibers calcined from PVP-$Mg(NO_3)_2$ (at 650°C for 8 hours).

2.2.3 – Thermal Decomposition and Hydrothermal Treatment

Three different thermal methods were used to prepare CaO samples from different precursors (marble, calcium acetate, and calcium nitrate). Calcium acetate was crushed and sieved to < 200 mesh, and then thermally treated in air at 1023 K for 8 h at a ramp rate of 5 K min^{-1} to form CaO (referred to as CaO-D-acetate). A marble-derived sample (referred to as CaO-marble) was also crushed and sieved to < 200 mesh, then thermally treated in air at 923 K for 8 h at a ramp rate of 5 K min^{-1}. Two samples were synthesized from decomposed calcium nitrate. A non-porous CaO sample was synthesized by crushing and sieving calcium nitrate to < 200 mesh, and then thermally treated in air at 1023 K for 8 h at a ramp rate of 5 K min^{-1} to form CaO (referred to as CaO-D-nitrate). A porous CaO sample was synthesized according to the method of surfactant-assisted hydrothermal interaction using previously synthesized CaO-D-nitrate powder as starting material. Subsequently, 0.8 g of CaO was dissolved in a beaker containing 150 cm^3 of DI water and 5 cm^3 of ethanol and stirred for 2 h. The CaO solution was then

ultrasonically treated for 2 h. The surfactant solution was prepared by dissolving 2.8 g of P123 in 100 cm^3 of water while stirring for 2 h. After stirring, the metal-containing solution was added to the surfactant solution, left stirring for 72 h, and then ultrasonically treated for 4 h. The solution was then transferred to a 1000 cm^3 Teflon-lined stainless-steel autoclave for hydrothermal treatment at 473 K for 60 h. The solid substance was filtered out and washed with 480 cm^3 of DI water and 20 cm^3 of ethanol (for the removal of the majority of the P123 surfactant). The solid was then dried overnight in a drying oven at 353 K. The as-obtained material was calcium hydroxide ($Ca(OH)_2$), which was subsequently thermally treated in air from room temperature to 923 K at ramping rate of 5 K min^{-1} for the generation of CaO.

2.3 – Sorption Kinetic Model

The random pore model (RPM) was first proposed by Bhatia and Perlmutter[58,59] and simplified to two equations by Grasa et al.[60] for the kinetic (Equation 1) and diffusion reaction regimes (Equation 2). The RPM is a result of solving the transport equation with diffusion and a surface reaction in a spherical particle with no bulk flow. The model assumes first order reaction kinetics, the rate of reaction is proportional to reaction surface, and no external mass transfer limitations. The RPM was used in this work to quantify carbonation reaction kinetics in terms of the reaction rate constant (k_{RPM}) and the effective diffusivity (D_{RPM}). The structural parameter, Ψ (Equation 3), was calculated using the initial surface area (S_0), initial length of pores (L_0), and initial porosity (ε_0), which were determined from the N_2 physisorption isotherms (see **Table 8** in the appendix for values). The RPM was not applied to the cycling studies due to potential changes in Ψ during carbonation-calcination cycling. In Equations 1 and 2, C_b, C_e, t, M_{CaO}, ρ_{CaO},

and Z are the bulk concentration of CO_2, equilibrium concentration of CO_2, reaction time, molar mass of CaO, density of CaO, and ratio of molar volumes of $CaCO_3$ to CaO, respectively.

$$\Psi = \frac{4\pi L_0(1-\varepsilon_0)}{S_0^2} \quad (1)$$

$$\frac{1}{\Psi}\left[\sqrt{1-\Psi\, ln(1-X)}-1\right] = \frac{k_{RPM}S_0(C_b-C_e)t}{2(1-\varepsilon_0)} \quad (2)$$

$$\frac{1}{\Psi}\left[\sqrt{1-\Psi\, ln(1-X)}-1\right] = \frac{S_0}{1-\varepsilon_0}\sqrt{\frac{D_{RPM}M_{CaO}C_b t}{2\rho_{CaO}Z}} \quad (3)$$

2.4 – Cooper Model

The general equation for reactive sorption from a gaseous stream can be written as a mass balance across a differential bed element, seen in Equation 4

$$v\left(\frac{\delta C}{\delta Z}\right)_t + \left(\frac{\delta C}{\delta t}\right)_Z + \frac{1-\varepsilon}{\varepsilon}\left(\frac{\delta q}{\delta t}\right)_Z = 0 \quad (4)$$

Where v is the axial interstitial velocity of the fluid, z is the axial distance coordinate in the direction of flow, C is the concentration of the contaminant in the bulk fluid, t is time, ε is the bed void fraction, and q is the average concentration of contaminant in the solid phase. This model assumes a plug flow, isothermal reactor, with negligible axial dispersion. The Cooper model assumes the linear driving force (LDF) in Equation 5

$$\left(\frac{\delta q}{\delta t}\right)_Z = k(q_0 - q) \quad (5)$$

Where k is the rate parameter and q_0 is the maximum capacity. The analytical solution to these equations ban be seen in Appendix 1. Ultimately the effluent concentration as a function of time becomes a function of experimental conditions and the parameter, k, and maximum

capacity, q_0. The excel solver function was used to minimize error between the experimental effluent gas concentration and the effluent concentration predicted by the Cooper model.

Chapter 3: Calcium Oxide Sorbent Studies

The properties and performance of calcium oxide sorbents were found to be highly dependent on synthesis precursor and technique. Conversions of calcium oxide ranged from 6-100%, at 873 K, by varying precursors (marble, calcium acetate, and calcium nitrate) and synthesis techniques (decomposition, hydrothermal treatment, and electrospinning). The choice of precursor and synthesis technique had a strong influence on the morphology, surface area, and pore volume of the materials which in turn led to these large changes in sorption capacity. Calcium oxide that was synthesized by thermal decomposition of calcium nitrate (CaO-D-nitrate) and calcium acetate (CaO-D-acetate) had very different material properties. The surface area and pore volume of CaO-D-nitrate and CaO-D-acetate were 7.6 and 17 $m^2\ g^{-1}$ and 0.003 and 0.110 $cm^3\ g^{-1}$, respectively. Hydrothermal treatment (CaO-H-nitrate) and electrospinning (CaO-nanofibers) using calcium nitrate precursor greatly improved the properties compared to thermal decomposition. The surface area and pore volume of CaO-H nitrate and CaO-nanofibers were 16 and 16 $m^2\ g^{-1}$ and 0.010 and 0.092 $cm^3\ g^{-1}$, respectively. SEM images of the three samples show that the particle size and agglomerates are largest for CaO-D-nitrate and are the smallest for CaO-nanofibers, conversely CaO-nanofibers have the largest macropores in the SEMs whereas CaO-D-nitrate had the minimal macroporosity. The sorption capacities determined via thermogravimetry were 0.05, 0.70, 0.58, and 0.79 $g_{CO2}\ g_{CaO}^{-1}$at 873 K for CaO-D-nitrate, CaO-D-acetate, CaO-H-nitrate, and CaO-nanofibers respectively at 873 K. The first order deactivation constant of samples synthesized using the calcium nitrate precursor were all the same and were more stable than CaO-D-acetate, indicating that for the SE-SMR process it would be less favorable to use calcium acetate precursors.

3.1 – Material Studies

Ca-based nanofibers were synthesized via electrospinning using polyvinylpyrrolidone (PVP) as the polymer component and $Ca(NO_3)_2$ as the calcium precursor. These materials were then thermally treated in air to remove PVP and convert $Ca(NO_3)_2$ to CaO (see Chapter 2). TGA experiments were conducted on the PVP-$Ca(NO_3)_2$ nanofibers to quantify the extent of PVP removal during the thermal treatment and provide evidence of the conversion to CaO. **Figure 5 (a)** shows the TGA curves of pure PVP and PVP-$Ca(NO_3)_2$ nanofibers. Pure PVP nanofibers were decomposed under argon at a heating rate of 10 K min^{-1}, whereas PVP-$Ca(NO_3)_2$ nanofibers were decomposed under air at a heating rate of 5 K min^{-1}. The heating rate was reduced in the case of PVP-$Ca(NO_3)_2$ to mimic the post-thermal treatment conditions described in Chapter 2. The nanofibers synthesized using pure PVP (MW = 1,300,000) decomposed under argon in two steps, with a total weight loss of ~95%. The first-step weight loss of 16% occurred between ambient temperature and 622 K. This weight loss step can be attributed to the evaporation of volatile solvents. The second-step weight loss of 79% from 623 to 763 K can be attributed to the thermal degradation of the polymer chains. It is clear from the TGA curve that the majority of the PVP matrix is removed at temperatures higher than 923 K. Additionally, PVP-$Ca(NO_3)_2$ nanofibers decompose under air in multiple steps, with a total weight loss of ~80%, **Figure 5 (b)**. The first step weight loss of 12% occurred between ambient temperature and 360 K and can be attributed to the evaporation of volatile solvents. The second weight loss of 27% from 580 to 620 K can be attributed to the combustion of PVP in the presence of oxygen. The third gradual weight loss of 14% from 620 to 770 K can be attributed to the oxidation of residual carbon remaining on the nanofibers. The final weight loss of 24% from 770 to 790 K

can be attributed to the decomposition of calcium nitrate, $Ca(NO_3)_2$, to CaO, indicating that the thermal treatments of PVP-$Ca(NO_3)_2$ nanofibers result in the formation of CaO nanofibers without residual carbon.

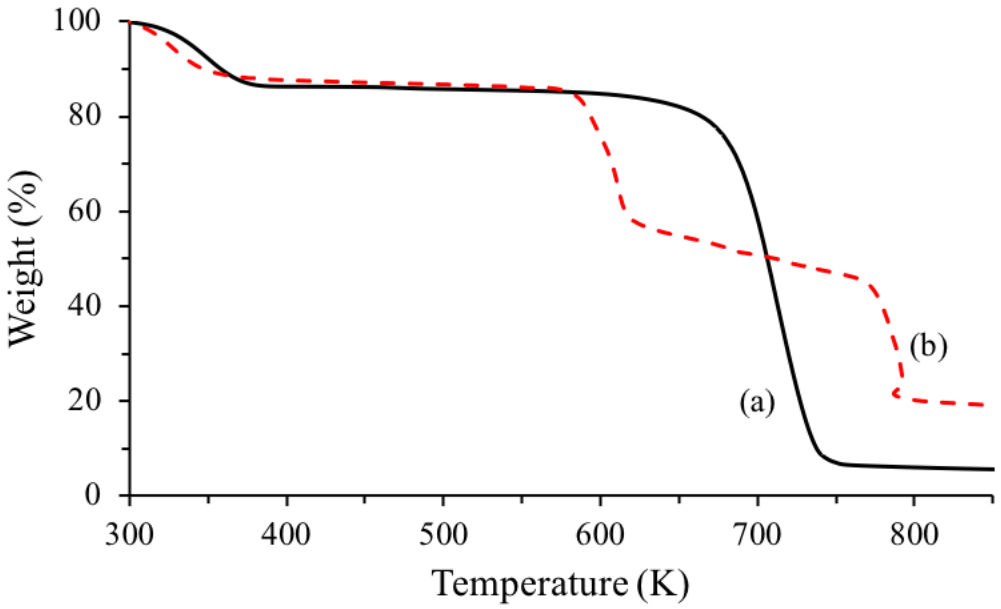

Figure 5. Thermogravimetric analysis (TGA) curves of (a) pure PVP nanofibers run under argon (straight, black) and (b) PVP-$Ca(NO_3)_2$ nanofibers run under air (dashed, red).

XRD was used to identify the crystalline phases and average crystal sizes of the CaO sorbents prepared using the synthesis techniques described in Chapter 2. **Figure 6** (black) shows the XRD patterns of the as-synthesized, PVP-$Ca(NO_3)_2$ nanofibers before thermal treatment at 923 K. Well-defined diffraction peaks are absent from the XRD pattern, which indicates that the nanofibers consist of amorphous polymer phases and calcium species that are too small to diffract X-rays. **Figure 6** also shows the XRD patterns of CaO-nanofibers (red), CaO-D-acetate (purple), CaO-D-nitrate (green), and CaO-H-nitrate (blue), after undergoing thermal treatment. **Figure 30**, in the appendix, shows the XRD patterns for CaO-marble and CaO-marble after the reaction-regeneration cycle. Crystalline peaks of CaO are identified with vertical dashed lines

and $Ca(OH)_2$ are identified with circles (●). $Ca(OH)_2$ was formed after the samples adsorbed moisture from the atmosphere because of the hygroscopic nature of CaO.[61] The edge length of the unit cell of the five CaO sorbents was calculated from the peak at $2\theta = 37°$ in XRD patterns. Each sample had a lattice parameter of 4.8 Å, confirming that the samples consist of cubic CaO. Average crystallite sizes were calculated from the peak at $2\theta = 37°$ using Scherrer's equation (**Table 4**). The average crystal domain sizes of CaO-nanofibers, CaO-D-acetate, CaO-D-nitrate, CaO-H-nitrate, and CaO-marble were 39 nm, 33 nm, 64 nm, 35 nm, and 84 nm, respectively, confirming that CaO derived from natural sources (in this case, marble) has significantly larger crystallite sizes than CaO derived from other sources. The XRD patterns of the CaO sorbents that have undergone multiple cycles of reaction with CO_2 followed by reaction with air (i.e., reaction–regeneration cycles) are shown in **Figure 6** (brown and gray) and **Figure 30** (red), in the appendix, and are discussed in subsequent sections.

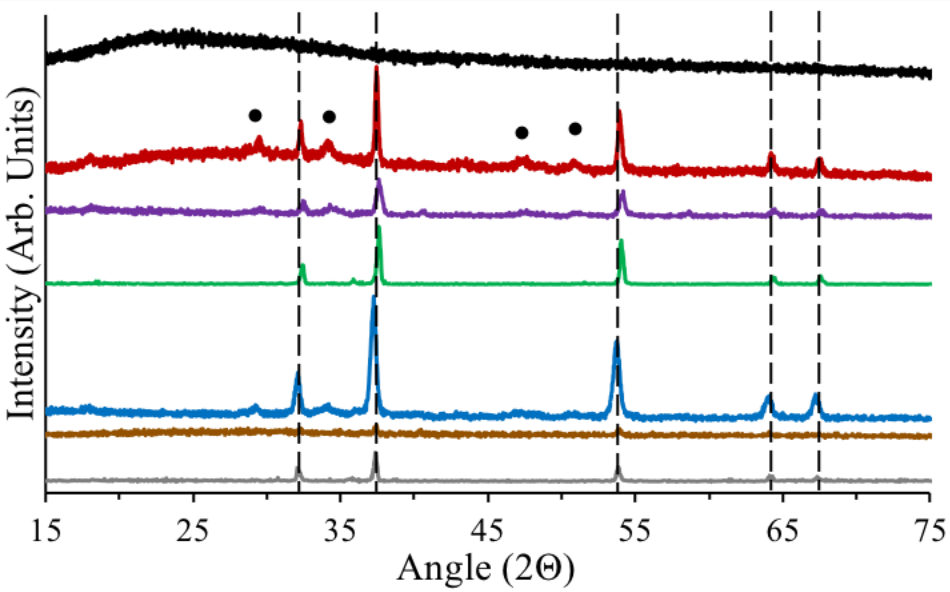

Figure 6. XRD patterns of (black) PVP-$Ca(NO_3)_2$ nanofibers (electrospinning), (red) CaO-nanofibers, (purple) CaO-D-acetate, (green) CaO-D-nitrate, (blue) CaO-H-nitrate, (brown) CaO-nanofibers after 10 carbonation-calcination cycles, and (gray) CaO-D-nitrate after 10 carbonation-calcination cycles.

Table 4. Properties of the CaO sorbents. (a) Based on BET method. (b) Based on BJH method. (c) Based on XRD.

Sorbent	S_{BET} ($m^2\ g^{-1}$) [(a)]	V_{pore} ($cm^3\ g^{-1}$) [(b)]	Pore Diameter (nm) [(b)]	Crystallite Size (nm) [(c)]	Post Cycle Crystallite Size (nm) [(c)]
CaO-marble	7.56	0.034	9.52	84	76
CaO-D-acetate	16.92	0.110	13.89	33	62
CaO-D-nitrate	4.8	0.003	2.7	64	73
CaO-H-nitrate	15.89	0.099	18.64	35	n/a
CaO-nanofibers	15.94	0.092	13.08	39	64

N_2-physisorption was used to determine the surface area, pore volume, and average pore diameter of the CaO samples (**Table 4**). The CaO-nanofibers (16 m^2 g^{-1}), CaO-D-acetate (17 m^2 g^{-1}), and CaO-H-nitrate (16 m^2 g^{-1}) samples exhibited more than twice the surface area of CaO-marble (7.6 m^2 g^{-1}) and more than three times the surface area of CaO-D-nitrate (4.8 m^2 g^{-1}). Similarly, the BJH pore volumes of the CaO-nanofibers (0.092 cm^3 g^{-1}), CaO-D-acetate (0.110 cm^3 g^{-1}), and CaO-H-nitrate (0.099 cm^3 g^{-1}) samples were a factor of three higher than the CaO-marble sample (0.034 cm^3 g^{-1}) and a factor of 30 higher than the CaO-D-nitrate sample (0.003 cm^3 g^{-1}). The chemically synthesized samples, with the exception of CaO-D-nitrate (2.7 nm), also had larger BJH average pore diameters (CaO-nanofibers: 13.1 nm, CaO-D-acetate: 13.9 nm, CaO-H-nitrate: 18.6 nm) compared with CaO-marble (9.5 nm). These data indicate that the techniques used to synthesize CaO from calcium nitrate (i.e., hydrothermal treatment and electrospinning) lead to highly porous materials that retain their pore structure even after thermal treatments to convert the calcium precursors to CaO.

SEM was used to probe the effect of synthesis technique and calcium source on sorbent morphology at the micrometer scale. **Figure 7a and b** show the SEM image (5,000 and 20,000 times magnification) of the as-synthesized PVP-$Ca(NO_3)_2$ nanofibers before thermal treatment. The electrospun fibers consisted of uniform, continuous, and smooth nanofibers with circular cross sections. The fibers had a narrow distribution with a mean diameter of 180 ± 57 nm, **Figure 8,** and lengths of up to several hundred micrometers. As seen from **Figure 7a**, a few spindle-like structural defects with an average diameter of 1.3 μm were present, and these defects were possibly formed from transient instabilities experienced by the travelling jet during the electrospinning process.[62,63] On thermal treatment at 923 K, CaO-nanofibers were obtained as

indicated by the XRD analysis (discussed previously). The post-thermally treated fibers (CaO-nanofibers) had a mean diameter of 208 ± 53 nm, **Figure 8d**. By comparing the SEM images of the nanofibers before (**Figure 7a and b**) and after thermal treatment (**Figure 7d**), it becomes clear that the thermal treatment transforms the PVP-$Ca(NO_3)_2$ fibers from smooth and continuous nanofibers, which are cylindrical in shape, to a network of nanoparticles that are closely connected in a nanofibrous structure with considerable macroporous (>300 nm diameter) intraparticle void volume. This change in morphology occurs, of course, because of the degradation of the polymer chains and the formation of CaO at these elevated temperatures.

Figure 7 also shows the SEM images of the remaining CaO sorbents (**(c)** CaO-marble, **(e)** CaO-D-nitrate, **(f)** CaO-H-nitrate, and **(g)** CaO-D-acetate) after undergoing thermal treatment. **Figure 7h and i** show CaO-marble and CaO-nanofibers, respectively, after 10 reaction–regeneration cycles. Both CaO-marble and CaO-D-nitrate had considerably large average agglomerate sizes, with the marble-derived sorbent having sizes of 835 ± 262 nm (measured from the SEM micrograph using ImageJ) and CaO-D-nitrate having agglomerates in the micrometer range. The agglomerate sizes of these two sorbents were a factor four or more larger than the other sorbents, with CaO-nanofibers having the smallest average agglomerate size of 184 ± 33 nm of the sorbents. Smaller agglomerate/particle sizes, in general, are believed to contribute to enhanced sorption performance due to their larger surface-to-volume ratios.[64] The SEM images in **Figure 7e and g** also reveal that CaO samples prepared from the decomposition of calcium acetate and nitrate and from the hydrothermal treatment of CaO (using calcium nitrate as a precursor) have uneven surface textures with considerably rough and sharp edges. On the other hand, the marble-derived CaO and CaO-nanofibers (**Figure 7c and d)** have well-defined,

rounder, and smoother structures, with the nanofibers having a noticeably smaller domain size and visibly larger macro-sized void volumes.

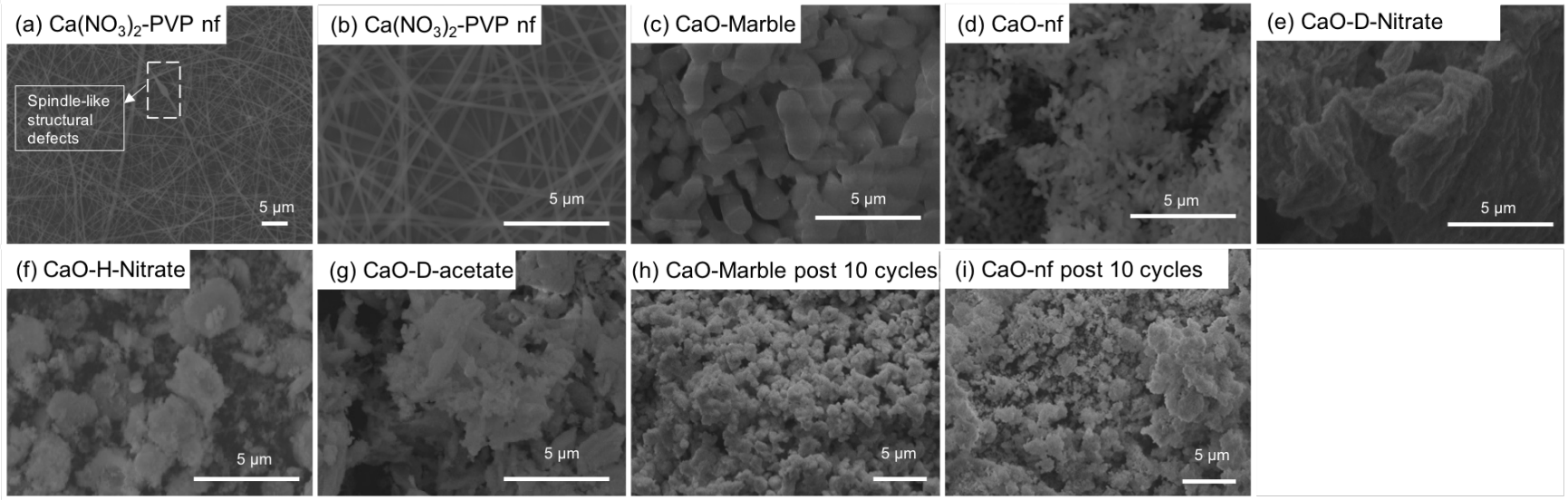

Figure 7. SEM images of as-synthesized PVP-$Ca(NO_3)_2$ nanofibers at (a) 5,000x and (b) 20,000x magnification, (c) CaO derived from marble, (d) CaO-nanofibers synthesized via electrospinning and thermally treated in air at 923 K, (e) CaO synthesized from thermal decomposition of calcium nitrate at 1023 K, (f) CaO synthesized from thermal decomposition of calcium nitrate at 1023 K followed by hydrothermal treatment, (g) CaO synthesized from thermal decomposition of calcium acetate in air 1023 K, (h) CaO-marble after 10 carbonation-regeneration cycles, and (i) CaO-nanofiber after 10 carbonation-regeneration cycles.

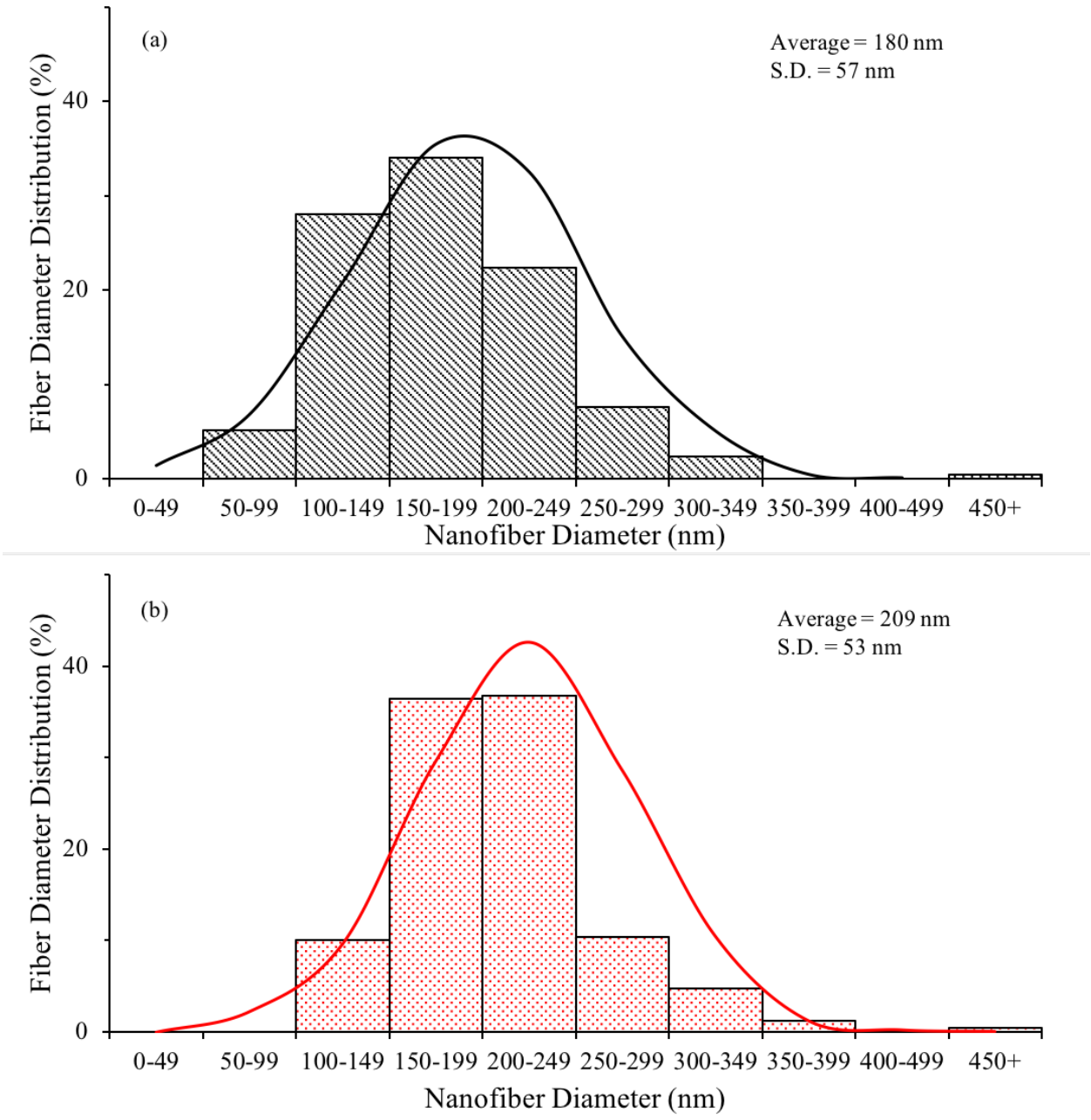

Figure 8. Diameter distribution and normal distribution of (a, black) PVP-$Ca(NO_3)_2$ nanofibers before thermal treatment and (b, red) CaO-nanofibers after thermal treatment at 923 K. The average diameter and standard deviation for the fibers were calculated using ImageJ (n=250) as described in Chapter 2.

TEM analysis (**Figure 9**) was performed on four CaO sorbents (CaO-marble, CaO-D-acetate, CaO-H-nitrate, and CaO-nanofibers) to supplement the SEM analysis and determine the

impact of synthesis approach on morphology. TEM image (**Figure 9a**) reveal that CaO derived from marble consists of large, closely packed and multilayered nanoparticles, with sizes ranging from roughly 50 to 180 nm. The CaO-H-nitrate (**Figure 9c**) and CaO-D-acetate samples (**Figure 9d**) had comparatively smaller nanoparticles (~25–120 nm) than CaO-marble. The electrospun CaO-nanofibers (**Figure 9b**) had nanoparticles with diameters ranging from 70–180 nm; however, they contained significantly larger macroporous intraparticle void volumes. These intraparticle spaces appear as void channels (inset of **Figure 9b**) and have diameters that are on the order of 0.5 μm.

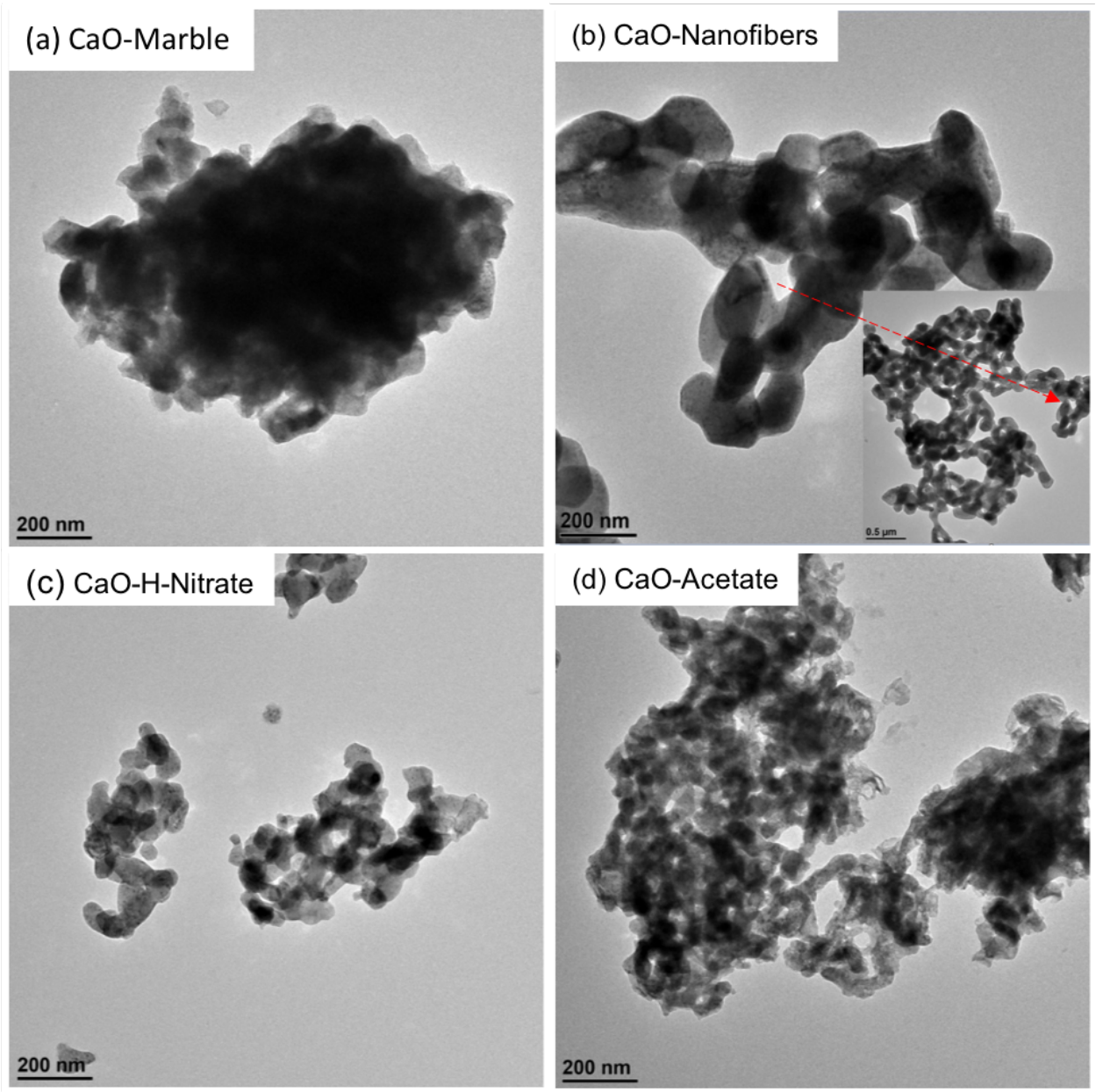

Figure 9. TEM images of the sorbents: (a) CaO-marble, (b) CaO-nanofibers, (c) CaO-H-nitrate, and (d) CaO-D-acetate.

3.2 – Material Studies – CO_2 Sorption Properties

TGA experiments were conducted on the five CaO samples (CaO-marble, CaO-D-acetate, CaO-D-nitrate, CaO-H-nitrate, and CaO-nanofibers) to compare their CO_2 sorption capacity and reaction rates. **Figure 10** shows the first-cycle carbonation reaction curves (in terms of conversion of CaO to $CaCO_3$ and capacity (g_{CO_2} g_{CaO}^{-1}) vs time on stream) at three temperatures (823, 873, and 923 K). The conversion of CaO has two stages: a fast chemical reaction–controlled stage followed by a slower increase that is controlled by the diffusion of molecules (and possibly atoms) through solid product layers.[65] TGA experiments were stopped after 60 min because at this time the conversion seems to approach a constant value with increasing time on stream.

The differences in conversion among the five samples (seen in **Figure 10**) indicate the effect of morphological features and physiochemical properties on CO_2 sorption. CaO-marble, a sample that has large agglomerate, particle, and crystallite sizes as well as a low surface area and intraparticle void volume (as discussed previously), exhibited conversions of 20% (0.17 g_{CO_2} g_{CaO}^{-1}) at 823 K, 18% (0.14 g_{CO_2} g_{CaO}^{-1}) at 873 K, and 32% (0.25 g_{CO_2} g_{CaO}^{-1}) at 923 K, in agreement with previous studies.[6,66] Additionally, CaO-D-nitrate, another sample with a relatively large crystallite size and small surface area and pore volume (an order of magnitude smaller than CaO-marble as shown in **Table 4**), exhibited conversions of 6.5% (0.05 g_{CO_2} g_{CaO}^{-1}) at 823 K, 6.5% (0.05 g_{CO_2} g_{CaO}^{-1}) at 873 K, and 8% (0.06 g_{CO_2} g_{CaO}^{-1}) at 923 K. The decrease in reactive surface area and pore volume for CO_2 diffusion resulted in approximately a fourfold decrease in conversion. On the other hand, the CaO samples synthesized from the decomposition

of calcium acetate (CaO-D-acetate) and hydrothermal treatment of CaO (CaO-H-nitrate) exhibited more than threefold higher conversions than CaO-marble and CaO-D-nitrate at all temperatures, with CaO-nanofibers achieving stoichiometric CO_2 capacity (0.79 g_{CO_2} g_{CaO}^{-1}) in less than 1 h of reaction at both 873 and 923 K. The higher conversion of the CaO-D-acetate, CaO-H-nitrate, and CaO-nanofibers provides evidence to support the conclusion that structures with small crystallites and high porosity (high surface area and intraparticle void volume) enhance the reactivity of CaO materials and reduce their susceptibility to transport limitations from the formation of product layers that cover surfaces and fill pores.

The CaO-nanofiber sample also exhibited higher capacity (0.79 g_{CO_2} g_{CaO}^{-1} at 873 and 923 K) compared with CaO-D-acetate (0.70 and 0.77 g_{CO_2} g_{CaO}^{-1} at 873 and 923 K, respectively) and CaO-H-nitrate (0.59 and 0.62 g_{CO_2} g_{CaO}^{-1} at 873 and 923 K, respectively). These three samples all consisted of similar particle and crystallite sizes, surface areas, and mesopore volumes (**Table 4**); therefore, the higher capacity of the nanofibers could potentially be attributed in part to the larger macroporosity (i.e., particle void spaces and intraparticle channels) within the nanofiber networks imparted by the electrospinning synthesis technique as shown via TEM in **Figure 9b**. Furthermore, the CaO-H-nitrate sample synthesized by hydrothermal treatment in our studies exhibited a much higher conversion (73% at 873 K) compared with the thermally decomposed $Ca(NO_3)_2$ (CaO-D-nitrate) (6.5% at 873 K). The low conversion of CaO synthesized from the simple thermal decomposition of $Ca(NO_3)_2$ (CaO-D-nitrate) is consistent with the values reported by Lu et al.[67] (2.5%) for such materials. Therefore, the studies reported herein indicate that the synthesis technique plays a pivotal role in dictating the sorbent capacity of a CaO-based material by controlling the morphology and properties such as crystallite size,

surface area, pore volume, pore diameter, and intraparticle void volumes. Hydrothermal treatment and electrospinning were found to alter the macroporosity of the sample (pores on the order of 0.5 μm as identified in SEM and TEM images); introduction of these macropores possibly abates diffusional restrictions from pore filling and surface coverage effects, thus leading to higher sorption capacities.

3.3 – Sorption Kinetic Modeling

To quantify the observed differences in performance described in the previous paragraphs, the results from the TGA experiments were analyzed using the random pore model (RPM; Chapter 2). The RPM models the rate of change of pore radii at the initial stages of conversion using a reaction rate equation that is first order in the concentration of CO_2 and normalized by the surface area of the material. Thus, the reaction rate constant (k_{RPM}) in this equation is also normalized by surface area and reflects the rate of chemical reaction at the surface. Nonreactive $CaCO_3$ surfaces serve as diffusional barriers, and as these nonreactive product surfaces grow and intersect with each other, the system transitions into a diffusion-controlled regime. The effective diffusivity (D_{RPM}) quantitatively characterizes this regime and reflects the differences in the product layer thickness and penetrability.

Values for k_{RPM} and D_{RPM} (**Table 5**) were determined using parameter estimation in Athena Visual Studio. RPM model predictions (lines) are shown in **Figure 10** (overlaid with experimental conversion data points). The largest deviation of the model from the experimental data comes at the transition from the kinetic reaction regime to the diffusion reaction regime. This is because the model describing this reaction has one equation for the kinetic regime and

one for the diffusive regime. In reality there is a short period of time where the carbonation is not completely kinetic or diffusion controlled this results in the small deviation between the model and experimental data.

The rate constants exhibit an exponential dependence on inverse temperature (**Figure 11**), and the activation energies for the reaction (E_a = 9, 20, 31, and 73 kJ mol^{-1} for CaO-D-nitrate, CaO-marble, CaO-D-acetate, and CaO-nanofibers, respectively) are within similar ranges as in the previous studies (E_a = 28.4 kJ mol^{-1} as reported by Zhou et al.[68]). Values for k_{RPM} for CaO-H-nitrate (2.5 x 10^{-4} ± 1.2 x 10^{-6} and 3.1 x 10^{-4} ± 1.7 x 10^{-6} cm^4 mol^{-1} s^{-1} at 873 and 923 K, respectively) are similar to those for CaO-D-nitrate (2.1 x 10^{-4} ± 1.1 x 10^{-6} and 2.3 x 10^{-4} ± 1.3 x 10^{-5} cm^4 mol^{-1} s^{-1} at 873 and 923 K, respectively) and CaO-marble (3.1 x 10^{-4} ± 1.2 x 10^{-6} and 3.8 x 10^{-4} ± 2.0 x 10^{-6} cm^4 mol^{-1} s^{-1} at 873 and 923 K, respectively), as expected for materials that are chemically similar (i.e., crystalline CaO). However, the D_{RPM} values for CaO-H-nitrate (4.7 x 10^{-12} ± 1.9 x 10^{-14} and 3.6 x 10^{-12} ± 5.1 x 10^{-14} cm^2 s^{-1} at 873 and 923 K, respectively) are 5–10 times larger than CaO-marble (2.0 x 10^{-13} ± 1.0 x 10^{-15} and 9.0 x 10^{-13} ± 5.0 x 10^{-15} cm^2 s^{-1} at 873 and 923 K, respectively). Additionally, the D_{RPM} values for CaO-D-nitrate (2.0 x 10^{-14} ± 1.0 x 10^{-15} and 4.0 x 10^{-14} ± 6.0 x 10^{-15} cm^2 s^{-1} at 873 and 923 K, respectively) are approximately an order of magnitude smaller than those for CaO-marble. Thus, we conclude that the modification of CaO via hydrothermal treatment in the presence of P123 leads to CaO domains with similar reactivity as CaO-D-nitrate and CaO-marble, but the CaO-H-nitrate sample exhibits better conversion during carbonation because of smaller domain sizes (crystallites and particles) and higher porosity.

In contrast to CaO-H-nitrate, the higher k_{RPM} values (**Table 5**) for CaO-D-acetate (3.2 x 10^{-4} ± 1.4 x 10^{-5}, 5.0 x 10^{-4} ± 2.5 x 10^{-6}, and 5.2 x 10^{-4} ± 4.8 x10^{-6} cm^4 mol^{-1} s^{-1} at 823, 873, and 923 K, respectively) and CaO-nanofibers (4.6 x 10^{-4} ± 4.2 x 10^{-6}, 8.9 x 10^{-4} ± 1.8 x 10^{-5}, and 1.5 x10^{-3} ± 9.5 x10^{-6} cm^4 mol^{-1} s^{-1} at 823, 873, and 923 K, respectively) compared with CaO-marble indicate a difference in the surface chemistry of the reaction despite their chemical similarity (i.e., crystalline CaO), beyond the effects of superior pore structure that ameliorates diffusion restrictions. This enhanced reactivity with decreasing particle size, similar to that observed in catalysis by metal particles,[69,70] may result from the preferential exposure of high index planes that comprise smaller crystallites[71] or from CaO structures that are inherently imparted by the synthesis technique with lesser extents of long range order. Values of D_{RPM} are also larger for CaO-D-acetate (4.2 x 10^{-12} ± 5.6 x 10^{-14}, 1.4 x 10^{-11} ± 3.7 x 10^{-14}, and 7.8 x 10^{-12} ± 2.1 x 10^{-13} cm^2 s^{-1} at 823, 873, and 923 K, respectively) and CaO-nanofibers (7.2 x 10^{-12} ± 1.9 x 10^{-14}, 4.3 x 10^{-11} ± 3.0 x 10^{-13}, and 5.5 x 10^{-11} ± 8.2 x 10^{-13} cm^2 s^{-1} at 823, 873, and 923 K, respectively) compared with CaO-marble (**Table 5**) indicating the effect of smaller reactive domains and possibly the formation of thinner $CaCO_3$ layers with structures that are more easily penetrable by gaseous CO_2.[72–74]

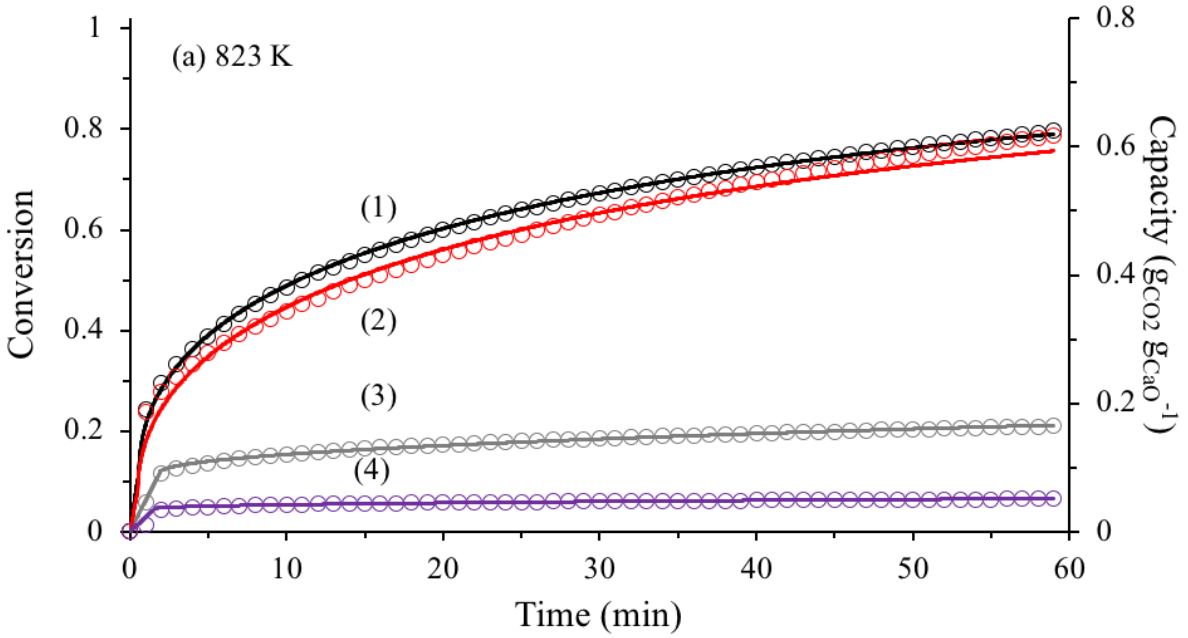
(a) 823 K
Conversion
Capacity (g_{CO2} g_{CaO}^{-1})
Time (min)
(1)
(2)
(3)
(4)
0
0.2
0.4
0.6
0.8
1
0
10
20
30
40
50
60

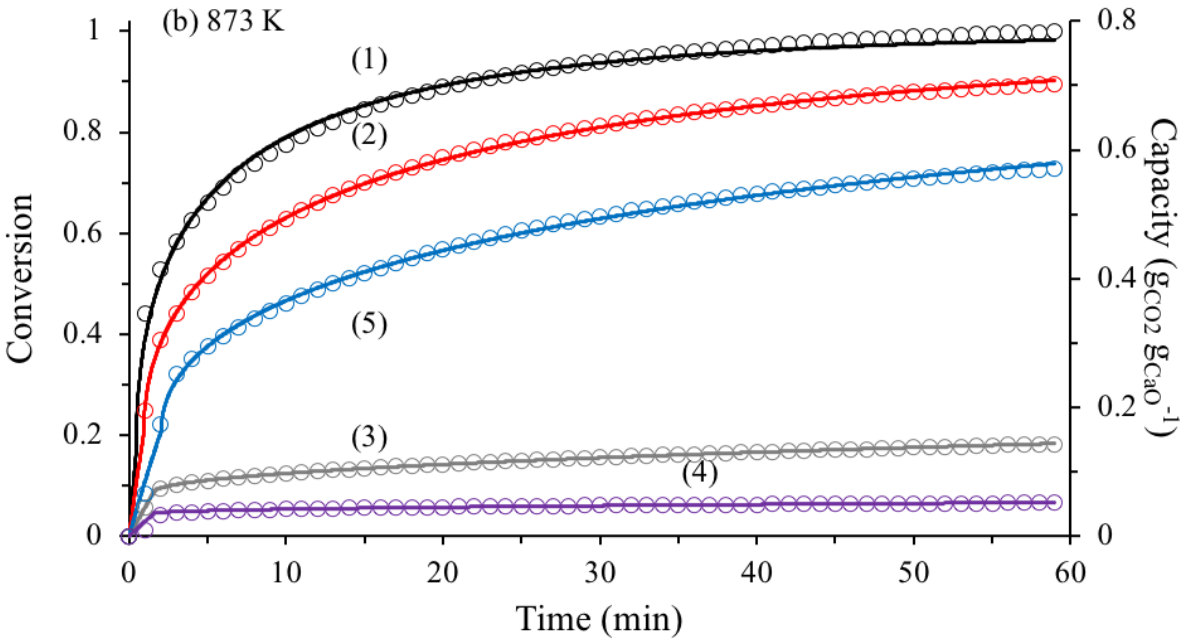
(b) 873 K
Conversion
Capacity (g_{CO2} g_{CaO}^{-1})
Time (min)
(1)
(2)
(5)
(3)
(4)
0
0.2
0.4
0.6
0.8
1
0
10
20
30
40
50
60

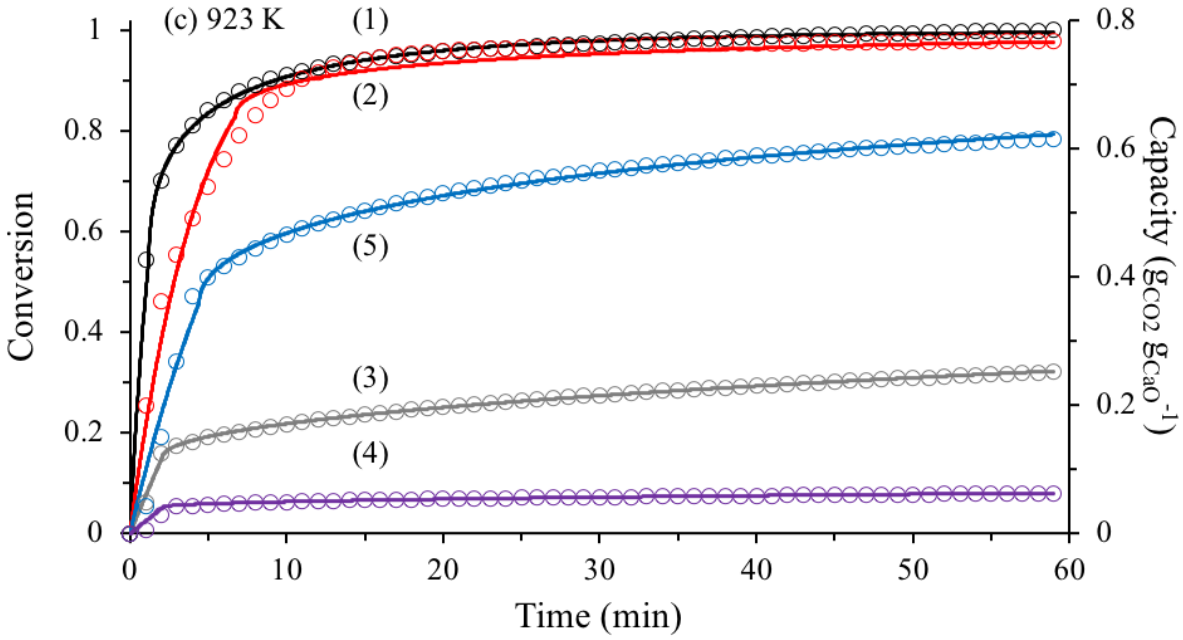

Figure 10. Experimental conversion and sorption capacities (hollow circles) and RPM prediction of conversion (solid lines) for (1) CaO-nanofibers, (2) CaO-D-acetate, (3) CaO-marble, and (4) CaO-D-nitrate, and (4) CaO-H-nitrate measured by TGA at (a) 823 K, (b) 873 K, and (c) 923 K, 1 atm, and 200 sccm of CO_2.

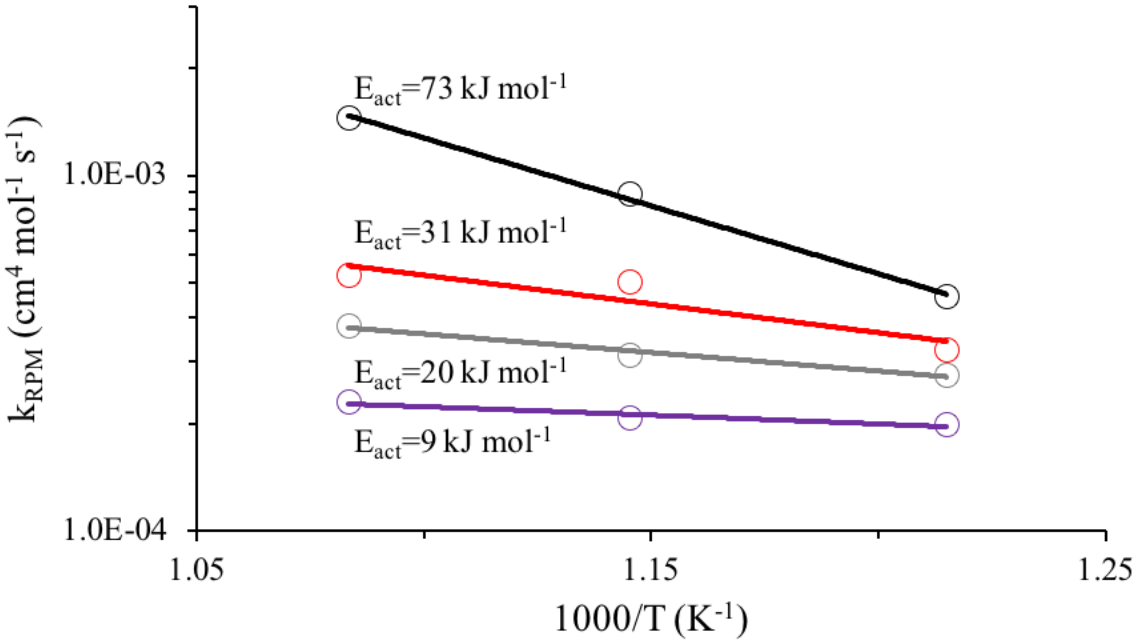

Figure 11. Arrhenius plots for reaction of CaO-nanofibers (black), CaO-D-acetate (red), CaO-marble (gray), and CaO-D-nitrate (purple). Circles represent experimentally determined reaction rate parameters for the random pore model determined from regression of conversion versus time data. Activation energies were determined by least squares regression of the experimentally determined parameters (lines).

Table 5. RPM parameters and 95% confidence intervals derived from the carbonation data in Figure 10.

Sample	823 K		873 K		923 K	
	k_{RPM} ($x10^4$) ($cm^4\ mol^{-1}\ s^{-1}$)	D_{RPM}($x10^{12}$) ($cm^2\ s^{-1}$)	k_{RPM} ($x10^4$) ($cm^4\ mol^{-1}\ s^{-1}$)	D_{RPM}($x10^{12}$) ($cm^2 s^{-1}$)	k_{RPM} ($x10^4$) ($cm^4\ mol^{-1}\ s^{-1}$)	D_{RPM} ($x10^{12}$) ($cm^2 s^{-1}$)
CaO-marble	2.8 ± 0.007	0.2 ± 0.002	3.1 ± 0.012	0.2 ± 0.001	3.8 ± 0.020	0.9± 0.005
CaO-D-acetate	3.2 ± 0.135	4.2 ± 0.056	5.0 ± 0.025	13.6 ± 0.037	5.2 ± 0.048	7.8 ± 0.206
CaO-D-nitrate	2.0 ± 0.010	0.02 ± 0.001	2.1 ± 0.011	0.02 ± 0.001	2.3 ± 0.134	0.04 ± 0.006
CaO-H-nitrate	-	-	2.5 ± 0.012	4.7 ± 0.019	3.1 ± 0.017	3.6 ± 0.051
CaO-nanofibers	4.6 ±0.042	7.2 ± 0.019	8.9 ± 0.177	42.9 ± 0.298	14.5 ± 0.095	55.0 ± 0.822

3.4 – Stability Studies

Ten cycles of carbonation and calcination were performed to study the stability of the CaO sorbents (CaO-marble, CaO-D-nitrate, CaO-D-acetate, and CaO-nanofibers) and the reversibility of the carbonation reaction. CaO-marble lost 1% (0.2 mg) of its initial sorption capacity after the first carbonation–oxidation cycle. **Figure 12** shows the sorption capacity of CaO-marble, CaO-D-nitrate, CaO-D-acetate, and CaO-nanofibers over 10 carbonation and calcination cycles. The CaO-marble reached 12% (0.10 g_{CO_2} g_{CaO}^{-1}) conversion on its 10th carbonation cycle, losing ~34% of its initial capacity. The CaO-D-nitrate reached 4.5% (0.036 g_{CO_2} g_{CaO}^{-1}) conversion on its 10th carbonation cycle, losing ~30% of its initial capacity. The CaO-D-acetate reached 29% (0.23 g_{CO_2} g_{CaO}^{-1}) conversion on its 10th carbonation cycle, losing ~66% of its initial capacity. The electrospun CaO sorbent reached 69% (0.54 g_{CO_2} g_{CaO}^{-1}) conversion on its 10th carbonation cycle, losing 31% of its initial capacity. The CaO-nanofibers sorbent retains a relatively high capacity even after 10 cycles of carbonation–calcination, although its loss of initial capacity is proportionally similar to CaO-marble and CaO-D-nitrate.

CaO samples after reaction–regeneration cycles (CaO-marble, CaO-D-nitrate, and CaO-nanofibers) were also treated at 923 K for 8 h at 5 K min^{-1} to minimize the impact of hydroxide formation via exposure to ambient air and immediately analyzed using XRD, as seen in **Figure 30** (red), in the appendix, and **Figure 6** (brown and gray). The crystallite sizes of the sorbents after these cycles (**Table 4**) were calculated based on the peak at $2\theta = 37°$. The calculated crystallite sizes of CaO-marble, CaO-D-nitrate, CaO-D-

acetate, and CaO-nanofibers were 76 nm, 73 nm, 62 nm, and 64 nm, respectively. The crystallite sizes of CaO-marble and CaO-D-nitrate remained relatively unchanged after cycling because the formation of this sample likely occurred at conditions that led to sintering and agglomeration. In contrast, the crystallite sizes of CaO-D-acetate and CaO-nanofibers increased from 33 nm to 62 nm and 39 nm to 64 nm, respectively. The sintering and aggregation of the crystallites in the CaO-D-acetate and CaO-nanofibers are likely the reason for the loss in activity of the sorbent over repeated cycles in addition to possible loss of pore structure and volume.[31,75,76]

SEM analysis, as discussed previously, was also performed on the cycled CaO-marble and CaO-nanofibers samples to investigate the effect of multiple reaction–regeneration cycles on morphology (**Figure 7 (h, i)**). The SEM images of the thermally treated CaO-marble (**Figure 7 (h)**) and CaO-nanofibers (**Figure 7 (i)**) reveal that cycling detrimentally affected the morphology of the oxide fibers, especially the CaO-nanofiber sample that underwent drastic structural and morphological changes. Specifically, the SEM image shows that upon cycling, the CaO-nanofibers sample lost its porous, fibrous structure, which was initially responsible for mitigating pore plugging. This loss of nanoscale structure results in the reduction seen in the sorption capacity of CaO-nanofibers upon multiple cycling. The post-cycle SEM images also reveal that after 10 cycles both samples consisted of agglomerated, irregularly shaped nanoparticles. Therefore, although electrospinning results in the formation of CaO nanostructures that are highly active, repeated calcinations collapse the fibrous structure, and strategies such

as metal doping may be required to maintain the morphology and thus the initial high sorption capacity of the active materials prepared via electrospinning.

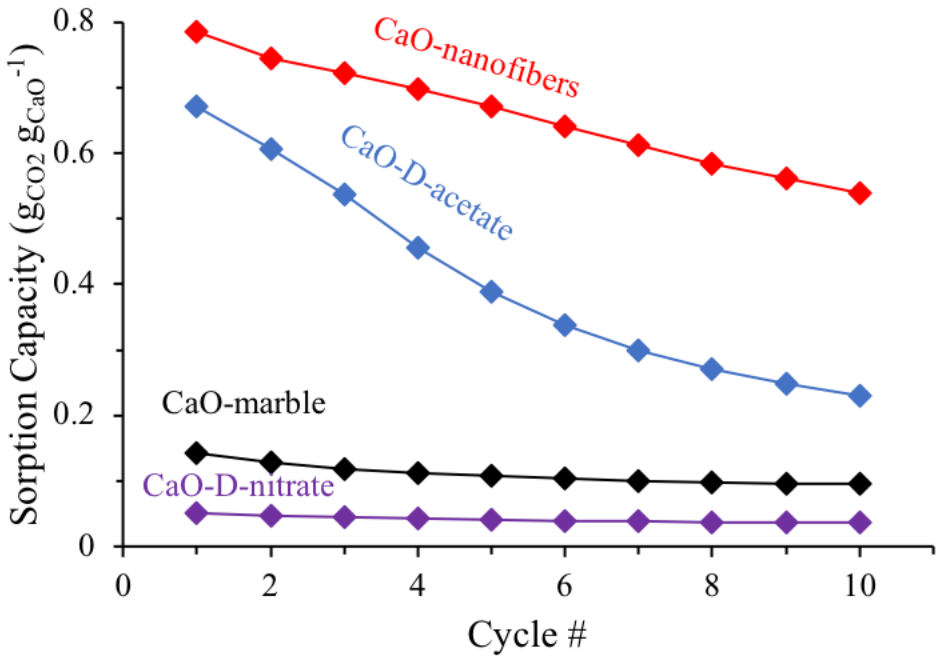

Figure 12. Sorption capacity of CaO-marble (black), CaO-D-nitrate (purple), CaO-D-acetate (blue), and CaO-nanofibers across ten reaction-regeneration cycles at 873 K, 101 kPa, and 200 sccm of CO_2 via TGA.

Chapter 4: Metal Additive Stabilized CaO-nanofibers

High capacity electrospun calcium oxide-based sorbents were modified with additive oxides to improve the material stability. Metal additives (Al, Co, Cr, Er, Ga, In, La, Li, Mg, Nd, Y, Zn) at nominal 3:10 (M:Ca) ratios were investigated for their ability to stabilize calcium oxide nanofibers over repeated carbonation-regeneration cycles at mild conditions. Samples containing Mg, Y, Nd, La, and Er additives had maximum sorption capacities from 0.40-0.60 g_{CO2} $g_{sorbent}^{-1}$, compared to 0.79 g_{CO2} $g_{sorbent}^{-1}$ for CaO. Y, Al, Er, and Nd were most effective for improving the stability of CaO, each had first order deactivation constants that were at least one order of magnitude smaller compared to CaO. Post-carbonation characterization revealed that particle agglomeration and structure degradation were the primary reasons for loss in capacity over repeated carbonation-regeneration cycles. Similar to observations with pure CaO, materials with large macropores, small agglomerates, and high porosity had higher capacities; however, in this study these properties also led to higher stability. Sorbents with additive oxide Tammann temperatures greater than the maximum treatment temperature had conversions approaching 100%, sorbent stability also increased with additive oxide Tammann temperature. Sorbents with low additive oxide Tammann temperature sintered, and thus suffered structural damage, prior the first carbonation. Likewise, sorbents with high additive oxide Tammann temperature had increased resistance sintering and structural damage over repeated carbonation-regeneration cycles. Formation of mixed oxides were found to be undesirable for sorbent performance because it behaves the same as other oxides but consumes calcium in its formation.

4.1 – Material Characteristics

Calcium oxide nanofibers were modified with metal additives via incorporating the corresponding additive metal nitrate in the electrospinning solution (described in Chapter 2), in a 3:10 (M:Ca) ratio, for the following metals: (Al, Co, Cr, Er, Ga, In, La, Li, Mg, Nd, Y, and Zn).

Incorporating that additive oxide decreases the sorption capacity on a per gram basis due to the dilution of calcium oxide. Further, since the dilution is on an atomic basis, the heavier the additive oxide molecular mass the lower the maximum theoretical capacity of the modified sorbent. When discussing the *maximum theoretical capacity*, it refers to the stoichiometric capacity of the modified sorbent, on a per gram basis, corrected for the dilution of calcium oxide.

Some of the additive oxides form mixed oxides, $M_xCa_yO_z$, with calcium oxide as will be identified and discussed at length below. The incorporation of calcium oxide in to the mixed oxide results in the consumption of calcium oxide that would otherwise be available for carbonation. For the sorbents where mixed oxides were identified via XRD, *a corrected theoretical capacity,* assumes that all of the additive metal formed a mixed oxide with calcium oxide. The corrected theoretical capacity is, in other words, the "minimum" stoichiometric capacity of the modified sorbent, on a per gram basis, because it assumes the maximum amount of calcium consumed by the additive metal.

4.2 – Physical and Chemical Properties of Additive-Modified Nanofibers

Figure 13 shows the SEM images of the modified CaO-nanofibers tested in this study both before and after carbonation. The SEMs are roughly grouped by unstable and/or low capacity, high stability/moderate capacity, and moderate stability and capacity. SEMs comparing the samples of different aluminum loadings can be seen in the appendix, **Figure 32**, because of the materials similarities, among the samples discussion will focus on 1Al-20Ca-O.

Figure 13 a, c, e, g, and i show fresh SEM images of the CaO, 3Zn-10Ca-O, 3Cr-10Ca-O, 3Li-10Ca-O, and 3Co-10Ca-O nanofibers which exhibited first order deactivation constants greater than 0.019 $cycle^{-1}$ and/or initial capacities less than 0.3 $g_{CO2}\ g_{sorbent}^{-1}$. Similarly, fresh SEM images of 1Al-20Ca-O, 3Y-10Ca-O, 3Er-10Ca-O, 3Nd-10Ca-O, 3La-10CaO, 3In-10Ca-O, and 1Mg-2Ca-O have low deactivation constants (less than $6.0x10^{-3}$ $cycle^{-1}$) and/or highest initial capacities (greater than 0.40 $g_{CO2}\ g_{sorbent}^{-1}$), are shown in **Figure 13 k, m, o, q, s, u, and x**. Images of the samples are shown before and after 10-16 carbonation-regeneration cycles to probe (i) how initial morphology impacts initial capacity and (ii) how repeated cycling changes the physical morphology of the materials. The SEM images reveal that the samples with large deactivation constants and low capacities (3Zn-10Ca-O (**Figure 13c**), 3Cr-10Ca-O (**Figure 13e**), 3Li-10Ca-O (**Figure 13g**), and 3Co-10Ca-O (**Figure 13i**)) are characterized by large particles, by significant agglomeration after cycling, and by smooth structures that are interconnected. In contrast, the top performing samples, 1Al-20Ca-O (**Figure 13k**), 3Y-10Ca-O (**Figure 13m**), 3Er-10Ca-O (**Figure 13o**), and 3Nd-10Ca-O (**Figure 13q**) each possess small particle sizes with highly microporous and

textured structures, and each exhibits minimal agglomeration after carbonation-regeneration cycling. Small particle sizes/agglomerates have previously been attributed to increases in sorption capacity due to larger surface area to volume ratios,[77] and Chapter 3 demonstrated that metal oxide the macroporous structure, pore volume, and surface area also has a significant impact on capacity. Furthermore, the materials tested in this study that exhibit higher initial capacity and smaller deactivation constants are also comprised of metal additives whose oxides possess higher Tammann temperatures. Thus, we conclude that Tammann temperature of the metal oxide additive may also impact initial capacity as well as preventing breakdown of the macroporous structure and agglomeration of CaO crystallites. This topic will also be discussed in more detail subsequently.

To further probe the effect of additives on sorbent performance, XRD scans were collected for each modified CaO sample before carbonation cycle testing, as seen by the patterns in **Figure 14**. The peaks at 2θ=37°, 54°, 64°, and 68° are attributed to pure calcium oxide. Peaks indicating the metal oxide of the additive are denoted with circles (e.g., 3La-10Ca-O forms a physical mixture of La_2O_3 and CaO). Some additive metals formed mixed oxides or are present in an anion form (e.g., 3In-10Ca-O formed $CaIn_2O_4$ whereas 3Cr-10Ca-O formed $CaCrO_4$). Peaks for these mixed oxides are denoted with a star symbol. The peak at 2θ=37° was used to calculate the crystallite size of CaO before and after cycling the samples in the TGA. A summary of the crystallite sizes before carbonation cycling is shown in **Table 6**. Calcium oxide sorbents containing Mg, Zn, and Y had the smallest CaO crystallite sizes at 26.5, 27.6, and 35.5 nm, respectively. Crystallite sizes of

the additive or mixed oxide species were also calculated to determine if there were any trends with oxide crystallites in terms of stability or capacity (peaks used for calculations are listed in **Table 9** in the appendix). XRD spectra of spent materials (i.e., after cycling) were collected after an ex-situ thermal treatment at 1073 K for 2 hr and are shown as dotted lines in **Figure 14**. Crystallite sizes of CaO and the additive oxides after cycling are also shown in **Table 6**. The post-cycle XRD spectra will be discussed in the section on sorbent stability.

Various additives consume CaO by forming a mixed oxide or by forming an anion with oxygen, CrO_4^{2-}. All additives that formed a mixed oxide are of the form $Ca_xM_yO_z$ and were a mixture of CaO and M_2O_3. The samples that formed mixed oxides include: 3Co-10Co-O, 3Ga-10Ca-O, and 3In-10Ca-O in the form of $Ca_3Co_2O_6$, $Ca_5Ga_6O_{14}$, and $CaIn_2O_4$. Aluminum additives in the following samples (3Al-10Ca-O, 1Al-10Ca-O, and 1Al-20Ca-O) exist as some mixture of Al_2O_3 and $Ca_{12}Al_{14}O_{33}$. The formation of $Ca_3Al_2O_6$ is also a possibility based on the XRD patterns in **Figure 14** (**Figure 33** in appendix contains all Al containing samples). Specifically, the XRD spectra confirm the presence of pure CaO along with the next most dominant peak at $2\theta=30°$ which is shared by $Ca_{12}Al_{14}O_{33}$ and $Ca_3Al_2O_6$. Other minor peaks, like $2\theta=36°$, are associated with mayenite. Previous papers found that $Ca_3Al_2O_6$ is not formed until temperatures above 1273 K are reached, which exceeds the maximum temperature this sample was exposed to, 1173 K.[78] Further discussion of the implications of the identity of the aluminum phase in the aluminum modified samples will be discussed in the two subsequent sections.

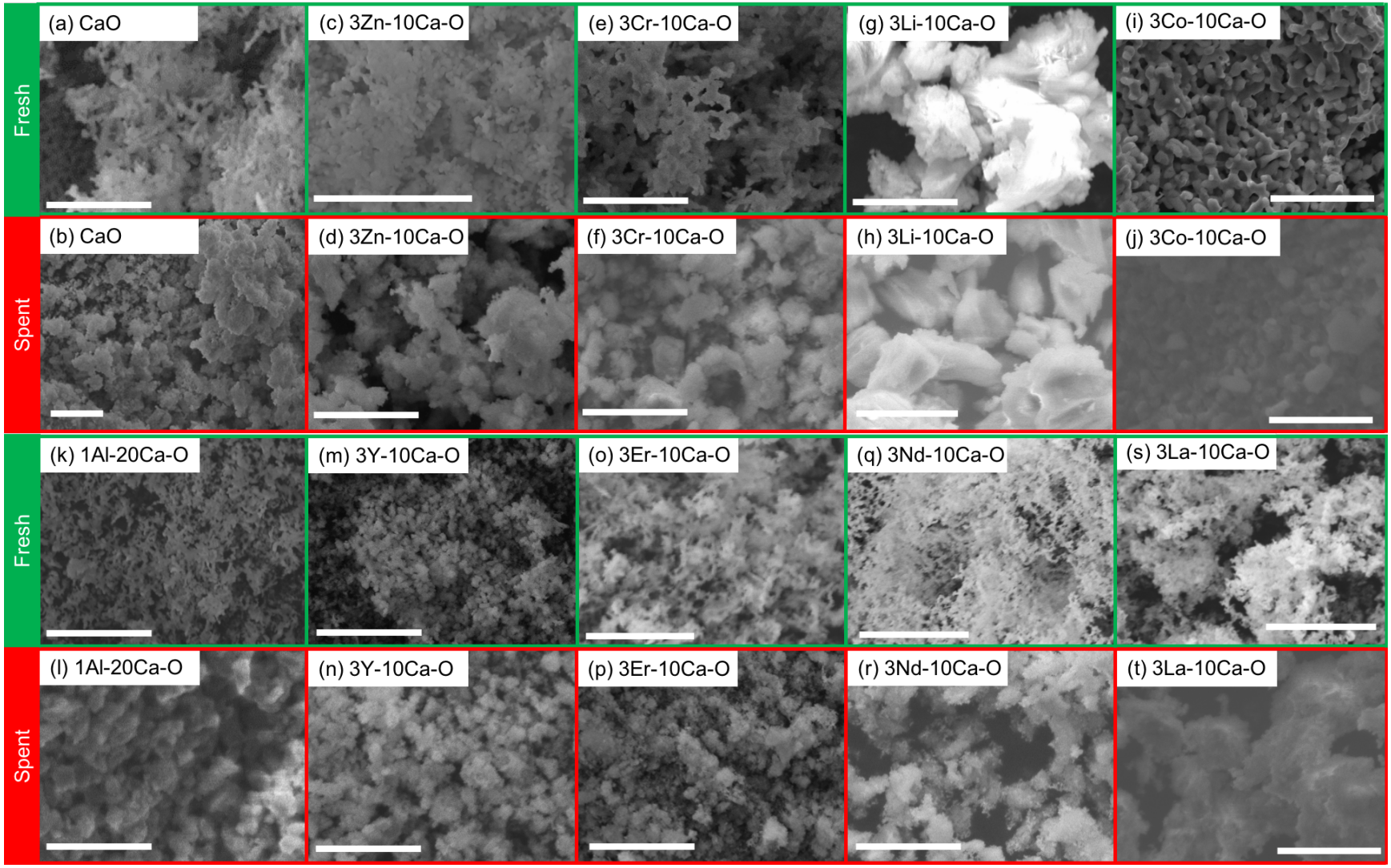
Fresh
(a) CaO
(c) 3Zn-10Ca-O
(e) 3Cr-10Ca-O
(g) 3Li-10Ca-O
(i) 3Co-10Ca-O
Spent
(b) CaO
(d) 3Zn-10Ca-O
(f) 3Cr-10Ca-O
(h) 3Li-10Ca-O
(j) 3Co-10Ca-O
Fresh
(k) 1Al-20Ca-O
(m) 3Y-10Ca-O
(o) 3Er-10Ca-O
(q) 3Nd-10Ca-O
(s) 3La-10Ca-O
Spent
(l) 1Al-20Ca-O
(n) 3Y-10Ca-O
(p) 3Er-10Ca-O
(r) 3Nd-10Ca-O
(t) 3La-10Ca-O

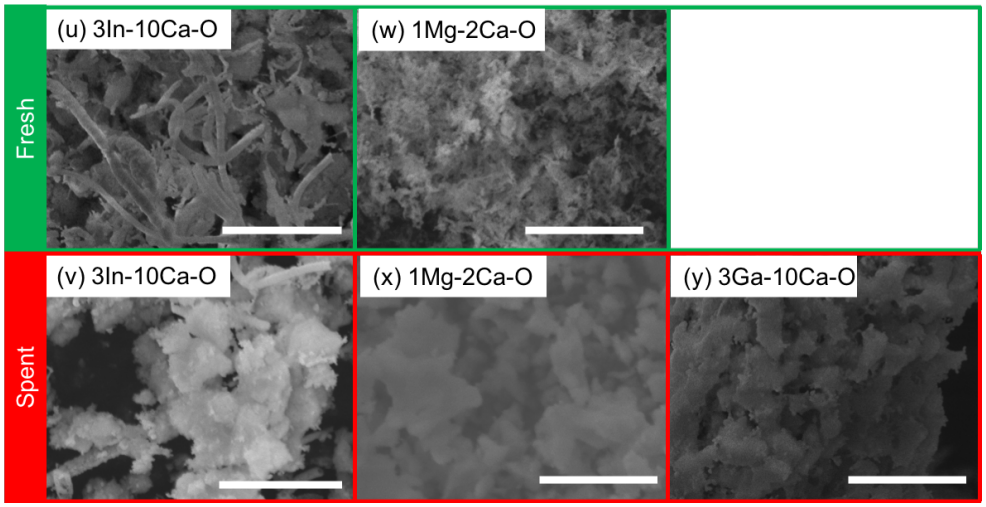

Figure 13. SEM Images of each of the CaO based nanofibers before and after cycling: a, b: CaO; c, d: 3Zn-10Ca-O; e, f: 3Cr-10Ca-O; g, h: 3Li-10Ca-O; i, j: 3Co-10Ca-O; k, l: 1Al-20Ca-O; m, n: 3Y-10Ca-O; o, p: 3Er-10Ca-O; q, r: 3Nd-10Ca-O; s, t: 3La-10Ca-O; u, v: 3In-10Ca-O; w, x: 1Mg-2Ca-O; y: 3Ga-10Ca-O.

Table 6. Calcium/metal ratio, calcium oxide crystallite size, and additive oxide crystallite size for CaO-based sorbents. (a) Obtained by EDS or ICP-OES if denoted with an asterisk after the value. (b) Calculated using the Scherrer equation and the peaks associated with CaO (2θ=37°) and the metal oxide (**Table 9** in the appendix).

Sorbent	Ca/M[(a)]	Crystallite Size[(b)] (nm)		Post Cycled Crystallite Size[(b)] (nm)	
		CaO	Additive	CaO	Additive
CaO	n/a	39	n/a	64	n/a
1Mg-2Ca-O	2.12	27	29	54	83
3Mg-10Ca-O	3.11	28	49	-	-
3Al-10Ca-O	3.52	53	60	50	70
3Y-10Ca-O	3.62*	35	54	51	55
3La-10Ca-O	3.36	48	54	50	84
3Zn-10Ca-O	3.60	28	86	62	88
3Er-10Ca-O	3.72*	48	92	69	117
3Ga-10Ca-O	3.43	47	58	46	84
3Li-10Ca-O	-	59	100	77	156
3Nd-10Ca-O	3.70*	64	54	59	69
3In-10Ca-O	4.01*	54	81	59	87
3Co-10Ca-O	3.09	58	173	55	170
3Cr-10Ca-O	3.28*	58	52	57	137

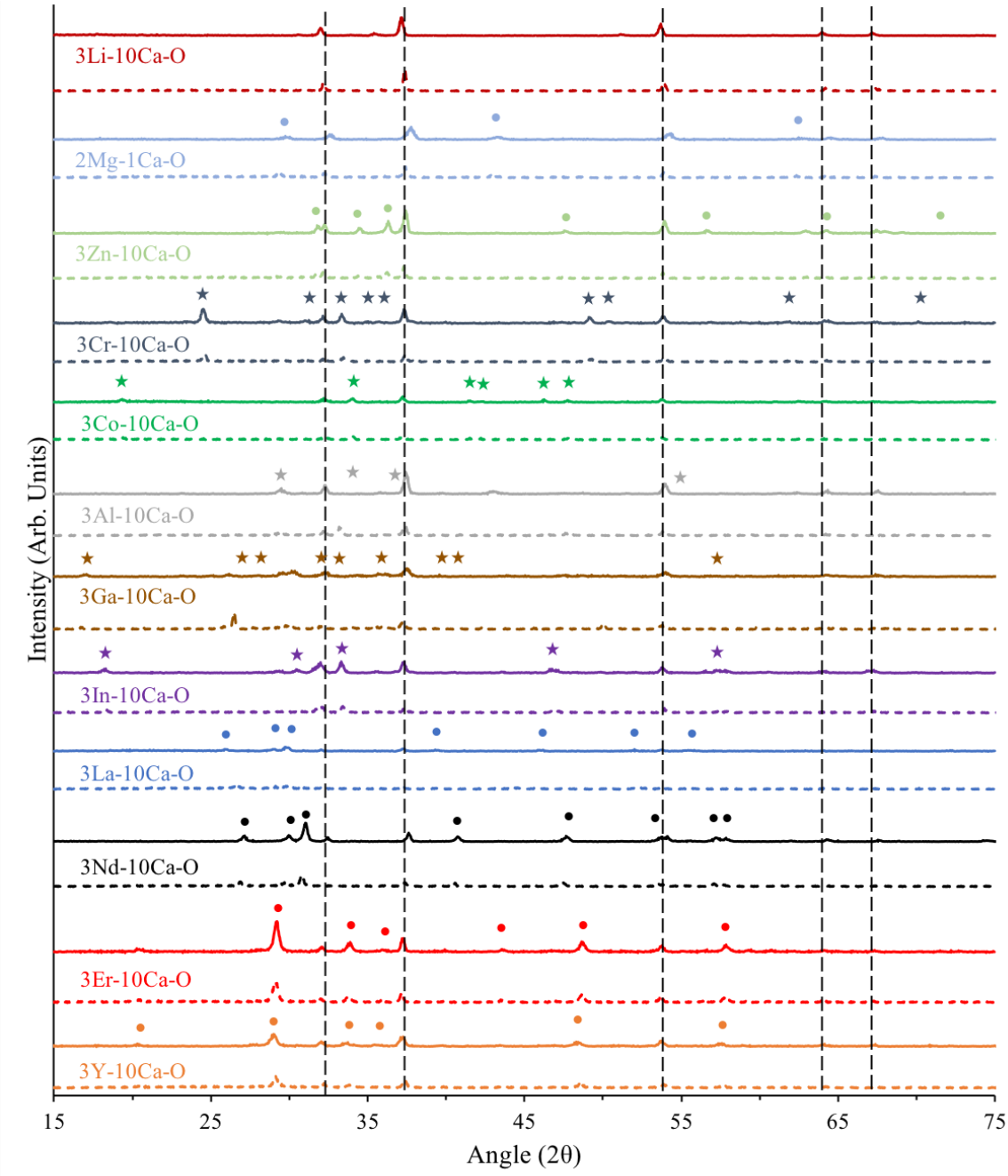

Figure 14. Powder X-ray diffraction scans of calcium oxide-based nanofiber samples. One samples for each additive is included: (top to bottom) Li, Mg, Zn, Cr, Co, Al, Ga, In, La, Nd. Er, and Y. Pre-cycle scans are indicated by the solid spectrum lines and the post-cycle scans are indicated by dashed spectrum lines. Vertical dashed lines denote the peaks of CaO (PDF#48-1467). Circles indicate XRD peaks of additive oxides (M_xO_y) while stars indicate mixed oxides ($Ca_xM_yO_z$) or additive incorporation in to an anion (CrO_4^{2-})

4.3 – Sorption Capacity

The sorption capacity of pure CaO is equal to the stoichiometric capacity of CaO, 0.79 g_{CO2} g_{CaO}^{-1}.[79] Electrospun calcium oxide sorbents with metal additives (3:10 metal additive to calcium oxide) were found to have a broad range of sorption capacities ranging from 0.04 to 0.60 g_{CO2} $g_{sorbent}^{-1}$, as seen in **Figure 15a**, for 1^+, 2^+, and 6^+ oxidation state metal additives, and **Figure 15b**, for 3^+ oxidation state additives (mass gain/loss plots for each TGA experiment are shown in **Figure 35**). The maximum capacity, defined as the highest capacity observed throughout the carbonation-regeneration cycling, is compared to the theoretical capacity and corrected theoretical capacities (for samples where the presence of mixed oxides were confirmed) in **Figure 16**.

The capacity of CaO-based sorbents is influenced by additive metals in various ways. First, the additive metal dilutes the CaO on a per gram basis, as discussed above. Second, calcium can be consumed in the form of a mixed oxide or by an additive metal anion, as shown by XRD and also mentioned above. The mixed oxide not only dilutes CaO, but it consumes calcium that would have been available for carbonation, thus, further decreasing the theoretical capacity. Indeed, this is the case for chromium, aluminum, cobalt, gallium, and indium which form mixed oxides ($CaCrO_4$, $Ca_{12}Al_{14}O_{33}$, $Ca_3Co_2O_6$, $Ca_5Ga_6O_{14}$, and $CaIn_2O_4$, respectively) in a physical mixture with CaO as observed in the XRD patterns (**Figure 14**). The observed decrease in corrected theoretical capacity compared to the theoretical capacity based on complete calcium carbonation is shown in **Figure 16**. Third, the additive metal negatively affects the morphological properties imparted by electrospinning (i.e., presence of macropores and small crystallites), as shown in **Figure 13c** (3Zn-10Ca-O), **13e** (3Cr-10Ca-O), **13g** (3Li-10Ca-O), and **13i** (3Co-10Ca-O) and as discussed above. Lastly, the ratio of additive metal to calcium can be

adjusted to increase (or decrease) the sorption capacity by changing the mass fraction of calcium oxide in the sample, resulting in a tradeoff between theoretical capacity and stability. This is the case for the Al containing samples, three M:Ca ratios were rested 3:10, 1:10, and 1:20 that had sorption capacities of 0.36, 0.62, and 0.75 g_{CO2} $g_{sorbent}^{-1}$, respectively and first order deactivation constants of $3.0x10^{-3}$, $4.7x10^{-3}$, $5.6x10^{-3}$ $cycle^{-1}$, respectively.[79]

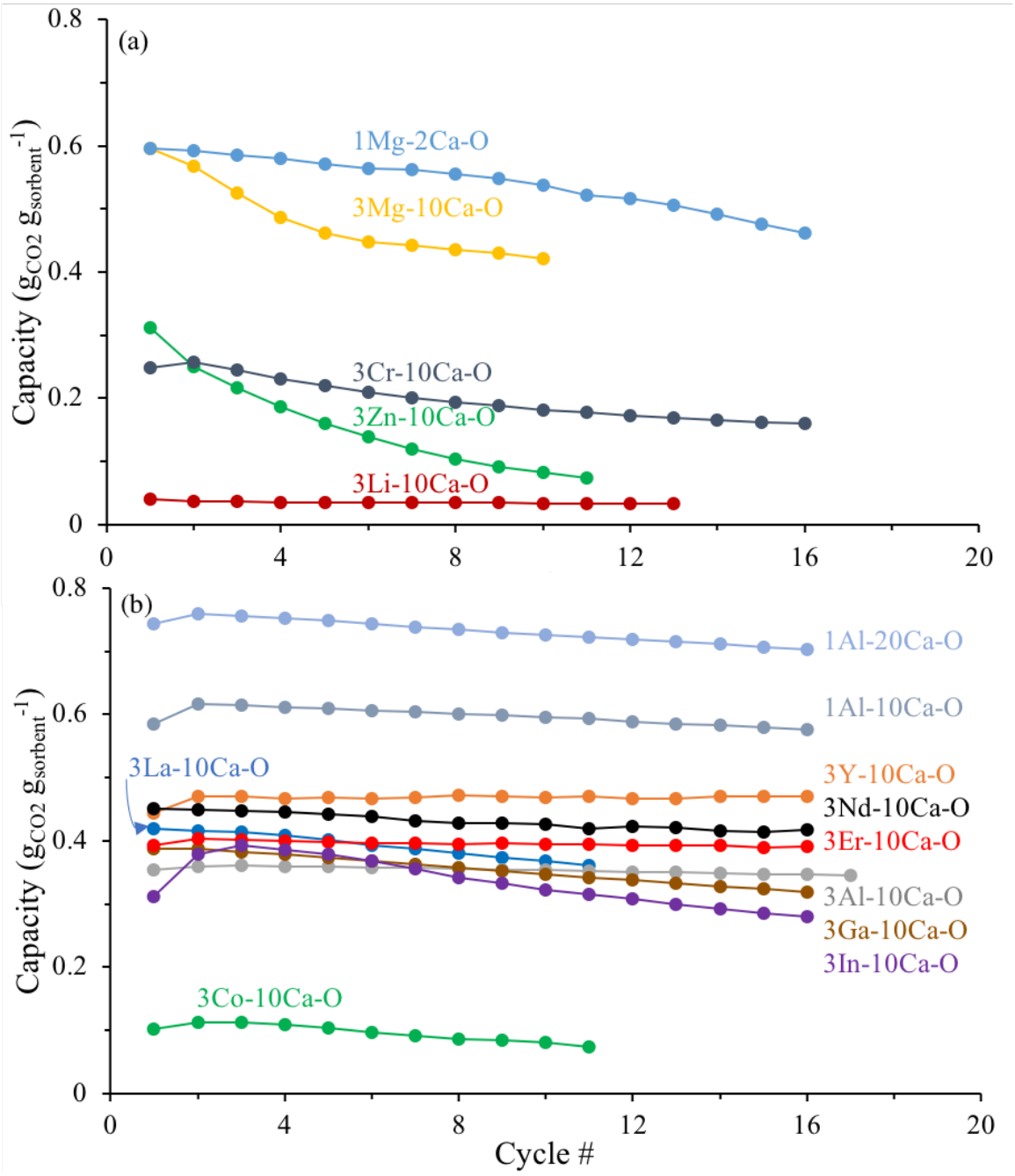

Figure 15. Sorption capacity of calcium oxide-based nanofiber samples across multiple carbonation-regeneration cycles at 873 K, 101 kPa, and 200 sccm of CO_2 via TGA. (a) includes samples with 1^+ (Li), 2^+ (Mg, Zn), and 6^+ (Cr) oxidation state additives. (b) includes samples with 3^+ oxidation state (Al, Co, Er, Ga, In, Nd, and Y) additives.

The property of the additive that had the strongest apparent effect on the sorption capacity of the modified sorbents was the Tammann temperature of the additive metal oxide. The effect can be seen, first, by comparing the SEMs of fresh samples that have high and low temperature additive metals in **Figure 13**. Fresh 3Zn-10Ca-O, 3Li-10Ca-O, and 3Co-10Ca-O can be seen in **Figure 13c, g** and **i**, respectively. The Tammann temperature of Li_2O, ZnO, and Co_3O_4 are 856, 983, and 1052 K, respectively. Since these Tammann temperatures are lower than the thermal treatment temperature during synthesis and regeneration (1173 K), lithium, zinc, and cobalt resulted in the formation of modified sorbents with larger particle sizes compared to fresh CaO. Furthermore, the structure and porosity of these sorbents further degraded due to sintering during regeneration (as observed in **Figure 13d, h** and **j**). Similar degeneration in the physical structure was also observed for 3Cr-10Ca-O comparing **Figure 13e** and **f**, but the cause of this samples instability is likely the presence of the chromate ion which will be discussed below. On the other hand, the SEM images for fresh 3Y-10Ca-O, 3Er-10Ca-O, and 3Nd-10Ca-O, shown in **Figure 13m**, **o**, and **q**, demonstrate that the physical appearance of these sorbents is much more similar to CaO following synthesis, (i.e. small particle sizes, highly porous structures, and minimal agglomeration). The metal oxides formed by these additives, Y_2O_3, Er_2O_3, and Nd_2O_3, have Tammann temperatures of 1473, 1308, and 1253 K, respectively, which are higher than the treatment temperatures during synthesis and regeneration. Indeed, our results show that additives with Tammann temperatures lower than the temperatures used during synthesis and regeneration undergo sintering and particle agglomeration that negates the beneficial properties imparted by the electrospinning process.[79]

The negative effect that a low additive metal Tammann temperature has on the measured or observed physical properties of a sorbent certainly carried over to reaction,

manifesting itself in terms of lower CO_2 sorption capacity. Specifically, samples with a higher oxide Tammann temperature tended to have higher CO_2 capacities and higher conversion of the CaO phases as seen in **Figure 17a** and **b**. Samples with additive oxide Tammann temperatures lower than the regeneration temperature, 1173 K, had low CaO conversions. This is clearly demonstrated for 3Li-10Ca-O and 3Zn-10Ca-O, the samples with the lowest additive oxide Tammann temperatures 856 and 983 K for Li_2O and ZnO, these samples reached 6% and 56% CaO conversion, respectively. The low CaO conversion is due to the high degree of sintering and agglomeration that occurred during synthesis. CaO conversion approached 100% for 3Y-10Ca-O, 3Er-10Ca-O, 3Nd-10Ca-O, 3La-10Ca-O, and 3Mg-10Ca-O. As was mentioned above, the morphological properties of 3Y-10Ca-O, 3Er-10Ca-O, and 3Nd-10Ca-O are similar to pure CaO which also reached 100% conversion at the same conditions.

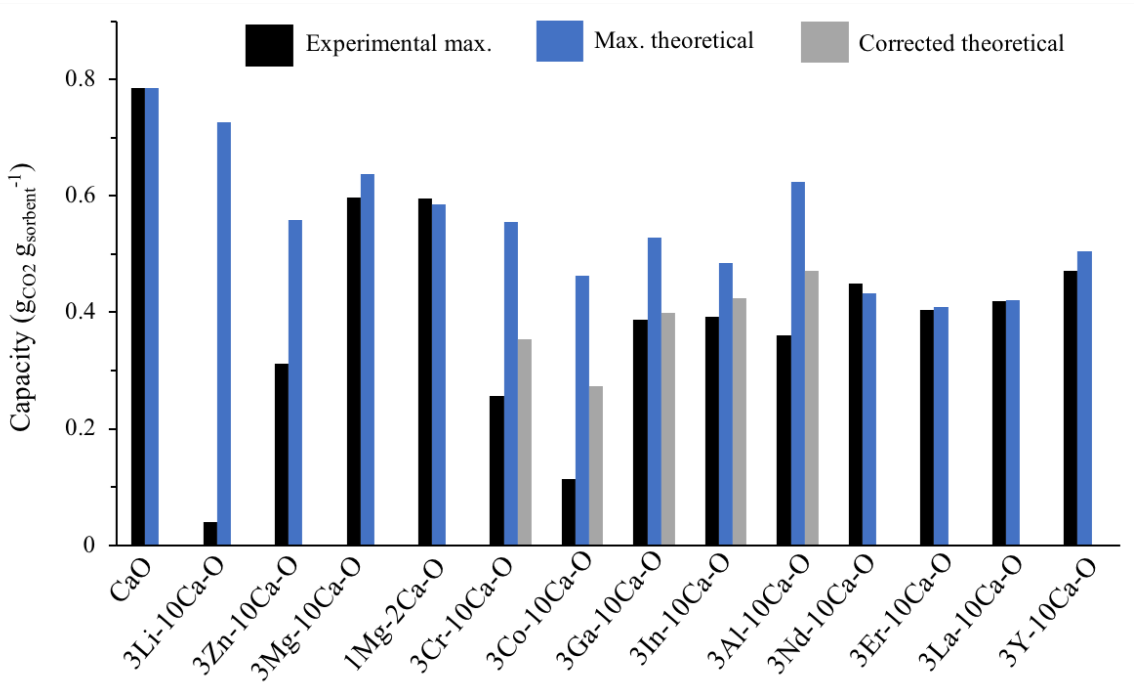

Figure 16. Maximum observed capacity (black bars) compared to theoretical capacity based on CaO content (assuming all Ca exists as CaO; blue bars) and theoretical capacity correcting for Ca incorporation in to mixed oxides (gray bars).

The CaO conversion in the 3Al-10Ca-O sample can give further clarification on the identity of the aluminum-containing additive oxide. **Figure 17b** shows the conversion of 3Al-10Ca-O versus the Tammann temperature assuming that 100% of aluminum exists either as $Ca_{12}Al_{14}O_{33}$ or Al_2O_3. This results in two different Tammann temperatures, 844 and 1263 K for $Ca_{12}Al_{14}O_{33}$ or Al_2O_3, respectively, and two different conversions because the theoretical stochiometric capacity is different for either case. Stoichiometric capacity assuming 100% Al_2O_3 is the maximum theoretical capacity, 0.62 g_{CO2} $g_{sorbent}^{-1}$, assuming 100% $Ca_{12}Al_{14}O_{33}$ is the corrected theoretical capacity, 0.47 g_{CO2} $g_{sorbent}^{-1}$, seen in **Figure 16**. For the case assuming aluminum exists entirely as mayenite, the conversion of CaO is significantly higher than expected, 79%, given its low Tammann temperature of 844 K. Assuming aluminum exists entirely as alumina, the conversion would be 58%, which is

much lower than expected (complete conversion). Discussion in the XRD section commented on the common peak of $Ca_{12}Al_{14}O_{33}$ and $Ca_3Al_2O_6$ at $2\theta=30°$. Prior research on stability of calcium oxide-calcium aluminate mixtures found that samples with $Ca_3Al_2O_6$ have a sorption capacity that increases with the number of regeneration steps, whereas the behavior of our samples, **Figure 15b**, is similar to the behavior of a mayenite-containing sample.[78] Mayenite is certainly present in the sorbent, based on the XRD pattern shown in **Figure 14**, but if all of the aluminum exists as mayenite, the sorption capacity of the sample would likely be much lower than what was observed in **Figure 16** based on its low Tammann temperature 844 K. This observation agrees with morphological observations in **Figure 13k**, where the sample has little agglomeration and appears similar to CaO and other samples with high Tammann temperature additives. These results indicate that, while mayenite formation does consume some of the calcium (thus, reducing the theoretical capacity), some Al also forms Al_2O_3 which is responsible for the higher than expected, for mayenite, CO_2 capacity and stability (as discussed subsequently).

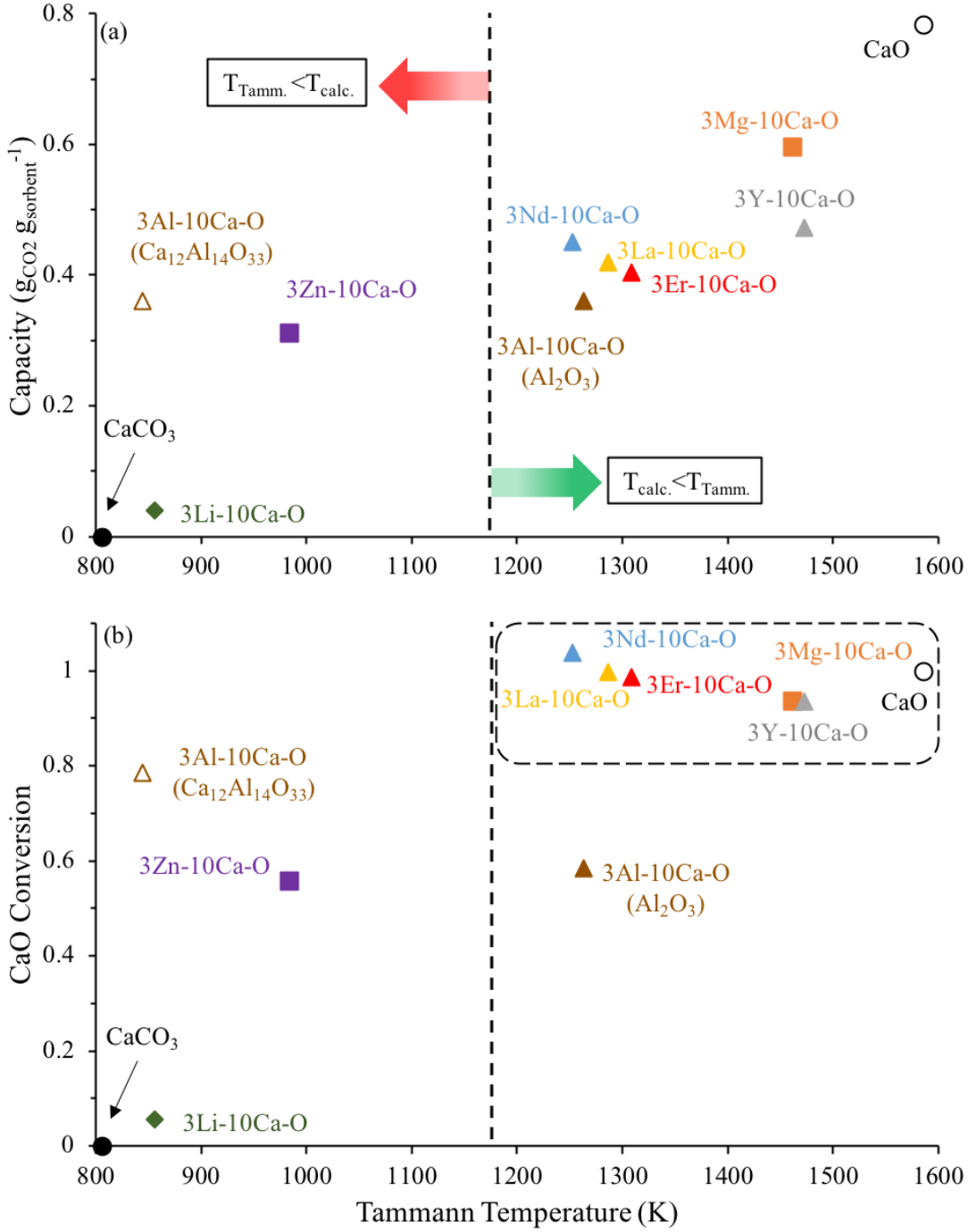

Figure 17. Effect of additive metal oxide on Tammann temperature on (a) the maximum sorption capacity and (b)CaO conversion of the modified sorbents with a 3:10 (M:Ca) ratio. Circles indicate CaO and $CaCO_3$, diamonds indicate 1^+ additives, squares indicate 2^+ additives, triangles indicate 3^+ additives. A hollow triangle is used for the mixed oxide $Ca_{12}Al_{14}O_{33}$ to highlight that the capacity properties observed are a mixture of mixed oxide and alumina. The vertical dashed line indicates the highest temperature that the samples are exposed to, 1173 K.

Samples containing mixed oxides with unknown the Tammann temperature (3Co-10Ca-O, 3Ga-10Ca-O, and 3In-10Ca-O) were not included in **Figure 17**. The capacities of these samples and their proximity to stoichiometric capacity are shown in **Figure 16**. The maximum observed capacity for 3Co-10Ca-O, 3Ga-10Ca-O, and 3In-10Ca-O was 0.11, 0.39, and 0.39 g_{CO2} $g_{sorbent}^{-1}$, respectively; compared to corrected theoretical capacities of 0.27, 0.40, 0.42 g_{CO2} $g_{sorbent}^{-1}$, respectively. Samples containing gallium and indium reached approximately 100% conversion compared to 37% for the cobalt containing sample, assuming stoichiometric mixed oxide formation. Although the Tammann temperature of the mixed oxide species are unknown, the Tammann temperature of CoO, Ga_2O_3, and In_2O_3 are 1052, 1087, and 1092 K, respectively. The high conversion of 3Ga-10Ca-O and 3In-10Ca-O demonstrate that Tammann temperatures of the mixed oxide are likely similar to that of the M_2O_3 oxide form. The high conversion also indicates that if the Tammann temperature of the additive oxide is slightly lower than maximum treatment temperature, high CaO conversion is still possible in the initial carbonation cycles. The Tammann temperature cited for cobalt was CoO, because it can be used as an upper limit of the additive oxide Tammann temperature. This is because the mixed oxide identified via XRD for 3Co-10Ca-O is $Ca_3Co_2O_6$ which implies a Co^{3+} oxidation state. The Tammann temperature of $Ca_3Co_2O_6$ and Co_2O_3 is unknown, but the melting point of Co_2O_3 is 1168 K, which indicates a Tammann temperature around 580-870 K (~50-75% melting point). Thus, the conversion and stability implied by the 1052 K Tammann temperature of CoO can be viewed as the upper limit of expected behavior for 3Co-10Ca-O. The low conversion, 37%, and stability, discussed below, indicate that the Tammann temperature of $Ca_3Co_2O_6$ is likely closer to that of Co_2O_3 than CoO. The last sample not included in this figure was 3Cr-10Ca-O, this

sample had moderate conversion 72% and a high Tammann temperature of 1490 K for $CaCrO_4$. As mentioned previously, 3Cr-10Ca-O had significant agglomeration compared to other samples containing an additive oxide with a high Tammann temperature. Chromium oxide has a Tammann temperature of 1354 K, therefore it is unlikely that chromium would have contributed to sintering if it were formed prior to the chromate ion during synthesis. It is possible these negative properties are due to the formation of the chromate ion itself. A study on the co-precipitation of chromate and calcite ($CaCO_3$), observed chromate ions incorporating preferentially on surface sites of the calcite surface.[80] The affinity of $CaCrO_4$ for the surface of $CaCO_3$ may explain why the conversion of 3Cr-10Ca-O is lower than expected based off of Tammann temperature. If $CaCrO_4$ localizes at the surface of the reacting particles of CaO, $CaCO_3$, and$CaCrO_4$ the surface will become nonreactive and carbonation will need to proceed via diffusion-controlled reaction. This behavior was observed in the RPM model analysis discussed below.

The effect of molecular weight of the additive metal can be observed in **Figure 16** and **Figure 17**. In **Figure 16**, the blue bars indicate theoretical capacity, samples with higher theoretical capacities had lower additive oxide molecular weights. This behavior can be more clearly seen in **Figure 17a**, when looking at samples that had ~100% CaO conversion: 3Mg-10Ca-O, 3Y-10Ca-O, 3Nd-10Ca-O, 3La-10Ca-O, and 3Er-10Ca-O. The samples with the two highest sorption capacities were 3Mg-10Ca-O, 0.60 $g_{CO2}\ g_{sorbent}^{-1}$ and 3Y-10Ca-O, 0.47 $g_{CO2}\ g_{sorbent}^{-1}$. These two samples had the lowest and second lowest additive oxide molecular weight, respectively. Differences between the capacity of 3Nd-10Ca-O, 3La-10Ca-O, and 3Er-10Ca-O (0.45, 0.42, and 0.40 $g_{CO2}\ g_{sorbent}^{-1}$, respectively) are also based off the additive oxide molecular weight, with the heaviest being Er_2O_3,

which had the lowest capacity. The discrepancy between 3Nd-10Ca-O and 3La-10Ca-O is due to the slight differences in the Ca/M ratio in the synthesized materials, where 3Nd-10Ca-O had a Ca/M ratio of 3.70 and 3La-10Ca-O had a ratio of 3.36 (**Table 6**).

The kinetic rate constant, k_{RPM}, and diffusivity constant, D_{RPM}, of a select group of modified sorbents were estimated using the RPM and can be seen in **Figure 18**. The kinetic rate constant characterizes the kinetic-controlled reaction regime and is normalized by surface area and reflects the rate of reaction at the sorbent surface. Whereas the diffusivity constant characterizes the diffusion-controlled reaction regime, where the surface is largely carbonated, or unreactive with CO_2, and it accounts for product layer thickness and permeability. A comparison of the first carbonation conversion data and model fits are included in the appendix **Figure 36.** Sorbents with lower capacities, 3Li-10Ca-O, 3Co-10Ca-O, 3Zn-10Ca-O, and 3Cr-10Ca-O had k_{RPM} of, $4.8x10^{-5}$, $3.5x10^{-5}$, $2.1x10^{-4}$, and $1.4x10^{-4}$ cm^4 mol^{-1} s^{-1}, respectively, and D_{RPM} of, $7.8x10^{-15}$, $4.8x10^{-14}$, $7.1x10^{-13}$, and $4.1x10^{-13}$ cm^2 s^{-1}, respectively. Sorbents with higher capacities, 3Al-10Ca-O, 3Er-10Ca-O, 3Nd-10Ca-O, and 3Y-10Ca-O had k_{RPM} of, $1.1x10^{-4}$, $2.1x10^{-4}$, $2.3x10^{-4}$, and $2.4x10^{-4}$ cm^4 mol^{-1} s^{-1}, respectively, and D_{RPM} of, $5.1x10^{-13}$, $6.3x10^{-13}$, $7.4x10^{-13}$, and $1.3x10^{-12}$ cm^2 s^{-1}, respectively. Generally, the rate constants were of similar magnitude (differing by a factor of 4 at most), however there was up to two orders of magnitude difference in D_{RPM}. These results are similar to our previous paper where differences in k_{RPM} were less than an order of magnitude, whereas D_{RPM} could vary over two orders of magnitude when comparing the best and worst samples.[79] The similarity in k_{RPM} implies the surface reaction of CaO and CO_2 is similar for all samples, except for potential negative interactions between Li and Co additives and the CaO surface. The much smaller diffusivity constants for 3Li-10Ca-O and 3Co-10Ca-O are

likely due to the large particle size and low porosity observed in the SEMs. The primary factor differentiating under-performing 3Zn-10Ca-O and 3Cr-10Ca-O from 3Al-10Ca-O, 3Er-10Ca-O, 3Nd-10Ca-O, and 3Y-10Ca-O was the duration of time for the kinetic regime. For instance, the kinetic regimes of 3Zn-10Ca-O and 3Cr-10Ca-O lasted 0.63 and 0.68 minutes, respectively, compared to 5.2, 3.3, 4.4, and 2.4 minutes for 3Al-10Ca-O, 3Er-10Ca-O, 3Nd-10Ca-O, and 3Y-10Ca-O, respectively. The difference in the kinetic regime durations and how it directly translates to higher conversion can be seen graphically in **Figure 36**. Possible causes of the shorter kinetic regime are either lower CaO surface area, less reactive CaO surface as the carbonation progresses, or possible pore clogging of the sample. This agrees with our observations from SEM, the samples that underperformed had larger particles that were more agglomerated and had lower porosity compared to samples with better performance. The possibility for a less exposed or less reactive CaO surface for the 3Cr-10Ca-O sample surface would agree our prior discussion of literature with regard to the chromate ion having a high affinity for specific surface sites of calcite.[49]

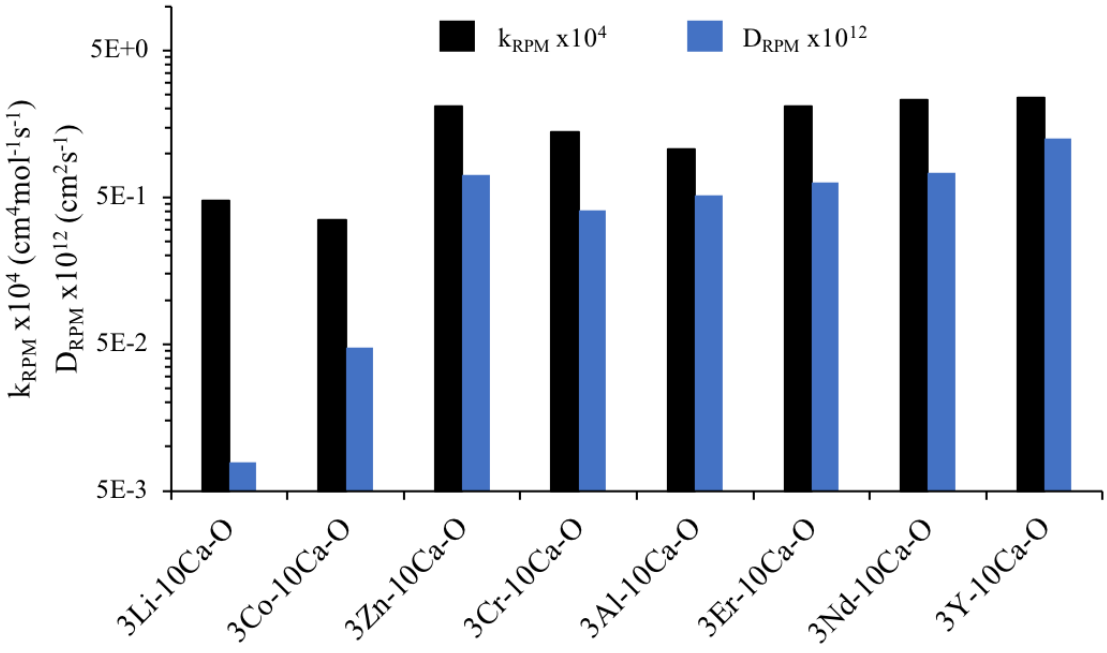

Figure 18. Random pore model kinetic rate constant (black bars) and diffusivity constant (white bars) for the first cycle carbonation of 3Li-10CaO, 3Co-10CaO, 3Zn-10CaO, 3Cr-10CaO, 3Al-10CaO, 3Er-10CaO, 3Nd-10CaO, and 3Y-10CaO.

Based on the results in this section, the preparation of a modified CaO sorbent with a high sorption capacity requires the use of an additive metal that: (1) has high metal oxide Tammann temperature which prevents agglomeration and destruction of the microporous fibrous network during high temperature treatment/regeneration, (2) forms separate metal oxide phases rather than consuming calcium oxide in mixed oxide phases, and (3) has a low metal oxide molar mass. It is also advantageous to reduce the quantity of the additive metal in the sorbent because it increases composition of CaO and thus increases the capacity.[79]

4.4 – Sorption Stability

The stability of modified CaO can be seen graphically in **Figure 15a** and **b** by observing the trend in sorption capacity versus carbonation cycle. Most of the additives metals had either no effect or a slight positive effect on the stability of CaO, quantified by comparing their first order deactivation constants in **Figure 19**. The only metal that had a deleterious effect on the sorption stability was 3Zn-10Ca-O, which had a first order deactivation constant of 0.15 $cycle^{-1}$ compared to 0.042 $cycle^{-1}$ for CaO. No improvement to sample stability was observed for 3Co-10Ca-O, 3Mg-10Ca-O, and 3Cr-10Ca-O which had first order deactivation constants of 0.051, 0.046, and 0.039 $cycle^{-1}$, respectively. First order deactivation constants for 3Ga-10Ca-O, 3In-10Ca-O, 3La-10Ca-O, 1Mg-2Ca-O, and 3Li-10Ca-O were 0.014, 0.027, 0.014, 0.014, and 0.019 $cycle^{-1}$, respectively, approximately 2-4 fold increase in sorbent stability compared to CaO. Improvement in the deactivation constant of an order of magnitude or more, included 3Al-10Ca-O, 1Al-10Ca-O, 1Al-20Ca-O, 3Y-10Ca-O, 3Nd-10Ca-O, and 3Er-10Ca-O which had first order deactivation constants of $3.0x10^{-3}$, $4.7x10^{-3}$, $5.6x10^{-3}$, $4.0x10^{-4}$, $6.0x10^{-3}$, and $3.0x10^{-3}$ $cycle^{-1}$, respectively. In this work, it was found that key additive metal properties that play a role in improving stability included: ability to retain initial fiber properties, Tammann temperature, oxidation state, likelihood of forming mixed oxide phases, and metal additive concentration.

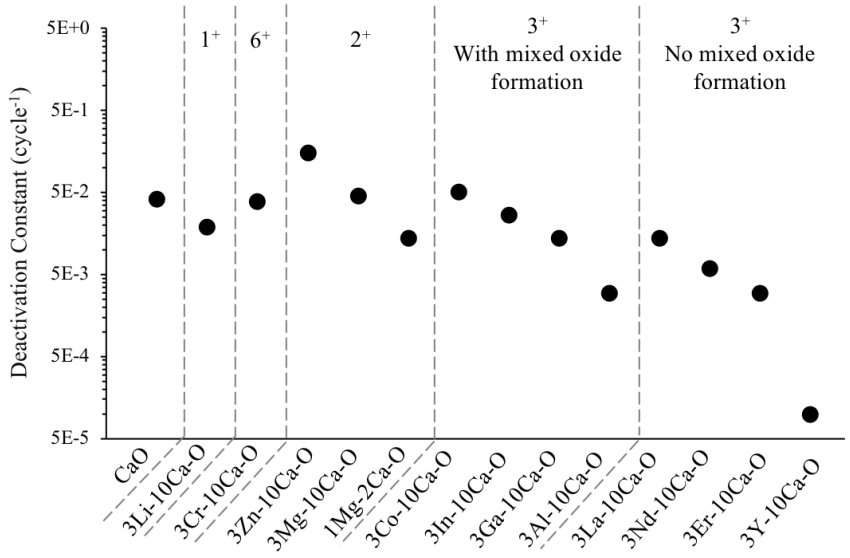

Figure 19. First order deactivation constant of calcium oxide-based samples across multiple carbonation-regeneration cycles. Samples are grouped based on oxidation state of additive metal and formation of mixed oxide.

Evidence of structural changes from pre-carbonation to post cycle are particularly clear for CaO, 3Zn-10Ca-O, 3Cr-10Ca-O, and 3Co-10Ca-O in **Figure 13b, d, f, and j**. Significant structural change is also observed for samples with moderate stability improvement 3Li-10Ca-O, 3La-10Ca-O, 3In-10Ca-O, and 1Mg-2Ca-O, in the remaining SEMs in **Figure 13h, t, v, and x**. The stable samples, 1Al-20Ca-O, 3Y-10Ca-O, 3Er-10Ca-O, and 3Nd-10Ca-O seen in **Figure 13 l, n, p, and r,** all had less post cycle particle growth and less agglomeration than the less stable samples, though there was some loss in the nanofibrous network. The post-cycle XRD spectra, seen in **Figure 14**, show that the oxide forms are returned to their initial state observed in the fresh material for all samples.

Tammann temperature of the additive oxide influences the material properties of fresh sorbents and it also contributes to the maintenance or deterioration these properties

over repeated cycles. **Figure 20** shows the first order deactivation constant as a function of additive oxide Tammann temperature, for additive metals with a 3^+ oxidation state, in an effort to minimize other factors contributing to sorbent stability. There is a clear trend that with increasing Tammann temperature there is a decrease in the first order deactivation constant (i.e. a more stable sorbent). Tammann temperature has an exceptionally strong effect on stability. Specifically, an increase in the Tammann temperature of 20% can increase stability by ca. 1 order of magnitude. **Figure 20** also indicates that samples that form mixed oxides are primarily influenced by the Tammann temperature of the metal oxide, M_2O_3. The Tammann temperature of the pure metal oxides are shown for 3Al-10Ca-O, 3Co-10Ca-O, 3Ga-10Ca-O and 3Ga-10Ca-O and they fit the general trend observed for deactivation constant as a function of additive oxide Tammann Temperature. This further indicates that aluminum is present in some combination of $Ca_{12}Al_{14}O_{33}$ and Al_2O_3, where Al_2O_3 is the species that provides stability over many cycles. **Figure 20** agrees with the behavior of 2^+ oxidation state metals in this study. The Tammann temperature of ZnO and MgO are 983 K and 1461 K, respectively and they have first order deactivation constants of 0.153 and 0.046 $cycle^{-1}$, respectively.

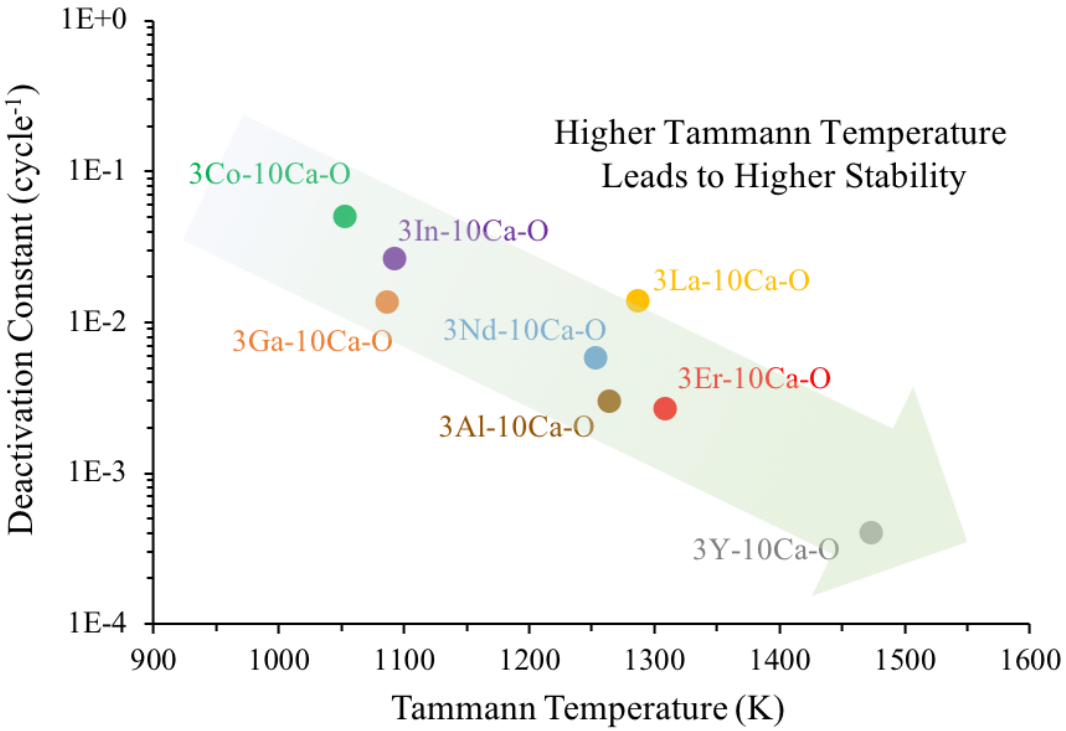

Figure 20. First order deactivation constant of modified CaO with 3:10 (M:Ca) ratio as a function of the additive oxide Tammann temperature for 3^+ oxidation state metals. All Tammann temperatures are associated with unmixed metal oxide (M_2O_3).

Each of the most stable samples in this study (yttrium, neodymium, erbium, aluminum, gallium, and indium) has a 3^+ oxidation state. Four additives did not have a 3^+ oxidation state: lithium, magnesium, zinc, and chromium. Of these samples lithium and zinc oxides have very low Tammann temperatures (856 and 983 K) such that the lithium containing sample had a completely destroyed structure and less than 10% CaO conversion. Similar poor performance, albeit less dramatic was observed for 3Zn-10Ca-O. Despite $CaCrO_4$, chromate is expected to localize around calcite surfaces, thus inhibiting carbonation and leading to accumulation of CaO surfaces post regeneration. Thus, of the additives that were not 3^+ oxidation state, only magnesium was expected to positively impact the CaO sorbent. Despite having a high Tammann temperature there is a loading

threshold for magnesium to positively influence the sorbent stability. It is unclear what the primary reason for this discrepancy is. A previous study by Lu et al. has found improved stability for additive metals with 4^+ oxidation states, including zirconium, silicon, cerium, and titanium. It should be noted in this study the regeneration conditions were at a more moderate conditions 973 K for 30 minutes, and each of the additive oxides exceeded the regeneration temperature.[36] Improved stability have been observed for additives of 2^+, 3^+, and 4^+ oxidation states therefore unlikely that additive oxidation state has a strong effect on the stability of modified CaO stability.

The crystallite stability of CaO and the additive oxide do not appear to influence the stability of CO_2 sorption. Indeed, most of the unstable sample CaO crystallite sizes nearly double over 10-16 cycles. However, 3Er-10Ca-O, the second most stable in this study, has its crystallite size increase by a factor of 1.4 over 16 cycles. This is likely because the initial CaO crystallite size of all samples is relatively small < 65 nm, with the CaO crystallite of 3Er-10Ca-O being on 69 nm after 16 cycles. Furthermore, the formation of mixed oxides has been cited as a source of stability for aluminum ($Ca_{12}Al_{14}O_{33}$) and zirconium ($CaZrO_3$) in literature.[36,38] In this work, 3Al-10Ca-O, 3Co-10Ca-O, 3Cr-10Ca-O, 3Ga-10Ca-O, and 3In-10Ca-O all formed mixed oxides (or chromates), and these samples had deactivation constants of $3x10^{-3}$, $5.2x10^{-2}$, $3.9x10^{-2}$, $1.4x10^{-2}$, and $2.7x10^{-2}$ $cycle^{-1}$, respectively (**Figure 19**). Only 3Al-10Ca-O had a strong stabilizing effect on the sorption capacity, which indicates that the presence of a mixed oxide is not the primary stabilizing force for these samples. This further indicates that some aluminum is present in the form of Al_2O_3 which provides stability to the sample. These results are still in agreement with previous studies that attributed stability to mixed oxides or $CaZrO_3$. For example, the Tammann temperatures of ZrO_2 and $CaZrO_3$ are

1218[36] and ~1125 K, respectively. Thus, zirconium is a stabilizing additive due to high Tammann temperature, though not necessarily due to the formation of a mixed oxide. While some mixed metal oxides may improve stability, it is not a characteristic trait of all mixed metal oxides.

Chapter 5: Nanofibrous Materials for Sorbent-Enhanced Steam Methane Reforming

Plug flow reactors packed with sorbent or a catalyst-sorbent mixture were used to characterize CO_2 breakthrough curves for calcium oxide carbonation in 5-18% CO_2 inlet concentration and for the SE-SMR reaction. CO_2 breakthrough experiments with a 5-18% CO_2 inlet concentration were used to translate our knowledge from the TGA experiments in Chapters 3 and 4 to a more industrially relevant reaction set up and also to determine how water influences the carbonation of calcium oxide. The CO_2 breakthrough time and maximum capacity, q_0, determined using the Cooper model, increased with increasing CO_2 concentration, steam concentration, and temperature. The presence of water during the carbonation led to a more significant loss in maximum capacity than the dry experiments. This indicates that under SE-SMR conditions sorbent stability likely to be a greater problem than capacity, as the steam present in the reformer will tend to increase sorbent capacity and decrease sorbent stability.

SE-SMR was studied using CaO-marble, CaO-D-acetate, CaO-nanofibers, and 1Al-20Ca-O sorbents at 823 K and a S:C ratio of 3. In the pre-breakthrough period, each of the reactors had 100% selectivity to H_2 and methane conversions greater than the SMR equilibrium. The magnitude of the breakthrough times, normalized by space velocity, for the materials were similar in order to the capacities measured by TGA. The CaO-nanofibers and 1Al-20Ca-O exhibited more than a factor of three longer breakthrough time compared to marble (1650, 6400, and 7500 mL $g_{sorbent}^{-1}$ for CaO-marble, 1Al-20Ca-O-nanofibers, and CaO-nanofibers respectively). The stability of modified sorbents translated well to reforming conditions. CaO-nanofibers and CaO-D-acetate lost ~45% of its initial breakthrough time, while 1Al-20Ca-O retained 94% of its initial breakthrough time over ten reforming-regeneration cycles.

5.1 – CO_2 Breakthrough Experiments

A parameter space of operating conditions that are similar to SE-SMR process conditions were studied for their effect sorbent performance for CaO-marble sorbents. Although CaO-marble is a relatively underperforming sorbent, in the TGA it had similar behavior as other sorbents, namely capacity as a of function temperature and deactivation behavior, in terms of both deactivation constant and observed sintering and agglomeration. The conditions varied include temperature, CO_2 concentration, carbonation-regeneration cycling, and presence, or absence, of steam. The complete set of breakthrough curves can be seen in **Figure 37 and 37**. The CO_2 breakthrough curves were analyzed with the Cooper model LDF to determine the LDF rate constant, k, and maximum capacity, q_0, tabulated in **Table 10**. The breakthrough curves will be discussed in terms of their CO_2 breakthrough time (the x-axis, normalized in terms of g_{CO2} g_{CaO}^{-1}), which is the time where C/C_0 rises above its baseline and also in terms of rate constant and maximum capacity determined using the Cooper model. Although these experiments do not involve the reforming reaction, it is notable that the breakthrough time is more critical to SE-SMR than the maximum capacity. This is because during the time elapsed between these two values CO_2 is present in the outlet, which indicates the process would not be at equilibrium i.e. the conditions where SE-SMR derives its benefits.

The effect of concentration and temperature on CO_2 breakthrough can be seen in **Figure 21** and **Figure 22**. Overall the effect is what would be expected from general knowledge and results from Chapter 3, at higher concentrations and temperatures more CO_2 is absorbed by CaO, shown by the shift right in the curves. It is also important to note that this increase in CO_2 absorbed translates to increased CO_2 breakthrough times as well.

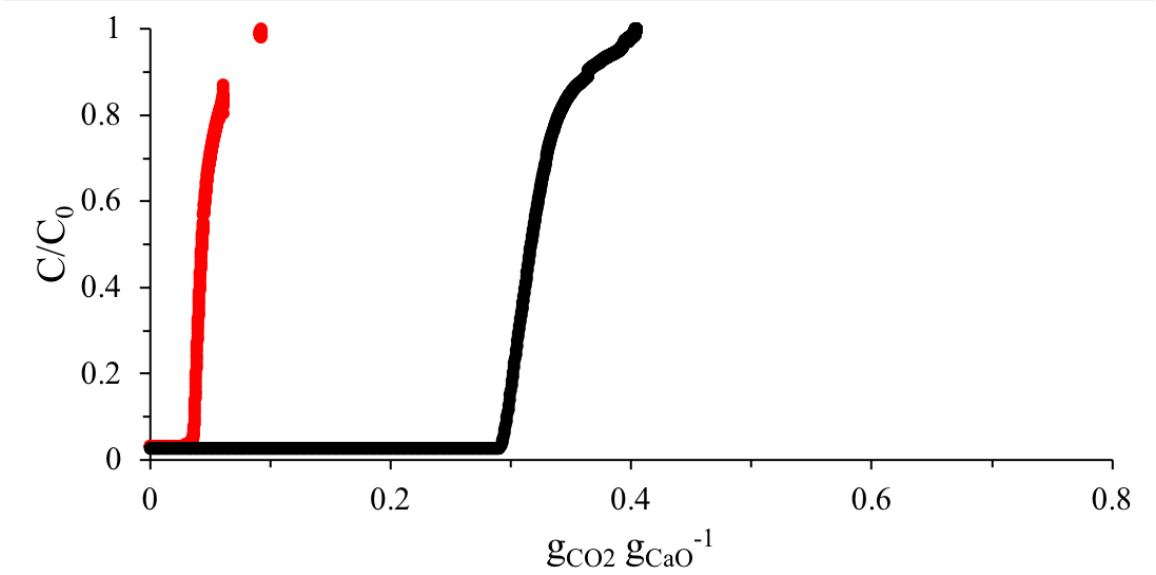

Figure 21. Normalized concentration of effluent gas stream as a function of CaO carbonation, at 823 K. The red and black lines indicate 5% and 18% CO_2, respectively.

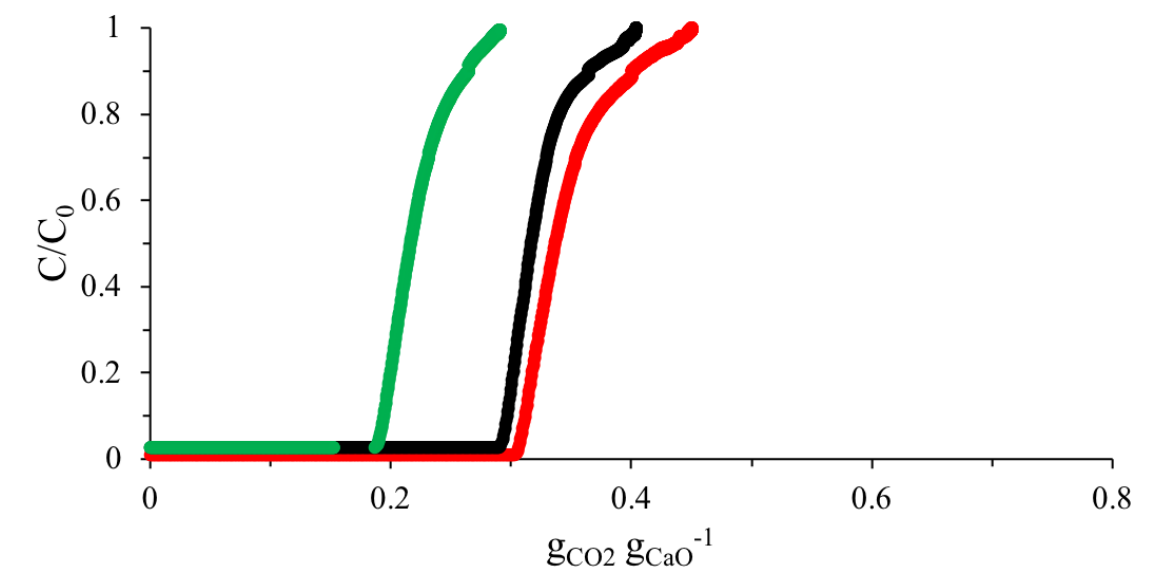

Figure 22. Normalized concentration of effluent gas stream as a function of CaO carbonation. The green, red and black lines indicate 823, 873, and 973 K, respectively.

The concentration of CO_2 in the inlet stream has a dramatic effect on the breakthrough curve and capacity of CaO. **Figure 21** the breakthrough curves at 823 K of CO_2 for 18% CO_2 and 5% CO_2 in the black and red lines, respectively. The primary effect of decreasing the CO_2 concentration is that the breakthrough curve is shifted left, indicating CO_2 breakthrough at lower

conversions of CaO. Ultimately this occurs because the reaction rate kinetics are reduced at lower gas phase concentrations of CO_2, which leads to the characteristic reaction time being larger than the space time of CO_2 in the reactor. Secondly is the curve becoming sharper at lower concentrations, indicating that there is less carbonation of CaO during the breakthrough window. This effect is due to the lower concentration leading to a smaller driving force for the diffusion of CO_2 through $CaCO_3$. The maximum capacity, predicted by the Cooper model, has a linear dependence on the concentration of CO_2 in the range tested as seen in **Figure 23**.

The effect of temperature on the breakthrough curve of 18% CO_2 at 823, 873, and 923 K is seen in **Figure 22**. As temperature is increased the breakthrough curves are shifted further right indicating higher CaO conversion prior to CO_2 breakthrough. This occurs because the reaction and diffusion rates are increased as temperature is increased. **Figure 24** shows the effect of temperature on the maximum capacity, predicted by the Cooper model, in the presence and absence of steam. In the absence of steam, the maximum capacity of CaO increases with increased temperature. In the presence of steam, the maximum capacity is unchanged by temperature. This lack of effect due to temperature is likely due to the nearly theoretical capacity exhibited at the lowest temperature tested. **Figure 25** shows the Arrhenius plot for the rate constant predicted by the Cooper model for dry streams at 18% and 5% CO_2. The general trend is as expected, with higher rates, kK, at higher temperatures, where K is the distribution parameter q_0/C_0. Detailed information on the influence of temperature on the reaction rate constant cannot be determined because k, is a lumped rate constant including the reaction rate constant, pore diffusion, and diffusion through the solid. Each of these terms has a dependence on the temperature of the reactor.

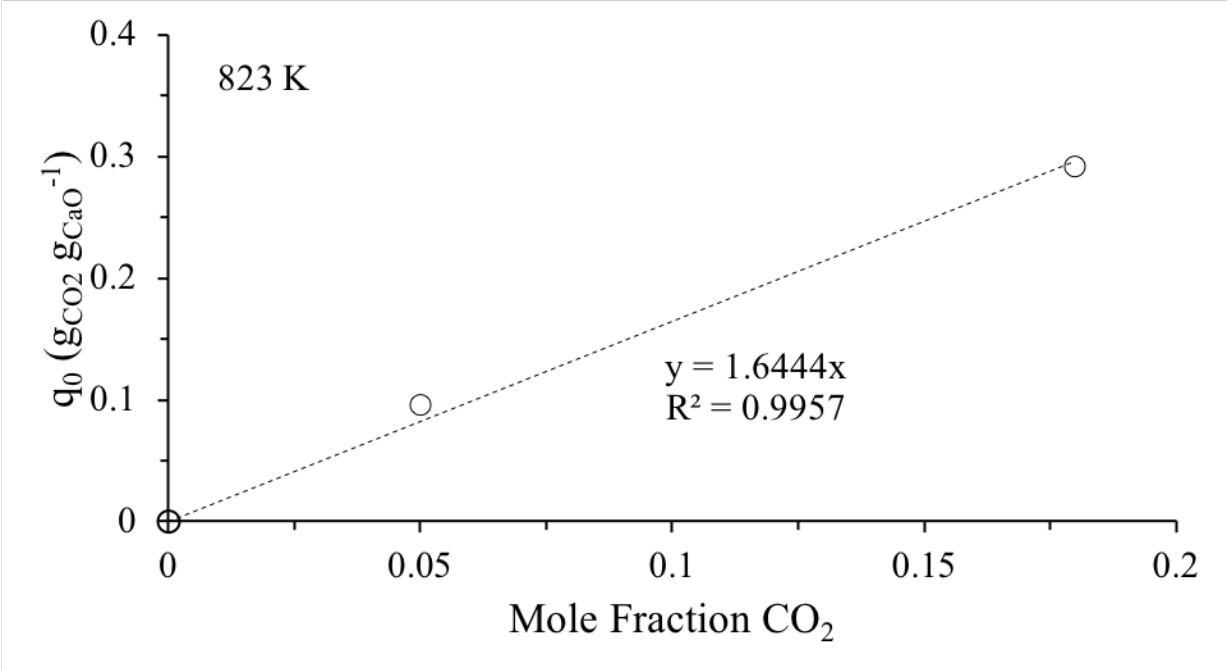

Figure 23. Maximum capacity determined by the Cooper model as a function of inlet mole fraction of CO_2, at 823 K and in the absence of steam.

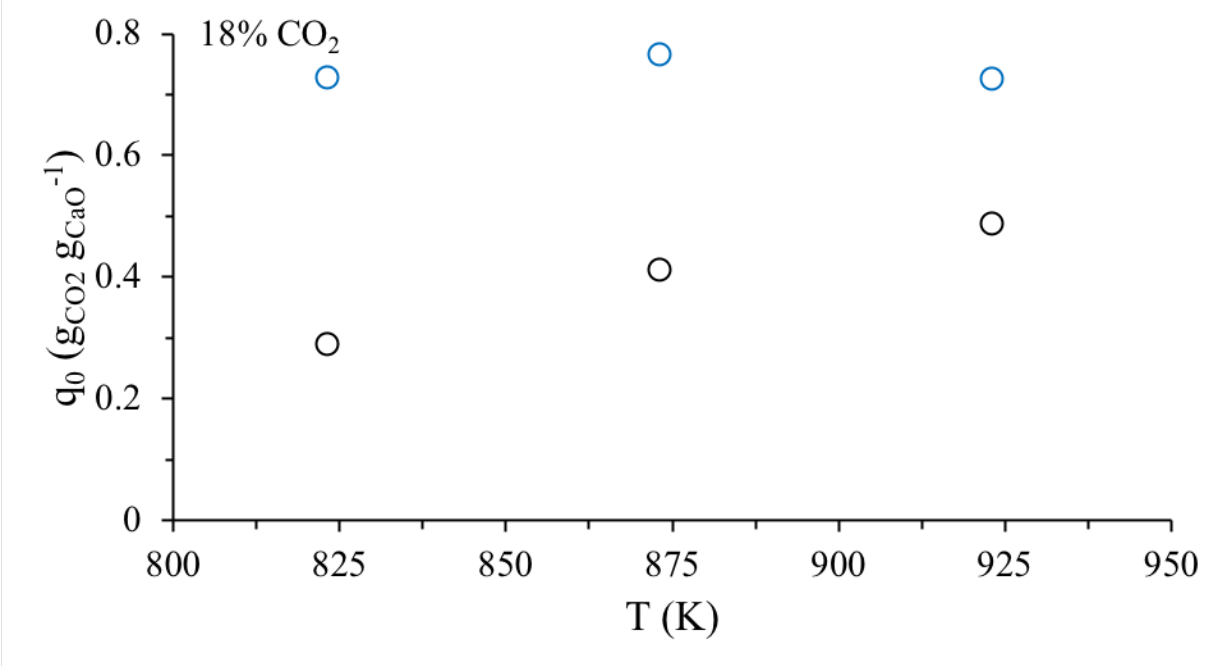

Figure 24. Maximum capacity determined by the Cooper model as a function of temperature in 18% CO_2 (dry mole fraction). Black circles indicate no presence of steam. The blue circles indicate the presence of steam at a ~2.5:1 (Steam:Dry gas flowrate) ratio.

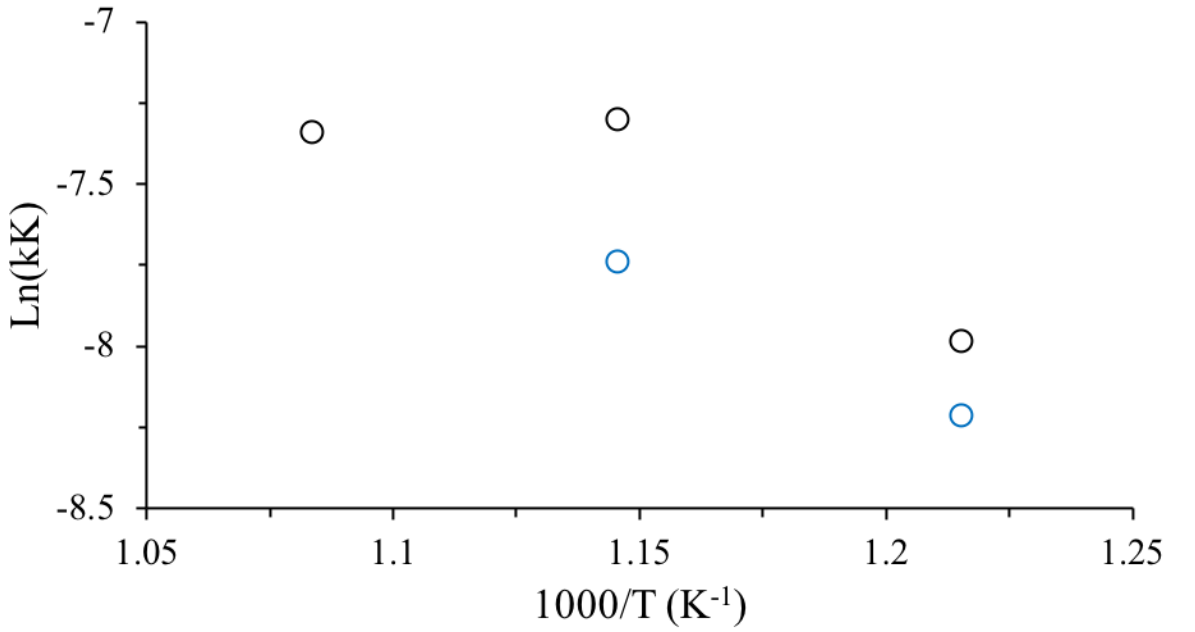

Figure 25. Arrhenius plot of the rate constant determined by the Cooper model fits. Black and blue circles indicate 18% and 5% CO_2 inlet concentration, respectively.

Calcium oxide carbonation in the presence of steam and stability in the presence of steam was not tested using the TGA because of equipment constraints. **Figure 26** is a comparison of the breakthrough curves of 18% CO_2 at 873 K with and without steam. This shows that the presence of steam increases the breakthrough time substantially. Also, in the presence of steam, calcium oxide picked up about twice the CO_2 during the breakthrough period, which indicates that the steam increases the rate of carbonation during diffusion-controlled carbonation.

The CO_2 breakthrough curve undergoes two changes upon its second carbonation cycle. **Figure 27** shows the breakthrough curves of 18% CO_2 for at 873 K for the first and second carbonation. First, the curve for the second carbonation is shifted left, which indicates that the CO_2 breakthrough is occurring at lower conversions of CaO. Second, the breakthrough curve for the second carbonation becomes sharper, this indicates a sharp break between total CO_2 sorption

and no observed CO_2 sorption, chemically what is happening is that the diffusion-controlled carbonation step becomes slower and hence less relevant on the effluent composition.

Similar to the general shape of the breakthrough curves, cycling resulted in two significant changes to the rate constant and maximum capacity, as determined by the Cooper model. First, generally the rate constant increased on the second cycle compared to the first, **Table 10**. This can also be observed graphically in **Figure 37 and 37**, where if the second cycle is compared to the first, generally the curve becomes sharper or more like a step change. This makes sense physically as the curve being sharper indicates less of an effect, or a slower, diffusion-limited reaction regime. This agrees with what was observed in the Chapters 3 and 4 where cycling resulted in sintering and agglomeration which would lead to larger particles and hence slower diffusion. Second, cycling of calcium oxide in the presence of steam resulted in a more significant loss in capacity than cycling without water as seen in **Table 10**. The samples cycled without the presence of steam had roughly constant maximum capacity as determined from the Cooper model, whereas in the presence of steam samples lost approximately 28% of its maximum capacity.

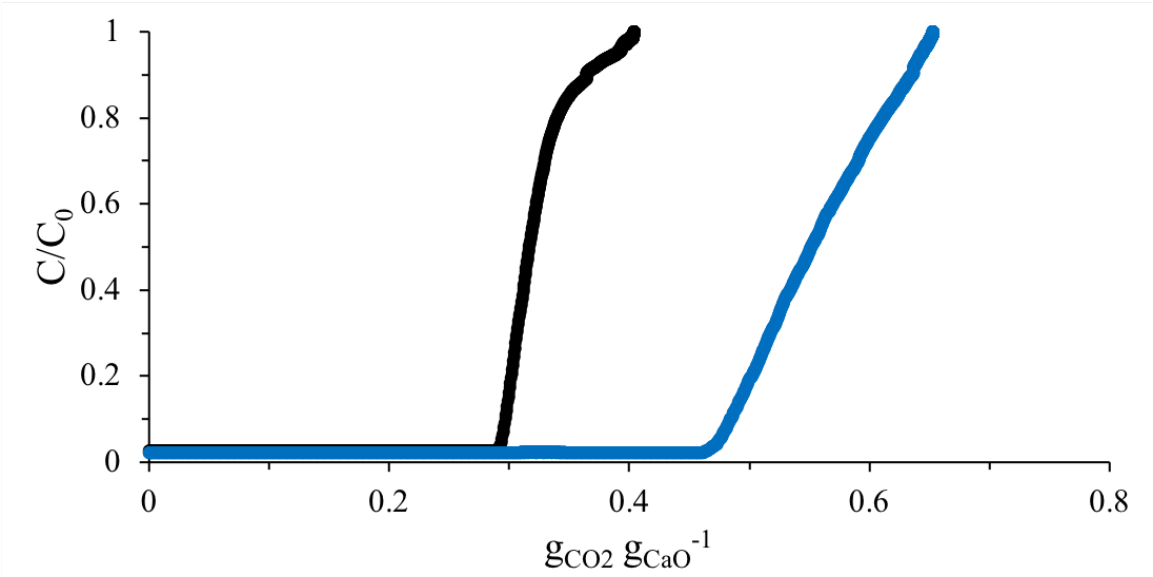

Figure 26. Normalized concentration of the effluent gas stream as a function of CaO carbonation, in 18% CO_2 (dry mole fraction) at 873 K. The black line indicates no presence of steam. The blue line indicates the presence of steam at a ~2.5:1 (Steam:Dry gas flowrate) ratio.

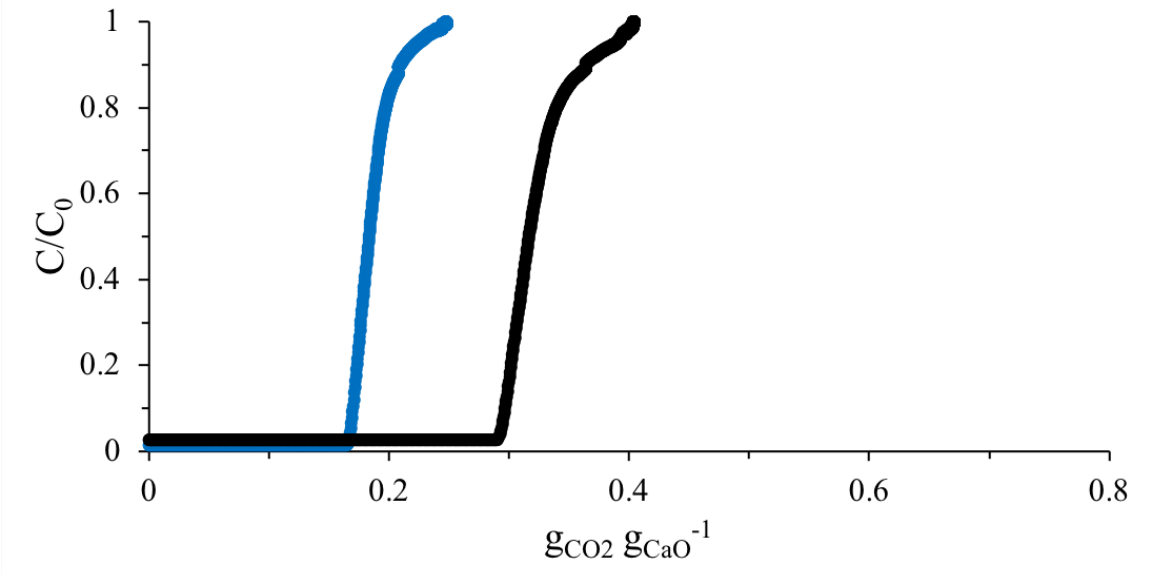

Figure 27. Normalized concentration of effluent gas stream as a function of CaO carbonation, in 18% CO_2 at 873 K. The black and blue lines indicate the first carbonation and second carbonation, respectively.

5.2 – SE-SMR Experiments

1Al-20Ca-O-nanofibers, CaO-nanofibers, CaO-D-acetate, and CaO-marble were tested as sorbents in SE-SMR, and the results are shown in **Figure 28**. SE-SMR was operated under the following reaction conditions: 823 K, 101 kPa total pressure (91 kPa of steam, 28 kPa of methane, and 3 kPa of argon) in a fixed-bed reactor with a HiFUEL R110 commercial NiO-based catalyst and one of the sorbents listed above. Initial methane conversion and H_2 product selectivity (i.e., before complete consumption of the sorbent), defined as moles H_2 per moles total product, and CO_2 breakthrough time (an indicator of sorbent capacity) are shown in **Figure 28a** for the four sorbents tested. Breakthrough time is taken as the data point where the composition of CO_2 equals or exceeds a mole fraction of 0.01. **Figure 28b** shows CO_2 mole fractions in SE-SMR reactor effluents as a function of reaction time on stream (normalized by the space velocity). At early times on stream, undetectable amounts of CO_2 appear in the effluent from the reactor, indicating high rates of sorption (i.e., all CO_2 produced from methane reforming is trapped by the solid CaO). During this stage of the reaction, each reactor (containing 1Al-20Ca-O-nanofibers, CaO-nanofibers, CaO-D-acetate, or CaO-marble) exhibited 100% selectivity to H_2. After breakthrough, the concentration of CO_2 in the effluent (and correspondingly, the selectivity to H_2 and conversion of methane) approached the SMR equilibrium values (red line in **Figure 28b**). The reactors that contained electrospun materials or CaO-D-acetate approached SMR equilibrium at a slower rate than CaO-marble. This behavior reflects the higher effective diffusivities for these materials (as shown in **Table 5** and discussed in detail in Chapter 3), which allow nanofiber materials and CaO-D-acetate to continue to adsorb CO_2 at a higher rate than CaO-marble during diffusion- controlled sorption regimes.

As shown in **Figure 28a**, the reactors loaded with the CaO-D-acetate and electrospun materials had a considerably higher methane conversion (88%, 83%, and 84% for CaO-D-acetate, CaO-nanofibers, and 1Al-20Ca-O-nanofibers, respectively) compared with CaO-marble (71%). Each of these systems can approach the same conversion by increasing or decreasing the loading or length (sorbents and catalysts) inside the reactor so that the reactor will always have a low concentration of CO_2, thereby shifting the SMR reactions toward H_2 products. **Figure 28a** also shows the CO_2 breakthrough time of the three sorbents, which are 1650, 6530, 7500, and 6400 mL gaseous flow g_{CaO}^{-1} for CaO-marble, CaO-D-acetate, CaO-nanofibers, and 1Al-20Ca-O-nanofifibers, respectively. The longer duration of SE-SMR for the electrospun sorbents results primarily from the higher CO_2 capacity of these materials, which is imparted by their smaller CaO crystallite size and larger extent of macroporosity. Their superior performance, as evident in Chapter 3, impacts the entire SE-SMR process by allowing for a factor of three or more decrease in contact time compared with CaO-marble to produce similar quality hydrogen streams under the same operating conditions (i.e., temperature, pressure, feed composition, and time between regeneration). Alternatively, the nanofibers allow for three or more times longer reaction periods (before regeneration) compared with CaO-marble while producing the same hydrogen stream at the same conditions. Finally, the nanofibers allow for the same quality hydrogen stream to be produced compared with CaO-marble but at milder conditions (i.e., lower temperature and pressures and shorter reactor contact time). Operation at milder conditions decreases capital and operational costs for SE-SMR by allowing for the use of less expensive materials for construction.[12]

CaO-D-acetate, CaO-nanofibers, and 1Al-20Ca-O-nanofibers were also tested in cyclic SE-SMR/regeneration experiments under the same conditions described in the previous section. After each SE-SMR run, the sorbent was regenerated by flowing 50 sccm of UHP hydrogen gas at 998 K with a ramping rate of 2 K min^{-1} and held overnight. The results of these experiments are shown in **Figure 29**. After ten cycles of SE-SMR-regeneration, the CO_2 breakthrough time from reactors containing CaO-D-acetate and CaO-nanofibers decreased by 62% (from 6530 to 2490 mL g_{CaO}^{-1}) and 45% (from 7500 to 4125 mL g_{CaO}^{-1}), respectively, whereas the CO_2 breakthrough time from reactors containing 1Al-20Ca-O-nanofibers decreased by 6% (from 6400 to 6000 mL $g_{sorbent}^{-1}$), thus indicating better stability during repeated reforming–regeneration cycles, in agreement with results from TGA studies. The high stability of 1Al-20Ca-O nanofibers in SE-SMR agrees with previous studies using nickel supported on Al-Ca-O mixtures.[81]

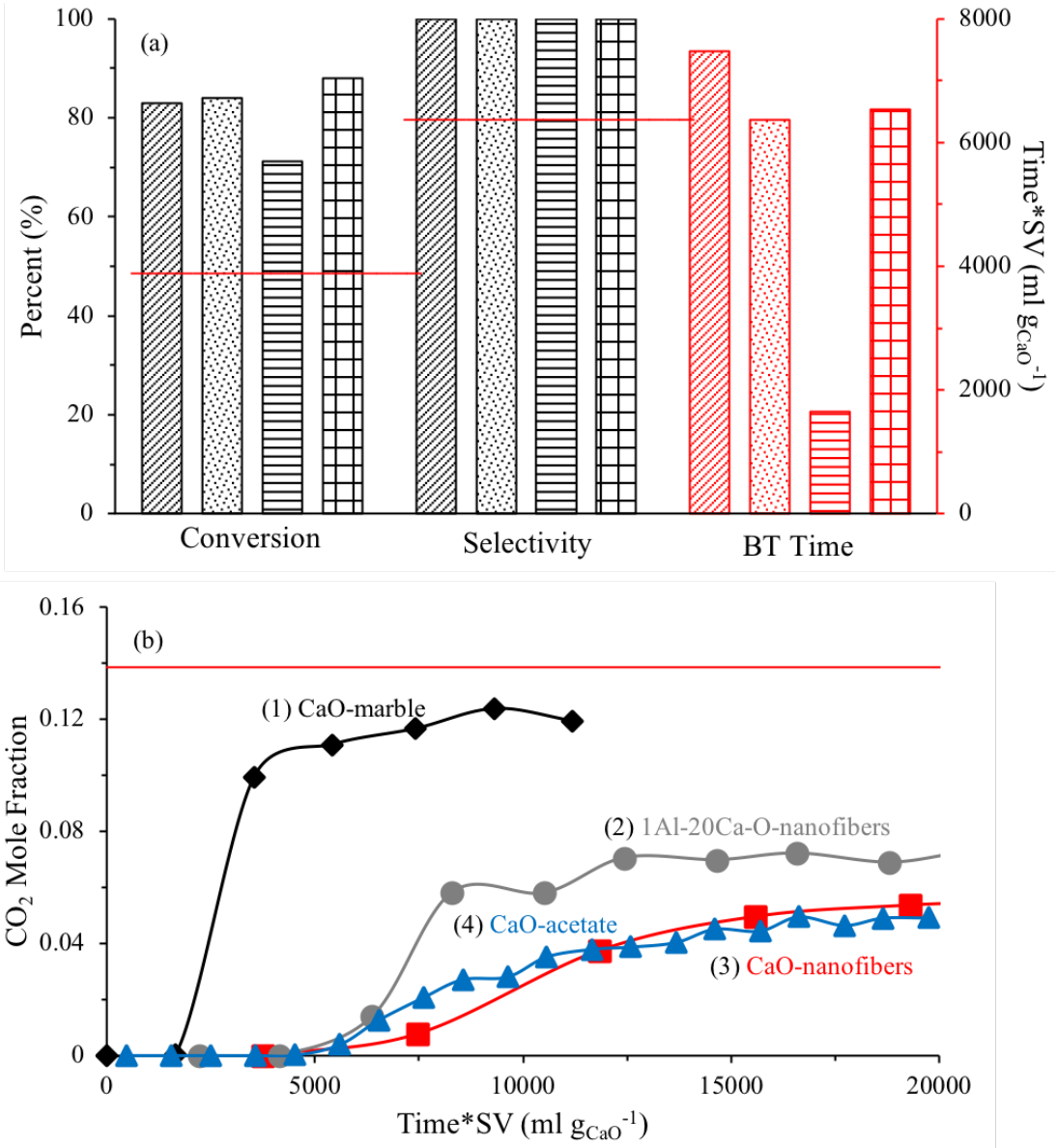

Figure 28. (a) Hydrogen selectivity, conversion, and CO_2 breakthrough time (in red) for SE-SMR process using CaO-marble (horizontal lines) and CaO-nanofiber (Diagonal lines). SMR equilibrium lines (823 K, steam:carbon ratio of 3) for conversion and selectivity are red horizontal lines. (b) CO_2 mole fraction as a function of time (normalized by space velocity) CaO-marble are black diamond symbols CaO-nanofiber are red squares. Equilibrium line (823 K, steam:carbon ratio of 3) is a red horizontal line.

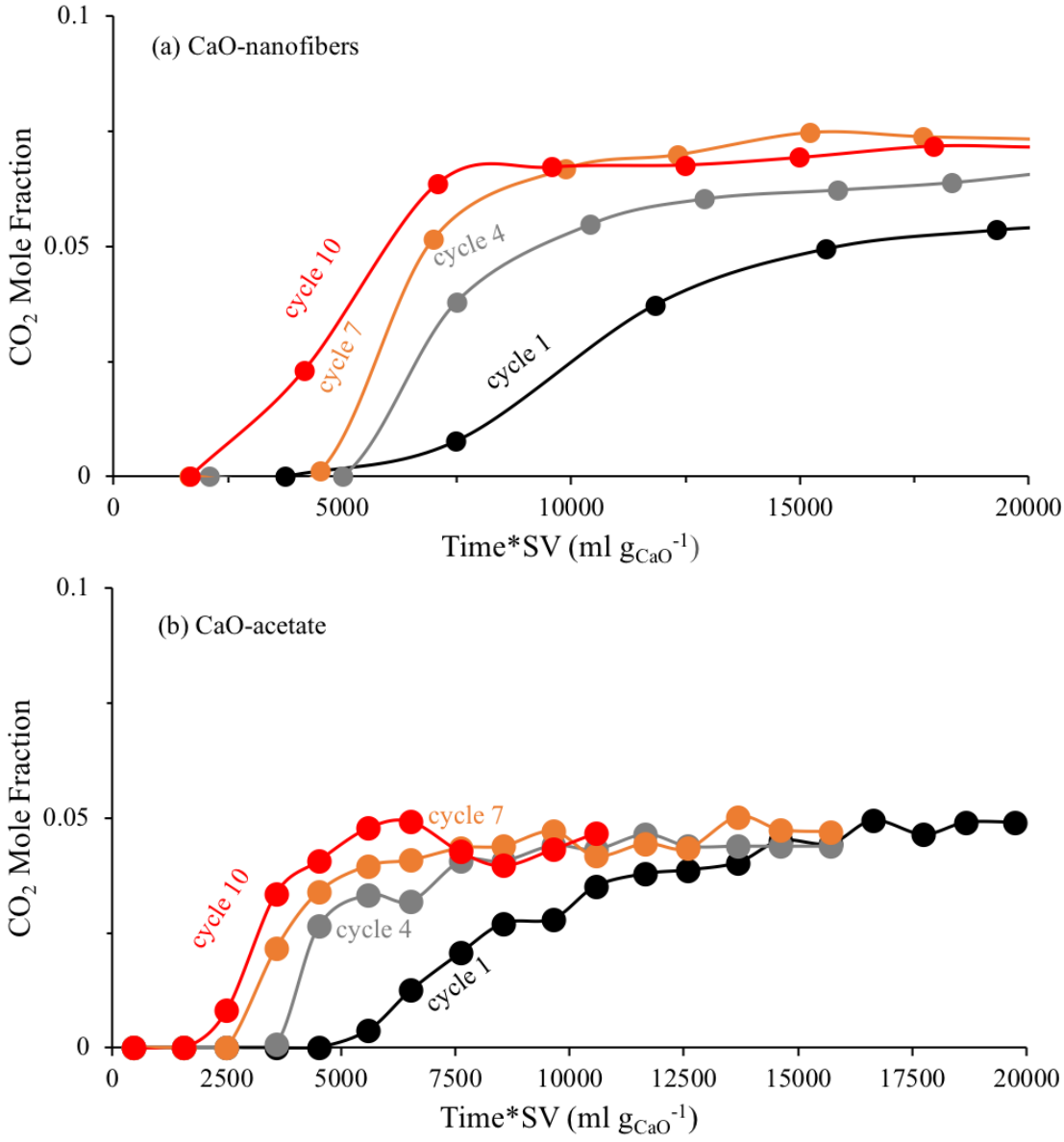
(a) CaO-nanofibers
0.1
0.05
0
CO_2 Mole Fraction
cycle 10
cycle 7
cycle 4
cycle 1
0
5000
10000
15000
20000
Time*SV (ml g_{CaO}^{-1})
(b) CaO-acetate
0.1
0.05
0
CO_2 Mole Fraction
cycle 7
cycle 10
cycle 4
cycle 1
0
2500
5000
7500
10000
12500
15000
17500
20000
Time*SV (ml g_{CaO}^{-1})

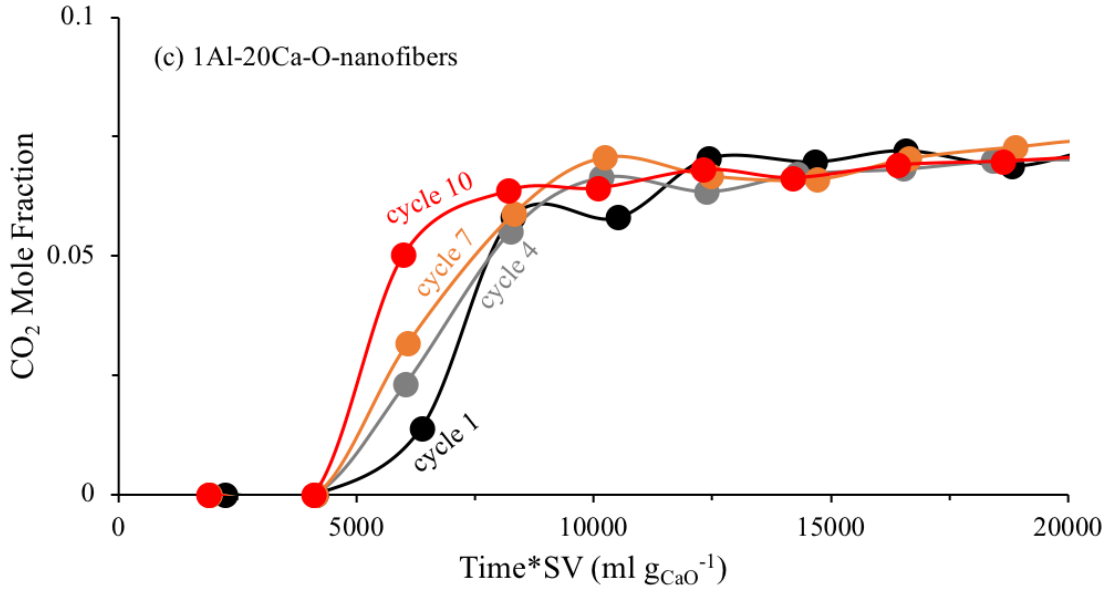

Figure 29. CO_2 mole fraction as a function of time (normalized by space velocity) over ten cycles of SE-SMR/calcination for a. CaO-nanofibers, b. CaO-D-acetate, and c. 1Al-20Ca-O. The data are simplified to show the first run (black), fourth run (gray), seventh run (orange), and tenth run (red).

Chapter 6: Summary

This work focused on (i) the effect of synthesis techniques and calcium oxide precursors on calcium oxide sorption capacity, (ii) the effect of introducing metal oxide additives to the calcium-based sorbent, and (iii) the effect of the improved sorbents on SE-SMR process performance. It was found that synthesis technique and calcium oxide precursors have a strong effect on the sorption capacity of calcium oxide in so far as it influences the sorbent material properties. The material properties that were found to have the strongest effect on sorption performance are surface area, pore volume, macroporosity, and particle size of the sorbents; in short, to maximize performance it is beneficial to minimize the size of reactive domains and maximize the porosity, surface area, and pore volume. The synthesis technique and precursor have little effect on the poor stability of pure calcium oxide sorbents upon carbonation-regeneration cycling. Metal oxide additives (Al, Co, Cr, Er, Ga, In, La, Li, Mg, Nd, Y, and Zn) were studied in depth to study their ability to mitigate the poor stability of pure calcium oxide. It was found that Tammann temperature is the dominant property determining both maximum conversion and stability of the modified-CaO sorbent. If the additive metal oxide had a low Tammann temperature, the material sintered before testing sorbent performance and thus had a low conversion, if the metal additive had a Tammann temperature above the maximum treatment temperature the conversion approached 100%. As the metal oxide Tammann temperature increased the stability of the samples were found to also increase. Other properties like additive molecular mass and formation of mixed oxides have minor effect of influencing capacity and consuming CaO, respectively. Formation of mixed oxides was found to have no impact of the stability of the sorbents. Further, the molar ratio of additive to calcium can be used to tune the stability and capacity of the sorbents. CO_2 breakthrough experiments found that CO_2 sorption

behaved as would be expected, namely higher sorption capacity under higher concentrations of CO_2 and temperatures. Calcium oxide had higher maximum sorption capacity and breakthrough times in the presence of steam in CO_2 breakthrough experiments. The performance benefits determined in the material studies were found to directly translate to improved performance in SE-SMR. Sorbents with higher capacities had longer SE-SMR breakthrough times. The stability the SE-SMR breakthrough time as a function of cycle for CaO sorbents in was similar to that determined for conversion in TGA experiments. The aluminum modified samples, 1Al-20Ca-O, only lost 5% of its breakthrough time over 10 cycles with the primary change in the breakthrough curves being that they became sharper.

Appendices

Appendix 1. Miscellaneous information

Sorbent nomenclature

Table 7. Summary of naming conventions of sorbents by precursor, synthesis technique, and chemistry.

Name	Description
CaO-marble	Commercially sources calcium oxide from marble
CaO-D-acetate	Calcium oxide from thermal decomposition of calcium acetate
CaO-D-nitrate	Calcium oxide from thermal decomposition of calcium nitrate
CaO-H-nitrate	Calcium oxide from hydrothermal synthesis using P123 and calcium nitrate
CaO-nanofibers	Unmodified calcium oxide produced via electrospinning
xM-yCa-O	Modified calcium oxide nanofibers with an additive metal to calcium molar ratio of (x:y)

Additional Equations for the Cooper Model

Equations A1-A5 is the piece-wise analytical solution to the Cooper model, where L is the length of the reactor bed:

$$\frac{C}{C_0} = 1 - \zeta e^{-\tau}, \zeta \leq 1 \tag{A4}$$

$$\frac{C}{C_0} = 1 - e^{\zeta - \tau - 1}, 1 \leq \zeta \leq 1 + \tau \tag{A5}$$

$$\frac{C}{C_0} = 0, \zeta \geq 1 + \tau \tag{A6}$$

$$\tau = k\left(t - \frac{L}{v}\right) \tag{A4}$$

$$\zeta = \left(\frac{k q_0 L}{C_0 v}\right)\left(\frac{1-\varepsilon}{\varepsilon}\right) \tag{A5}$$

Appendix 2. Pure calcium oxide sorbent supplemental figures

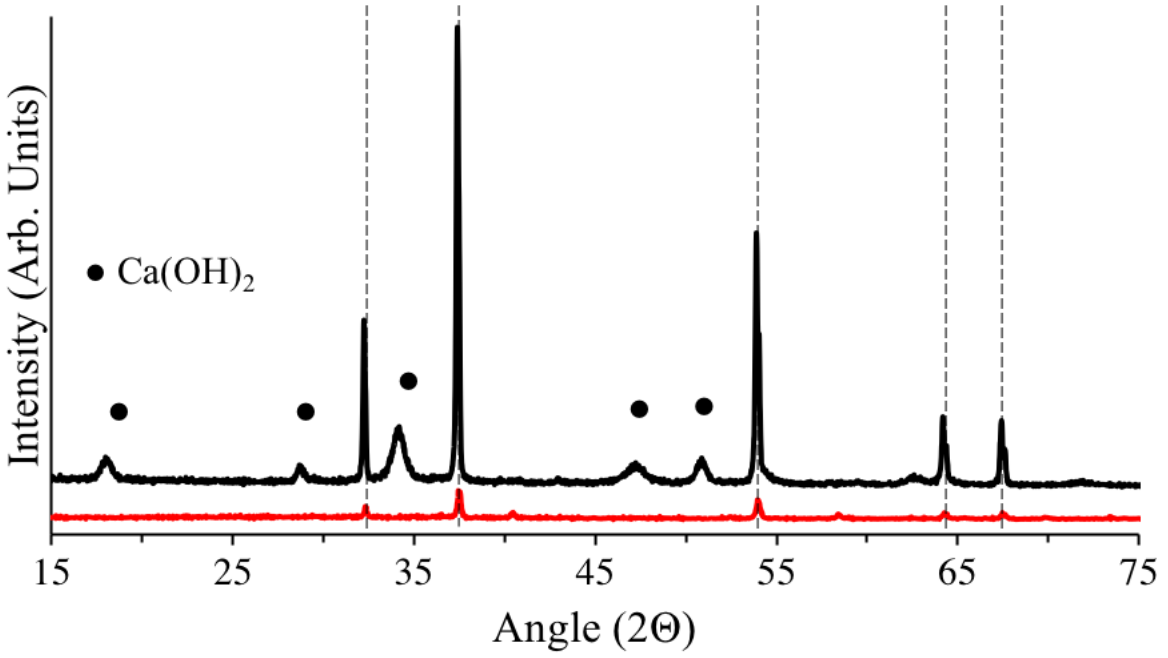

Figure 30. XRD of CaO-marble fresh (black) and post carbonation-regeneration cycling (red). Dashed vertical lines indicate CaO characteristic peaks and circles indicate $Ca(OH)_2$ characteristic peaks.

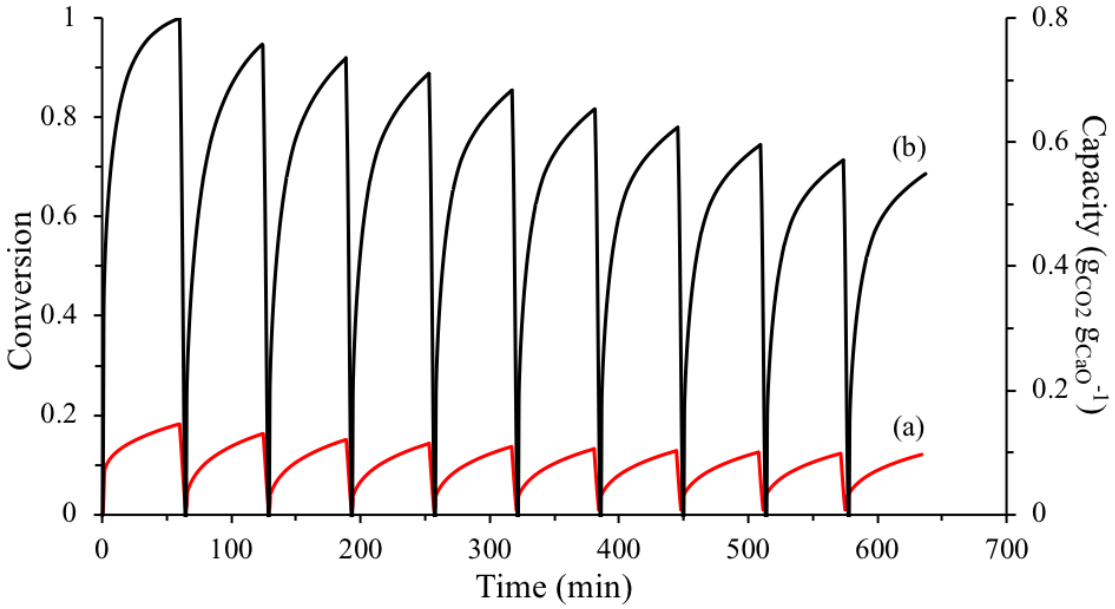

Figure 31. Conversion of (a, red) CaO-marble and (b, black) CaO-nanofibers over 10 carbonation-calcination cycles at 873 K, 1atm, and 200 sccm of CO_2.

Table 8. RPM structural parameters calculated from BET and packed bed void spacing.

Sample	S_0 (m^2 m^{-3})	L_0 (m m^{-3})	ε_0	ε_{void}
CaO-marble	2.27×10^7	5.69×10^{13}	0.1019	0.6666
CaO-D-acetate	4.13×10^7	5.69×10^{13}	0.2694	0.9101
CaO-D-nitrate	1.60×10^7	5.69×10^{13}	0.0106	0.7006
CaO-H-nitrate	3.99×10^7	5.69×10^{13}	0.2490	0.7537
CaO-nanofiber	4.08×10^7	5.69×10^{13}	0.2345	0.9715

Appendix 3. Modified calcium oxide sorbent supplemental figures

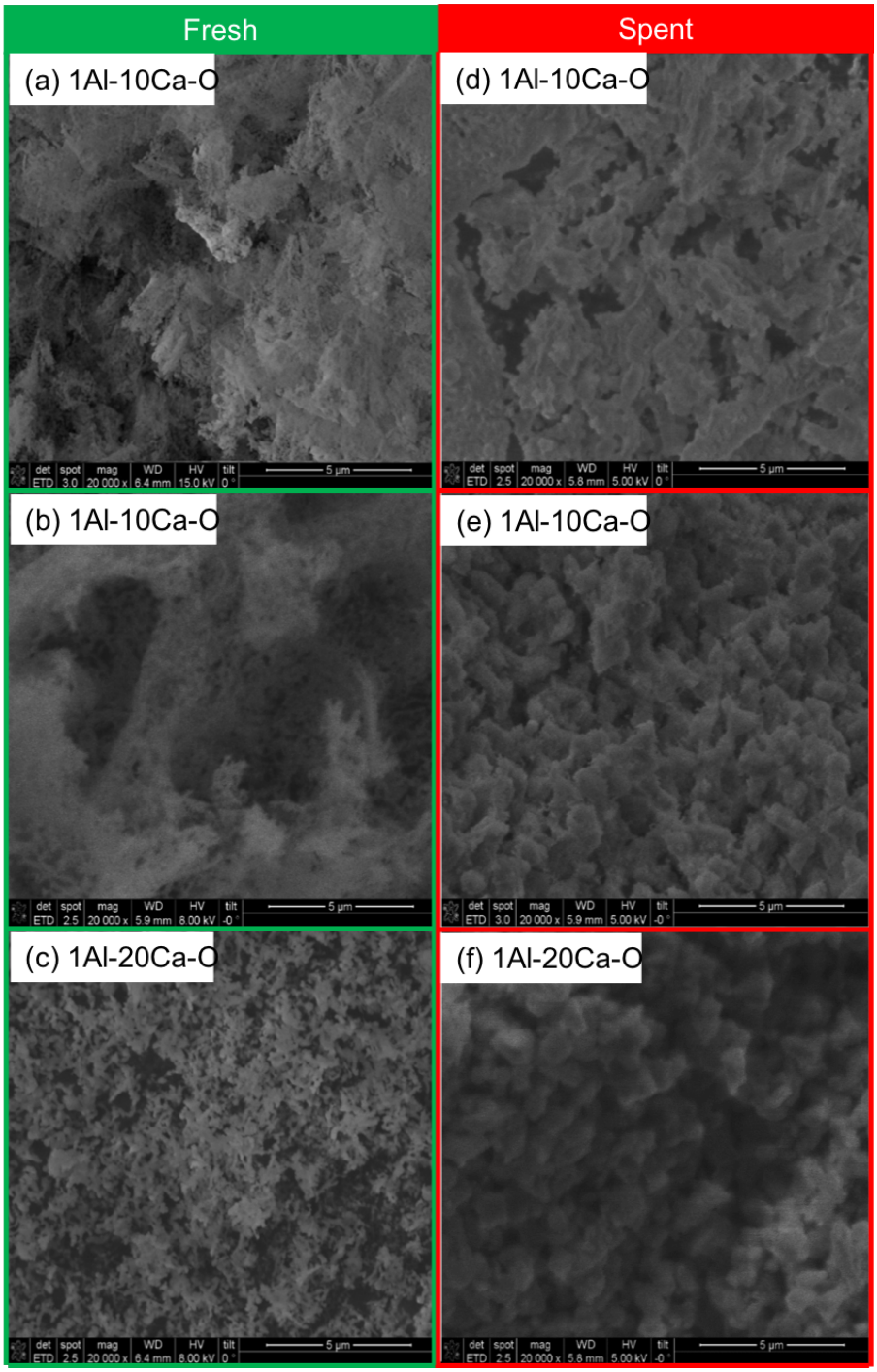

Figure 32. SEM images of a: 3Al-10Ca-O, b: 1Al-10Ca-O, c: 1Al-20Ca-O, d: 3Al-10Ca-O after 17 cycles, e: 1Al-10Ca-O after 16 cycles, and f: 1Al-20Ca-O after 16 cycles.

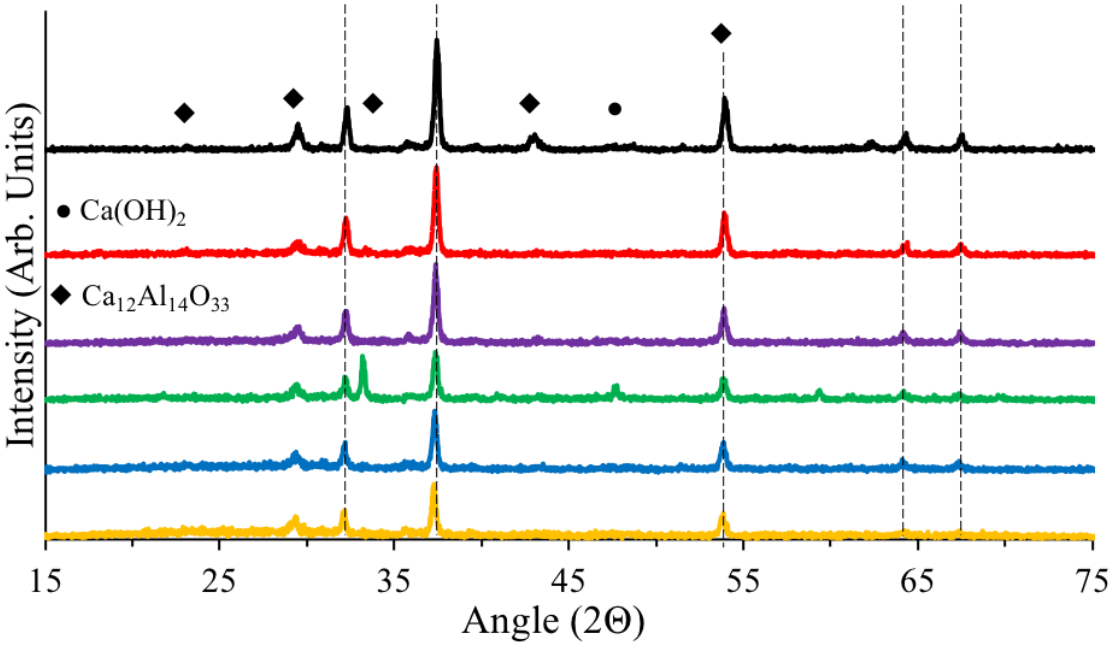

Figure 33. XRD spectrums of Al-doped CaO materials: 3Al-10Ca-O (black), 1Al-10Ca-O (red), 1Al-20Ca-O (purple), 3Al-10Ca-O after 17 cycles (green), e: 1Al-10Ca-O after 16 cycles (blue), and f: 1Al-20Ca-O after 16 cycles(yellow). Characteristic peaks for CaO, $Ca(OH)_2$, and $Ca_{12}Al_{14}O_{33}$ are indicated by vertical dashed lines, circles and diamonds.

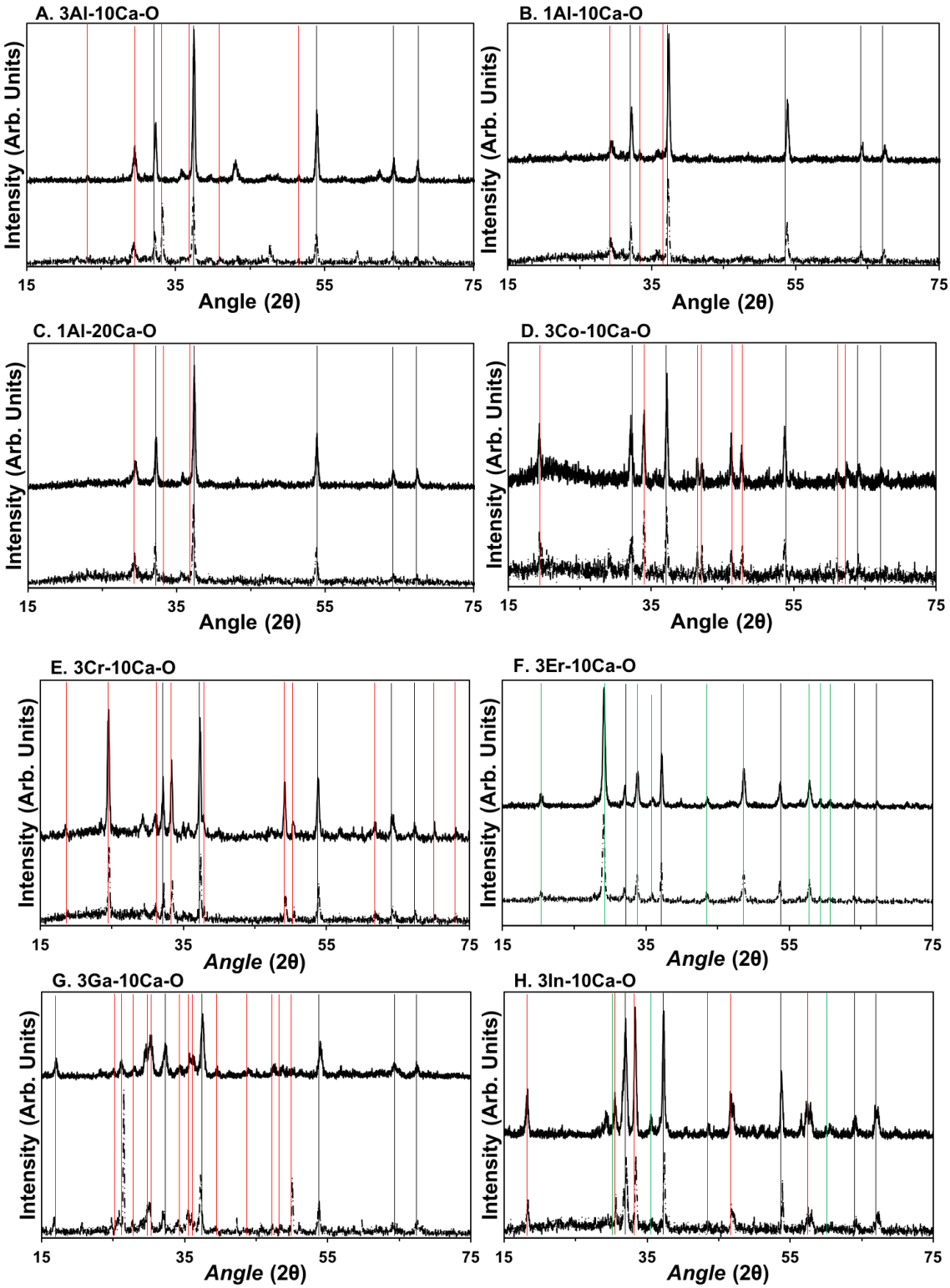
A. 3Al-10Ca-O
B. 1Al-10Ca-O
C. 1Al-20Ca-O
D. 3Co-10Ca-O
E. 3Cr-10Ca-O
F. 3Er-10Ca-O
G. 3Ga-10Ca-O
H. 3In-10Ca-O
Intensity (Arb. Units)
Angle (2θ)
15
35
55
75

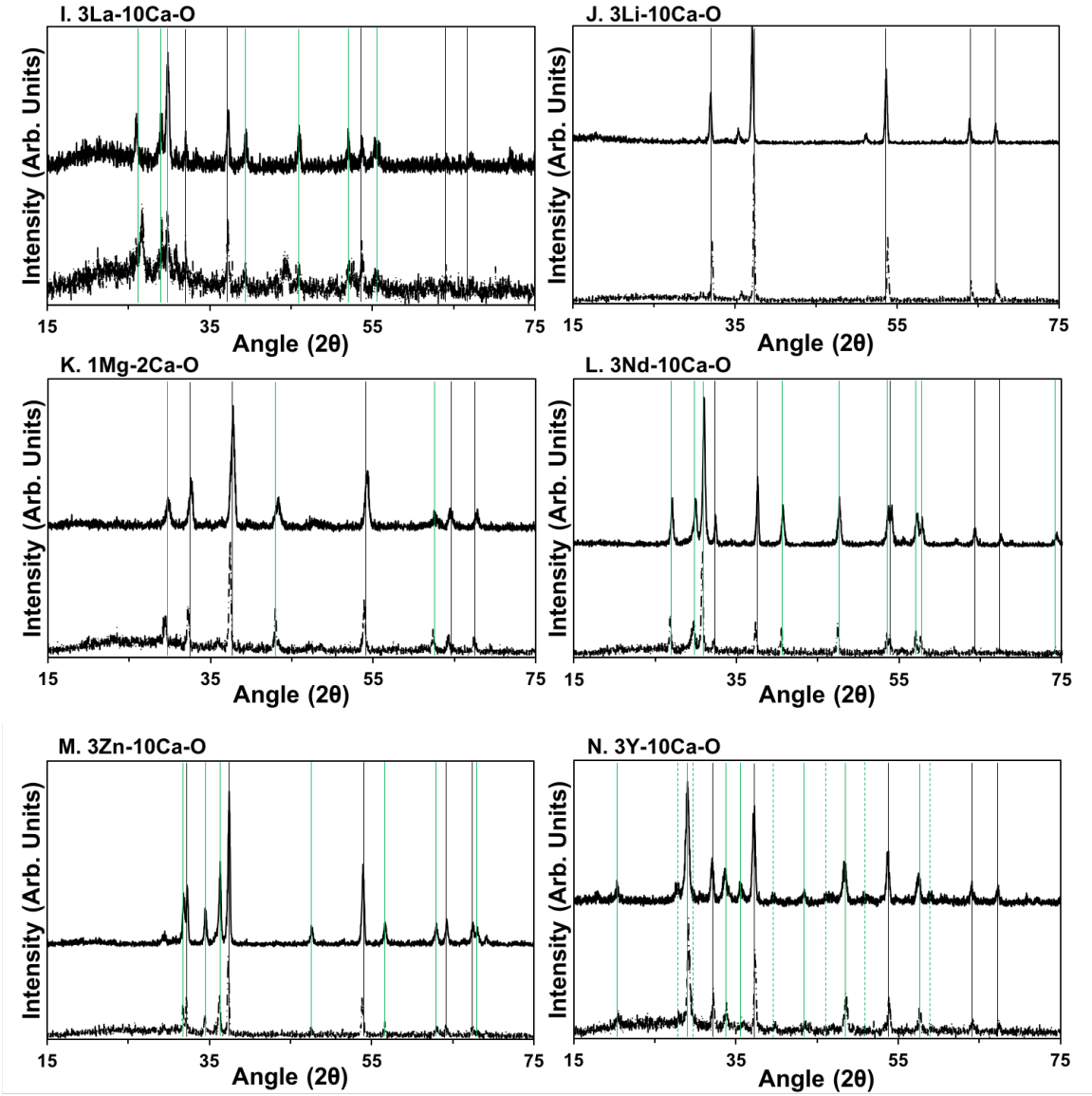

Figure 34. XRD spectra for A. 3Al-10Ca-O, B. 1Al-10Ca-O, C. 1Al-20Ca-O, D. 3Co-10Ca-O, E. 3Cr-10Ca-O, F. 3Er-10Ca-O, G. 3In-10Ca-O, H. 3Ga-10Ca-O, I. 3La-10Ca-O, J. 3Li-10Ca-O, K. 1Mg-2Ca-O, L. 3Nd-10Ca-O, M. 3Y-10Ca-O, and N. 3Zn-10Ca-O sorbents with the pre-cycle spectrum on top (solid line), and the post- cycle sample below (dashed line). Characteristic peaks for each crystal are identified using verticle lines: black lines indicate CaO (PDF#48-1467) characteristic peaks, green lines indicate the characteristic peaks for the metal oxide (M_xO_y), red lines indicate the characteristic peak for the mixed oxide ($Ca_xM_yO_z$). Yttrium hydroxide peaks were identified and labeled with green dashed lines.

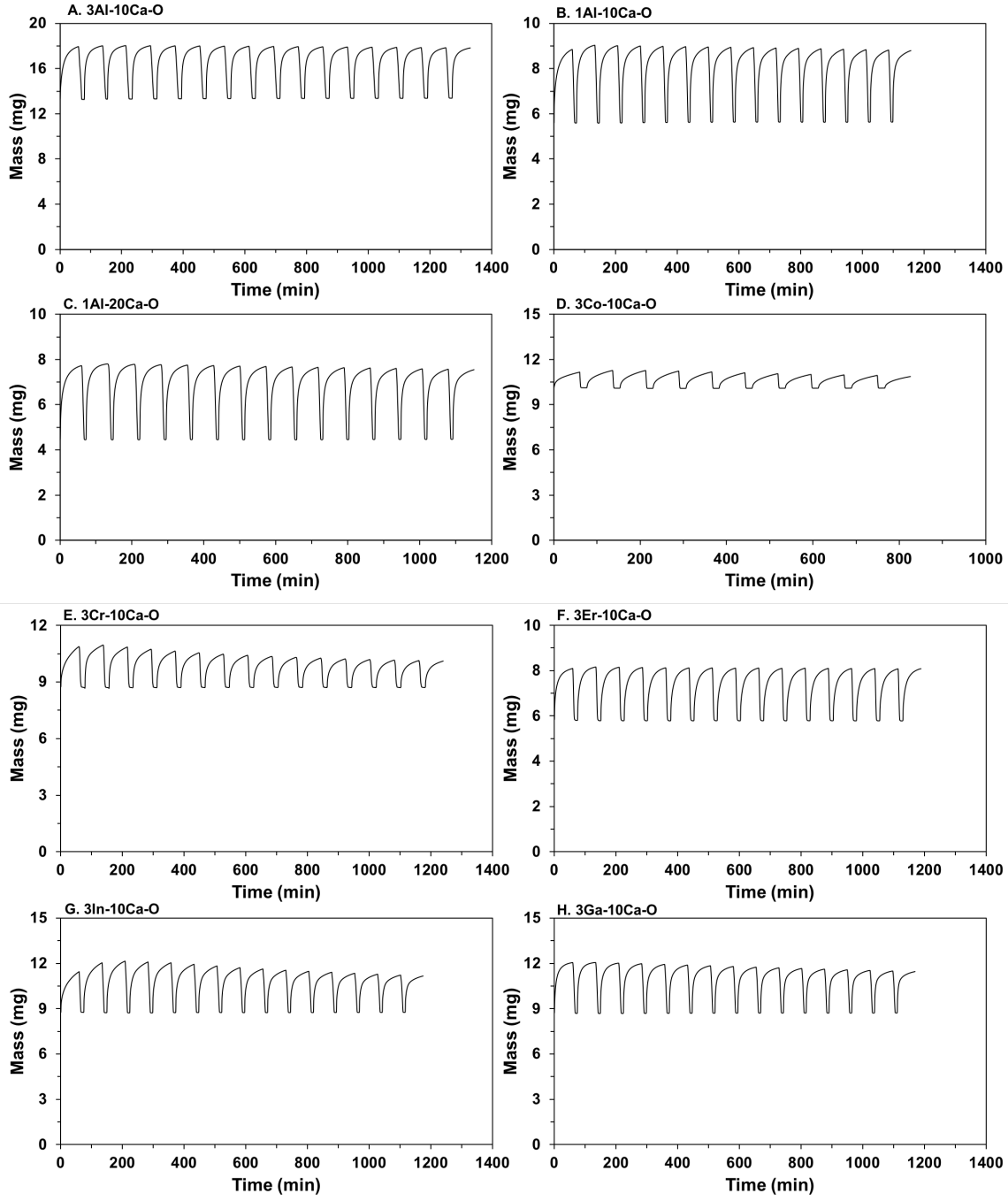
A. 3Al-10Ca-O
B. 1Al-10Ca-O
C. 1Al-20Ca-O
D. 3Co-10Ca-O
E. 3Cr-10Ca-O
F. 3Er-10Ca-O
G. 3In-10Ca-O
H. 3Ga-10Ca-O
Mass (mg)
Time (min)

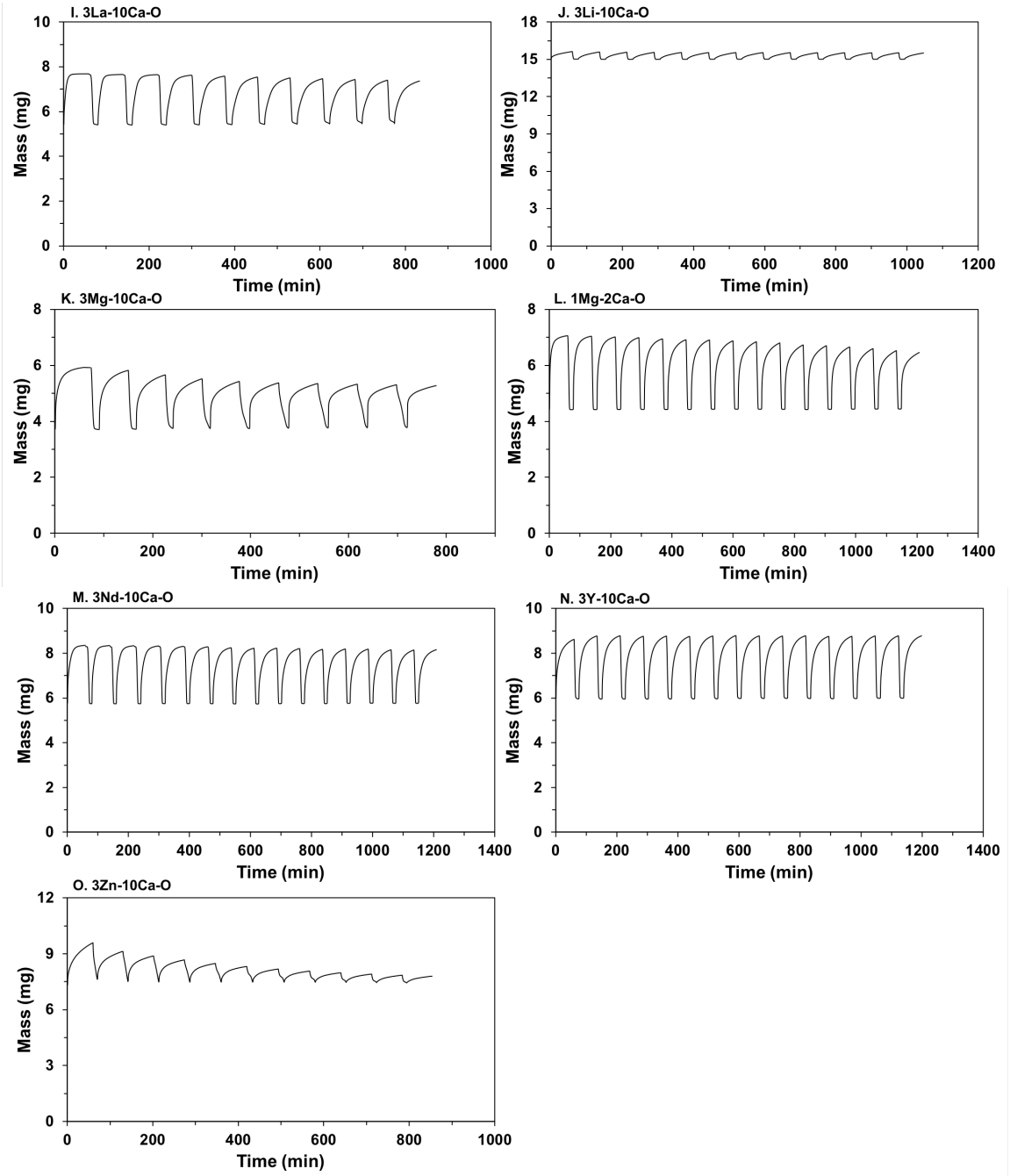

Figure 35. Raw data for TGA carbonation-regeneration cycling for A. 3Al-10Ca-O, B. 1Al-10Ca-O, C. 1Al-20Ca-O, D. 3Co-10Ca-O, E. 3Cr-10Ca-O, F. 3Er-10Ca-O, G. 3In-10Ca-O, H. 3Ga-10Ca-O, I. 3La-10Ca-O, J. 3Li-10Ca-O, K. 3Mg-10Ca-O, L. 1Mg-2Ca-O, M. 3Nd-10Ca-O, N. 3Y-10Ca-O, and O. 3Zn-10Ca-O sorbents. Each carbonation was carried out for 60 minutes in 200 sccm of 100% CO_2 at 873 K. Regeneration was carried out under 200 sccm of air at 1073 K for 10 minutes. Data is simplified by deleting data from temperature ramps and incubation periods to equilibrate sample temperature.

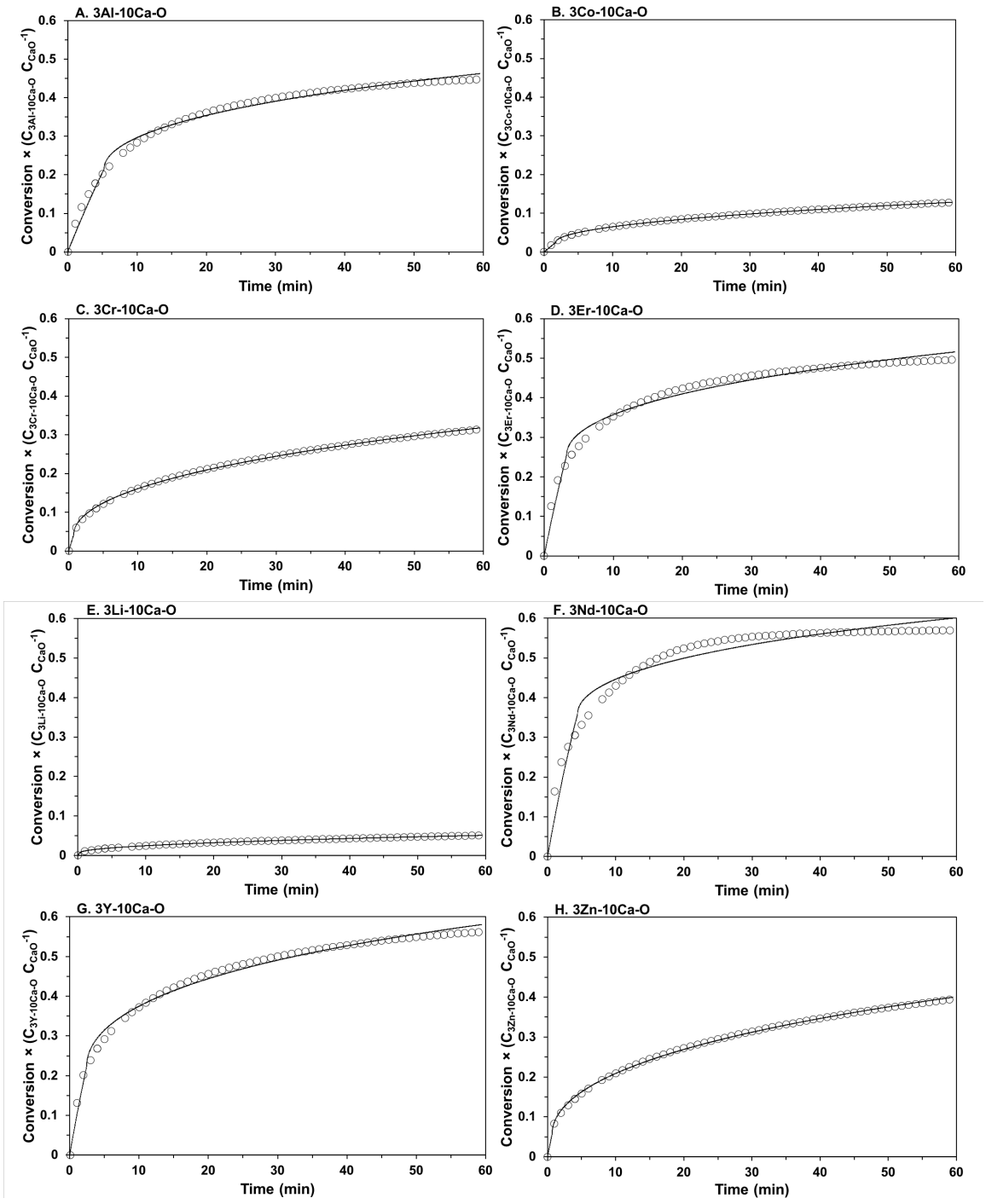

Figure 36. Raw data of the first carbonation (hollow circles) of A. 3Al-10Ca-O, B. 3Co-10Ca-O, C. 3Cr-10Ca-O, D. 3Er-10Ca-O, E. 3Li-10Ca-O, F. 3Nd-10Ca-O, G. 3Y-10Ca-O, H. 3Zn-10Ca-O sorbents with the optimized RPM fit used to determine k_{RPM} and D_{RPM} parameters. The experiment was carried out at in 200 sccm of 10% CO_2 at 873 K for 1 hr.

Table 9. Melting-point, Tammann temperature, and XRD peak location that was used in Scherrer's equation as described in the main text. Compounds that do not have a Tammann temperature in the literature are reported as 50% of the melting point.

Compound	Melting Point (K)	Tammann Temperature (K)	XRD Peak Location (°)
CaO	3171	1586 [82–84]	37
MgO	3125	1461 [82–84]	43
Y_2O_3	2683	1473 [49]	48
Er_2O_3	2617	1309	29
Nd_2O_3	2506	1253	31
La_2O_3	2490	1286 [49]	30
Al_2O_3	2273	1263 [82–84]	N/A
ZnO	2248	983 [84,85]	36
In_2O_3	2183	1092	N/A
Ga_2O_3	2173	1087	N/A
CoO	2103	1052 [83,84]	N/A
Li_2O	1711	856	N/A
Cr_2O_3	2708	1354	N/A
$Ca_{12}Al_{14}O_{33}$	1688	844[86]	30
$CaIn_2O_4$	N/A	N/A	33
$Ca_5Ga_4O_{14}$	N/A	N/A	16
$Ca_3Co_2O_6$	N/A	N/A	46
$CaCrO_4$	2980	1490	25
$CaCO_3$	1612	806 [83,84]	N/A

Appendix 4. Packed bed reactor supplemental figures

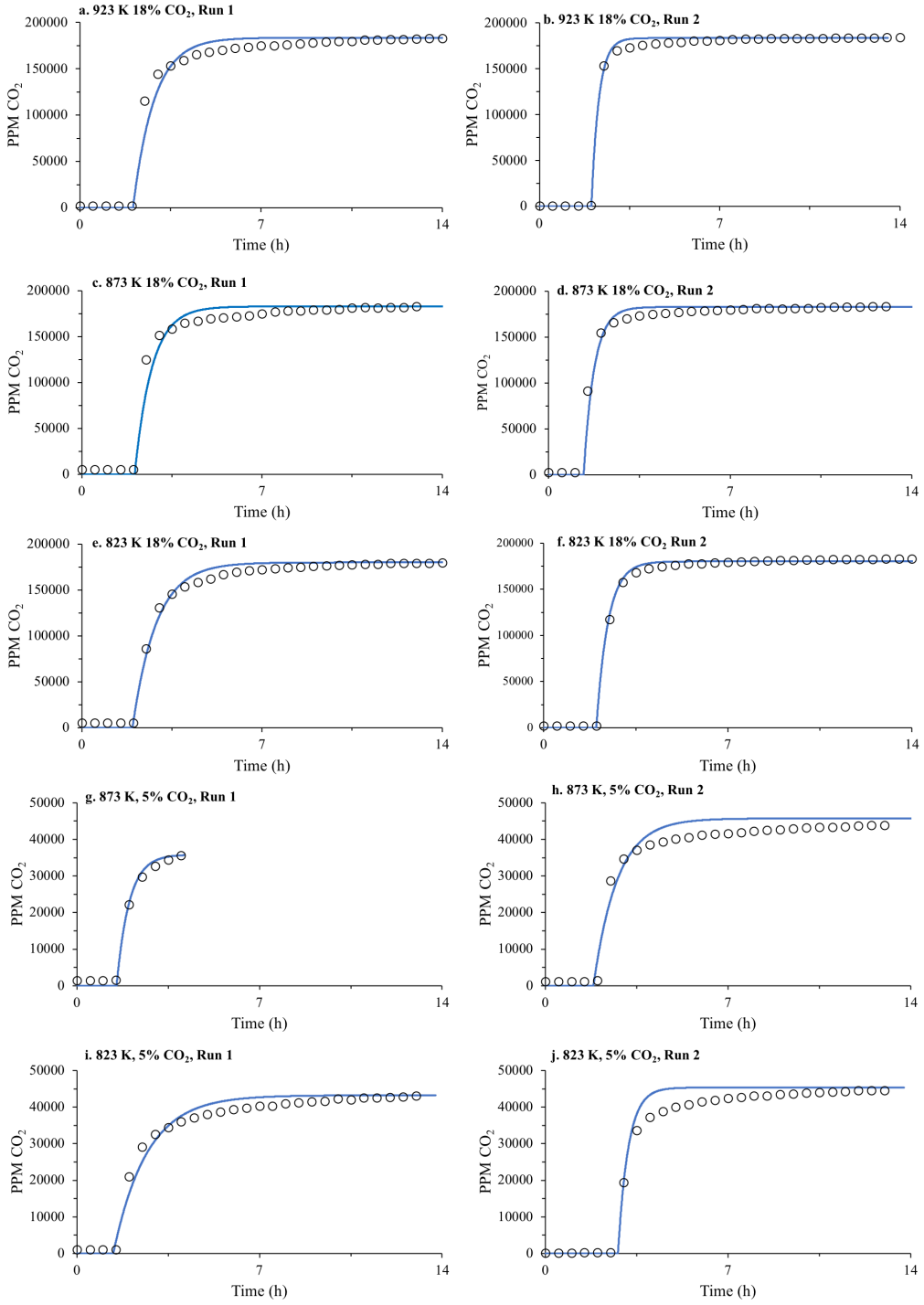

Figure 37. Cooper model fits, solid blue line, compared to the raw data for CO_2 breakthrough curves, hollow circles, in the absence of steam. a. 923 K, 18% CO_2, Run 1, b. 923 K, 18% CO_2, Run 2, c. 873 K, 18% CO_2, Run 1, d. 873 K, 18% CO_2, Run 2, e. 823

K, 18% CO_2, Run 1, f. 823 K, 18% CO_2, Run 2, g. 873 K, 5% CO_2, Run 1, h. 873 K, 5% CO_2, Run 2, i. 823 K, 5% CO_2, Run 1, i. 823 K, 5% CO_2, Run 2.

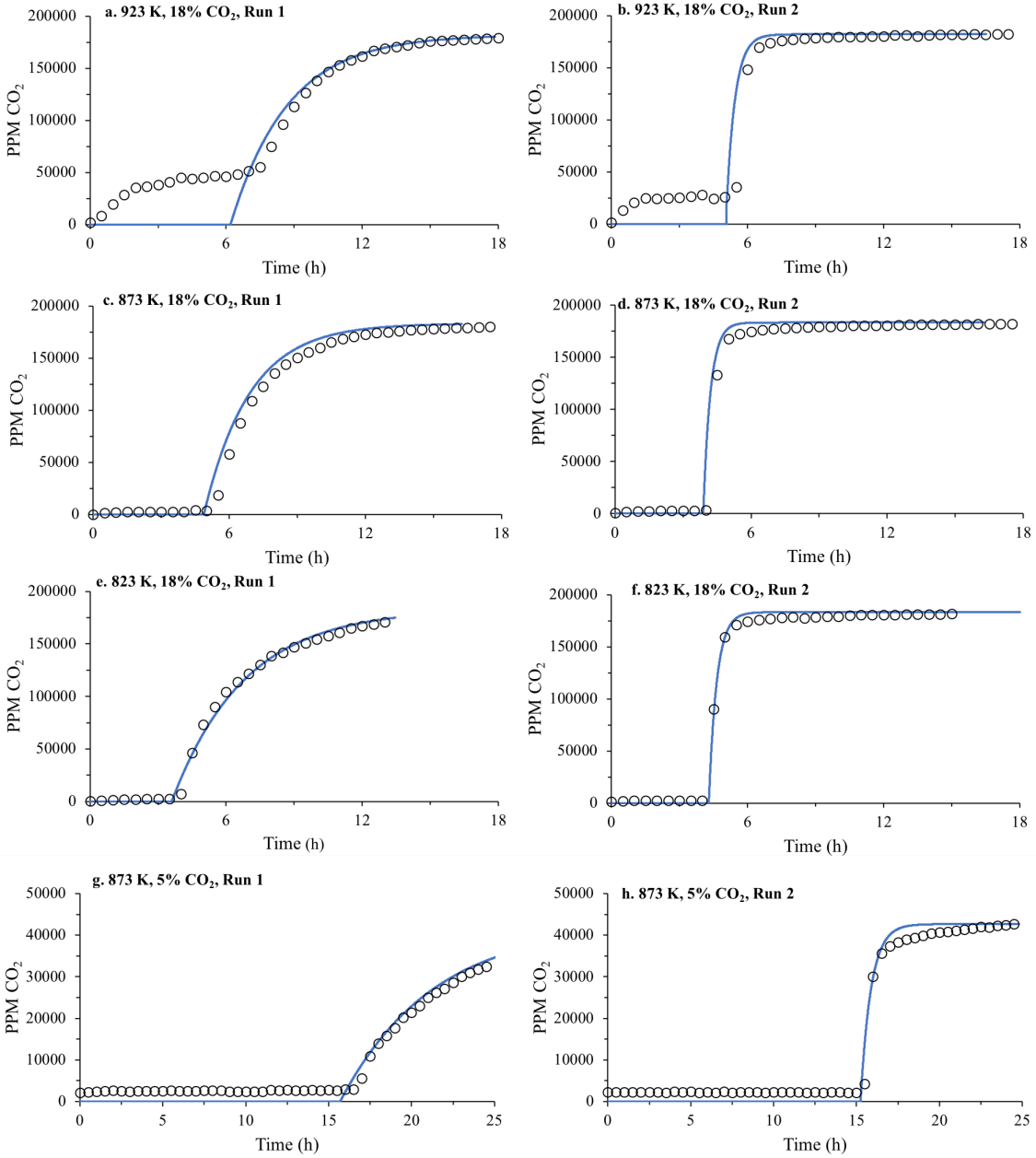

Figure 38. Cooper model fits, solid blue line, compared to the raw data for CO_2 breakthrough curves, hollow circles, in the presence of steam (~2.5:1 steam:dry gas). a. 923 K, 18% CO_2, Run 1, b. 923 K, 18% CO_2, Run 2, c. 873 K, 18% CO_2, Run 1, d. 873 K, 18% CO_2, Run 2, e. 823 K, 18% CO_2, Run 1, f. 823 K, 18% CO_2, Run 2, g. 873 K, 5% CO_2, Run 1, h. 873 K, 5% CO_2, Run 2.

Table 10. Summarized Cooper maximum capacity, q_0, and rate constant, k. Estimated by minimizing the error between the experimental data and model fit.

Presence of Steam	% CO_2	Temperature (K)	q_0 (g_{CO2} g_{CaO}^{-1})		k (s^{-1})	
			Run 1	Run 2	Run 1	Run 2
No	5	823	0.10	0.11	2.17E-04	7.06E-04
		873	0.06	0.12	5.75E-04	3.05E-04
		923				
	18	823	0.29	0.28	3.00E-04	6.24E-04
		873	0.41	0.32	4.19E-04	6.77E-04
		923	0.49	0.49	3.41E-04	9.58E-04
Yes	5	823				
		873	0.53	0.41	4.97E-05	4.18E-04
		923				
	18	823	0.73	0.50	8.69E-05	7.91E-04
		873	0.77	0.54	1.38E-04	8.72E-04
		923	0.73	0.45	1.10E-04	7.27E-04

References

1. U.S. EIA Shale Gas Data. Available at: https://www.eia.gov/dnav/ng/ng_enr_shalegas_dcu_NUS_a.htm. (Accessed: 5th May 2018)

2. Glazer, Y. R., Kjellsson, J. B., Sanders, K. T. & Webber, M. E. Potential for Using Energy from Flared Gas for On-Site Hydraulic Fracturing Wastewater Treatment in Texas. *Environ. Sci. Technol. Lett.* **1**, 300–304 (2014).

3. Balat, M. Potential importance of hydrogen as a future solution to environmental and transportation problems. *Int. J. Hydrogen Energy* **33**, 4013–4029 (2008).

4. Chaubey, R., Sahu, S., James, O. O. & Maity, S. A review on development of industrial processes and emerging techniques for production of hydrogen from renewable and sustainable sources. *Renew. Sustain. Energy Rev.* **23**, 443–462 (2013).

5. Earth System Research Laboratory. Available at: https://www.esrl.noaa.gov/gmd/ccgg/trends/global.html.

6. Gupta, H. & Fan, L.-S. Carbonation−Calcination Cycle Using High Reactivity Calcium Oxide for Carbon Dioxide Separation from Flue Gas. *Ind. Eng. Chem. Res.* **41**, 4035–4042 (2002).

7. Engineering Challenges. *National Academy of Sciences* Available at: http://engineeringchallenges.org/challenges.aspx. (Accessed: 5th May 2018)

8. Rochelle, G. T. Amine Scrubbing for CO2 Capture. *Science (80-.).* **325**, 1652–1654 (2009).

9. Barelli, L., Bidini, G., Gallorini, F. & Servili, S. Hydrogen production through sorption-enhanced steam methane reforming and membrane technology: A review. *Energy* **33**, 554–570 (2008).

10. Shah, M. M. & Drnevich, R. F. Economic Feasibility Analysis of Hydrogen Production By Integrated Ceramic Membrane System. 1–7 (2002).

11. Stein, V. E. *et al.* ION TRANSPORT MEMBRANE MODULE AND VESSEL SYSTEM. (2007).

12. Roy, S., Cox, B. G., Adris, A. M. & Pruden, B. B. Economics and simulation of fluidized bed membrane reforming. *Int. J. Hydrogen Energy* **23**, 745–752 (1998).

13. Williams, R. Hydrogen Production. (1933).

14. Mayorga, S.G.; Hufton, J.R.; Sircar, S.; Gaffney, T. R. *Sorption enhanced reaction process for production of hydrogen. Phase 1 final report*. (1997).

15. Baker, E. H. The Calcium Oxide-Carbon Dioxide System in the Pressure Range of 1-300 Atmospheres. *J. Chem. Soc.* **87**, 464–70 (1962).

16. Silaban, A., Narcida, M. & Harrison, D. P. Characteristics of the reversible reaction between CO2(g) and calcined dolomite. *Chem. Eng. Commun.* **146**, 149–162 (1996).

17. Readman, J. E. & Blom, R. The use of in situ powder X-ray diffraction in the investigation of dolomite as a potential reversible high-temperature CO2 sorbent. *Phys. Chem. Chem. Phys.* **7**, 1214–1219 (2005).

18. Ding, Y. & Alpay, E. Equilibria and kinetics of CO2 adsorption on hydrotalcite adsorbent. *Chem. Eng. Sci.* **55**, 3461–3474 (2000).

19. Ramezani, M., Tremain, P., Doroodchi, E. & Moghtaderi, B. Determination of Carbonation/Calcination Reaction Kinetics of a Limestone Sorbent in low CO2 Partial Pressures Using TGA Experiments. *Energy Procedia* **114**, 259–270 (2017).

20. Guo, H. *et al.* Incorporation of Zr into Calcium Oxide for CO2 Capture by a Simple and Facile Sol–Gel Method. *Ind. Eng. Chem. Res.* **55**, 7873–7879 (2016).

21. Luo, C., Zheng, Y., Guo, J. & Feng, B. Effect of sulfation on CO2 capture of CaO-based sorbents during calcium looping cycle. *Fuel* **127**, 124–130 (2014).

22. Blamey, J., Anthony, E. J., Wang, J. & Fennell, P. S. The calcium looping cycle for large-scale CO2 capture. *Prog. Energy Combust. Sci.* **36**, 260–279 (2010).

23. Liu, W. *et al.* Performance Enhancement of Calcium Oxide Sorbents for Cyclic CO2 Capture—A Review. *Energy & Fuels* **26**, 2751–2767 (2012).

24. Martavaltzi, C. S. & Lemonidou, A. A. Parametric study of the CaO-Ca12Al14O33 synthesis with respect to high CO2 sorption capacity and stability on multicycle operation. *Ind. Eng. Chem. Res.* **47**, 9537–9543 (2008).

25. Bo, F. & Wenqiang, L. Calcium Precursors for the Production of CaO Sorbents for Multicycle CO 2 Capture. *Environ. Sci. Technol.* **44**, 3640–3640 (2010).

26. Angeli, S. D., Martavaltzi, C. S. & Lemonidou, A. A. Development of a novel-synthesized Ca-based CO2 sorbent for multicycle operation: Parametric study of sorption. *Fuel* **127**, 62–69 (2014).

27. Koirala, R., Reddy, G. K. & Smirniotis, P. G. Single nozzle flame-made highly durable metal doped ca-based sorbents for CO2 capture at high temperature. *Energy and Fuels* **26**, 3103–3109 (2012).

28. Naeem, M. A. *et al.* Optimization of the structural characteristics of CaO and its effective stabilization yield high-capacity CO2 sorbents. *Nat. Commun.* **9**, 1–11 (2018).

29. Naeem, M. A., Armutlulu, A., Broda, M., Lebedev, D. & Müller, C. R. The development of effective CaO-based CO2 sorbents: Via a sacrificial templating technique. *Faraday Discuss.* **192**, 85–95 (2016).

30. Wang, K., Clough, P. T., Zhao, P. & Anthony, E. J. Synthesis of highly effective stabilized CaO sorbents: Via a sacrificial N-doped carbon nanosheet template. *J. Mater. Chem. A* **7**, 9173–9182 (2019).

31. Grasa, G. S. & Abanades, J. C. CO2 Capture Capacity of CaO in Long Series of Carbonation/Calcination Cycles. *Ind. Eng. Chem. Res.* **45**, 8846–8851 (2006).

32. Abanades, J. C. & Alvarez, D. Conversion limits in the reaction of CO2 with lime. *Energy and Fuels* **17**, 308–315 (2003).

33. Gommes, C. J., Blacher, S., Dunsmuir, J. H. & Tsou, A. H. Practical Methods for Measuring the Tortuosity of Porous Materials from Binary or Gray-Tone Tomographic Reconstructions. *AIChE J.* **55**, 2000–2012 (2012).

34. Valverde, J. M. & Medina, S. Crystallographic transformation of limestone during calcination under CO2. *Phys. Chem. Chem. Phys.* **17**, 21912–21926 (2015).

35. Fuertes, A. B. *et al.* Surface Area and Pore Size Changes During Sintering of Calcium Oxide Particles. *Chem. Eng. Commun.* **109**, 73–88 (1991).

36. Lu, H., Khan, A., Pratsinis, S. E. & Smirniotis, P. G. Flame-Made Durable Doped-CaO Nanosorbents for CO2 Capture. *Energy & Fuels* **23**, 1093–1100 (2009).

37. Kumar, S. & Saxena, S. K. A comparative study of CO2 sorption properties for different oxides. *Mater. Renew. Sustain. Energy* **3**, (2014).

38. Li, Z. S., Cai, N. S., Huang, Y. Y. & Han, H. J. Synthesis, experimental studies, and analysis of a new calcium-based carbon dioxide absorbent. *Energy and Fuels* **19**, 1447–1452 (2005).

39. Radfarnia, H. R. & Iliuta, M. C. Development of Zirconium-Stabilized Calcium Oxide Absorbent for Cyclic High-Temperature CO2 Capture. *Ind. Eng. Chem. Res.* **51**, 10390–10398 (2012).

40. Koirala, R., Gunugunuri, K. R., Pratsinis, S. E. & Smirniotis, P. G. Effect of zirconia doping on the structure and stability of CaO-based sorbents for CO2 capture during extended operating cycles. *J. Phys. Chem. C* **115**, 24804–24812 (2011).

41. Hu, Y. *et al.* Screening of inert solid supports for CaO-based sorbents for high temperature CO2 capture. *Fuel* **181**, 199–206 (2016).

42. López, J. M., Navarro, M. V., Murillo, R. & Grasa, G. S. Development of Synthetic Ca-based CO2 Sorbents for Sorption Enhanced Reforming Coupled to Ca/Cu Chemical Loop. *Energy Procedia* **114**, 230–241 (2017).

43. Naeem, M. A., Armutlulu, A., Kierzkowska, A. & Müller, C. R. Development of High-performance CaO-based CO2 Sorbents Stabilized with Al2O3 or MgO. *Energy Procedia* **114**, 158–166 (2017).

44. Wang, S., Fan, S., Fan, L., Zhao, Y. & Ma, X. Effect of Cerium Oxide Doping on the Performance of CaO-Based Sorbents during Calcium Looping Cycles. *Environ. Sci. Technol.* **49**, 5021–5027 (2015).

45. Yu, C. T. & Chen, W. C. Preparation, characterization of Ca/Al carbonate pellets with TiO2 binder and CO2 sorption at elevated-temperature conditions. *Powder Technol.* **239**, 492–498 (2013).

46. Wu, S. F. & Zhu, Y. Q. Behavior of CaTiO3/Nano-CaO as a CO2 reactive adsorbent. *Ind. Eng. Chem. Res.* **49**, 2701–2706 (2010).

47. Hu, Y. *et al.* Incorporation of CaO into novel Nd2O3 inert solid support for high temperature CO2 capture. *Chem. Eng. J.* **273**, 333–343 (2015).

48. Derevschikov, V. S., Lysikov, A. I. & Okunev, A. G. High Temperature CaO/Y2O3 Carbon Dioxide Absorbent with Enhanced Stability for Sorption-Enhanced Reforming Applications. *Ind. Eng. Chem. Res.* **50**, 12741–12749 (2011).

49. Xu, Y. *et al.* Characteristics and performance of CaO-based high temperature CO2 sorbents derived from a sol-gel process with different supports. *RSC Adv.* **6**, 79285–79296 (2016).

50. Zhang, X. *et al.* Investigation on a novel CaO-Y2O3 sorbent for efficient CO2 mitigation. *Chem. Eng. J.* **243**, 297–304 (2014).

51. Luo, C. *et al.* Effect of Support Material on Carbonation and Sulfation of Synthetic CaO-Based Sorbents in Calcium Looping Cycle. *Energy & Fuels* **27**, 4824–4831 (2013).

52. Luo, C., Zheng, Y., Ding, N. & Zheng, C. Enhanced cyclic stability of CO2 adsorption capacity of CaO-based sorbents using La2O3 or Ca12Al14O33 as additives. *Korean J. Chem. Eng.* **28**, 1042–1046 (2011).

53. Luo, C. *et al.* Development and Performance of CaO/La2O3 Sorbents during Calcium Looping Cycles for CO2 Capture. *Ind. Eng. Chem. Res.* **49**, 11778–11784 (2010).

54. Zhao, M., Yang, X., Church, T. L. & Harris, A. T. Novel CaO-SiO 2 sorbent and bifunctional Ni/Co-CaO/SiO 2 complex for selective H 2 synthesis from cellulose. *Environ. Sci. Technol.* **46**, 2976–2983 (2012).

55. Valverde, J. M., Perejon, A. & Perez-Maqueda, L. A. Enhancement of fast CO2capture by a nano-SiO2/CaO composite at Ca-looping conditions. *Environ. Sci. Technol.* **46**, 6401–6408 (2012).

56. Sedghkerdar, M. H., Mahinpey, N., Sun, Z. & Kaliaguine, S. Novel synthetic sol-gel CaO based pellets using porous mesostructured silica in cyclic CO2 capture process. *Fuel* **127**, 101–108 (2014).

57. Alshafei, F. H. & Simonetti, D. A. Targeted Morphology of Copper Oxide Based Electrospun Nanofibers. *Chem. Eng. Sci.* (2020). doi:10.1016/j.ces.2020.115547

58. Bhatia, S. K. & D., P. A Rondom Pore Model for Fluid-Solid Reactions: I. Isothermal , Kinetic Control. *AIChE J.* **26**, 379–386 (1980).

59. Bhatia, S. K. & Perlmutter, D. D. The effect of pore structure on fluid-solid reactions: Application to the SO2-lime reaction. *AIChE J.* **27**, 226–234 (1981).

60. Grasa, G., Murillo, R., Alonso, M. & Abanades, J. C. Application of the Random Pore Model to the Carbonation Cyclic Reaction. *AIChE J.* **55**, 1246–1255 (2009).

61. Granados, M. L. *et al.* Biodiesel from sunflower oil by using activated calcium oxide. *Appl. Catal. B Environ.* **73**, 317–326 (2007).

62. Hohman, M. M., Shin, M., Rutledge, G. & Brenner, M. P. Electrospinning and electrically forced jets. II. Applications. *Phys. Fluids* **13**, 2221–2236 (2001).

63. Shin, Y. M., Hohman, M. M., Brenner, M. P. & Rutledge, G. C. Experimental characterization of electrospinning: The electrically forced jet and instabilities. *Polymer (Guildf).* **42**, 09955–09967 (2001).

64. Piella, J. *et al.* Probing the surface reactivity of nanocrystals by the catalytic degradation of organic dyes: The effect of size, surface chemistry and

composition. *J. Mater. Chem. A* **5**, 11917–11929 (2017).

65. Liu, W. G., Low, N. W. L., Feng, B., Wang, G. & Diniz Da Costa, J. C. Calcium precursors for the production of CaO sorbents for multicycle CO2 capture. *Environ. Sci. Technol.* **44**, 841–847 (2010).

66. Nouri, S. M. M. & Ale Ebrahim, H. Effect of sorbent pore volume on the carbonation reaction of lime with CO 2. *Brazilian J. Chem. Eng.* **33**, 383–389 (2016).

67. Lu, H., Reddy, E. P. & Smirniotis, P. G. Calcium oxide based sorbents for capture of carbon dioxide at high temperatures. *Ind. Eng. Chem. Res.* **45**, 3944–3949 (2006).

68. Zhou, Z., Xu, P., Xie, M., Cheng, Z. & Yuan, W. Modeling of the carbonation kinetics of a synthetic CaO-based sorbent. *Chem. Eng. Sci.* **95**, 283–290 (2013).

69. Chen, M. & W. Goodman, D. *Structure—Activity Relationships in Supported Au Catalysts*. *Catalysis Today* **37**, (2006).

70. Bell, A. T. The Impact of Nanoscience on Heterogeneous Catalysis. *Science (80-.).* **299**, 1688–1691 (2003).

71. Somorjai, G. A. Surface Science and Catalysis. *Science (80-.).* **227**, 902–908 (1985).

72. Li, Z. & Flytzani-Stephanopoulos, M. Cu-Cr-O and Cu-Ce-O Regenerable Oxide Sorbents for Hot Gas Desulfurization. *Ind. Eng. Chem. Res.* **36**, 187–196 (1997).

73. Mess, D., Sarofim, A. F. & Longwell, J. P. Product layer diffusion during the reaction of calcium oxide with carbon dioxide. *Energy and Fuels* **13**, 999–1005 (1999).

74. Barker, R. The reactivity of calcium oxide towards carbon dioxide and its use for energy storage. *J. Appl. Chem. Biotechnol.* **24**, 221–227 (1974).

75. Ramezani, M., Tremain, P., Doroodchi, E. & Moghtaderi, B. Determination of Carbonation/Calcination Reaction Kinetics of a Limestone Sorbent in low CO2Partial Pressures Using TGA Experiments. *Energy Procedia* **114**, 259–270 (2017).

76. Iyer, M. V, Gupta, H., Sakadjian, B. B. & Fan, L.-S. Multicyclic Study on the Simultaneous Carbonation and Sulfation of High-Reactivity CaO. *Ind. Eng. Chem. Res.* **43**, 3939–3947 (2004).

77. Piella, J. *et al.* Probing the surface reactivity of nanocrystals by the catalytic degradation of organic dyes: The effect of size, surface chemistry and composition. *J. Mater. Chem. A* **5**, 11917–11929 (2017).

78. Li, Z. S., Cai, N. S. & Huang, Y. Y. Effect of preparation temperature on cyclic CO2 capture and multiple carbonation-calcination cycles for a new Ca-based CO2 sorbent. *Ind. Eng. Chem. Res.* **45**, 1911–1917 (2006).

79. Alshafei, F. H., Minardi, L. T., Rosales, D., Chen, G. & Simonetti, D. A. Improved Sorption-Enhanced Steam Methane Reforming via Calcium Oxide–Based Sorbents with Targeted Morphology. *Energy Technol.* **1800807**, 1–13 (2019).

80. Tang, Y., Elzinga, E. J., Jae Lee, Y. & Reeder, R. J. Coprecipitation of chromate with calcite: Batch experiments and X-ray absorption spectroscopy. *Geochim. Cosmochim. Acta* **71**, 1480–1493 (2007).

81. Di Giuliano, A., Gallucci, K., Giancaterino, F., Courson, C. & Foscolo, P. U. Multicycle sorption enhanced steam methane reforming with different sorbent regeneration conditions: Experimental and modelling study. *Chem. Eng. J.* **337**, 119874 (2019).

82. Tian, S., Jiang, J., Yan, F., Li, K. & Chen, X. Synthesis of Highly Efficient CaO-Based, Self-Stabilizing CO2 Sorbents via Structure-Reforming of Steel Slag. *Environ. Sci. Technol.* **49**, 7464–7472 (2015).

83. Phromprasit, J., Powell, J. & Assabumrungrat, S. Metals (Mg, Sr and Al) modified CaO based sorbent for CO2 sorption/desorption stability in fixed bed reactor for high temperature application. *Chem. Eng. J.* **284**, 1212–1223 (2016).

84. Xu, Y. *et al.* Characteristics and performance of CaO-based high temperature CO2 sorbents derived from a sol–gel process with different supports. *RSC Adv.* **6**, 79285–79296 (2016).

85. Doornkamp, C., Clement, M. & Ponec, V. The Isotopic Exchange Reaction of Oxygen on Metal Oxides. *J. Catal.* **182**, 390–399 (1999).

86. Kierzkowska, A. M., Pacciani, R. & Müller, C. R. CaO-based CO2 sorbents: From fundamentals to the development of new, highly effective materials. *ChemSusChem* **6**, 1130–1148 (2013).